

DOI 10.14750/ME.2023.011

UNIVERSITY OF MISKOLC
MIKOVINY SÁMUEL DOCTORAL SCHOOL OF EARTH SCIENCES

Head of the doctoral school:

Prof. Dr. Péter Szűcs

Professor

Propped Hydraulic Fracture Analysis

Ph.D. Thesis

Author: TAMÁS LENGYEL

MS in Petroleum Engineering

Advisor: PROF. DR. ISTVÁN LAKATOS

Professor Emeritus

Miskolc, 2022

CONTENTS

Contents.....	i
Table of Figures.....	iv
List of Tables.....	vii
Nomenclature.....	viii
Advisor’s Forward	xi
Acknowledgment	xiii
Funding	xiv
1. Introduction and topic relevance	1
1.1. Research purpose & research conducted	2
2. Hydraulic fracturing & conductivity.....	4
3. Analytical model.....	10
3.1. Proppant within fracture	13
3.2. Mono-layer pattern results.....	16
3.3. Multi-layer pattern.....	20
3.3.1. Interaction of proppants	20
3.3.2. Embedment of multi-layers.....	23
3.3.3. Multi-layer results	24
3.4. Fracture conductivity.....	25
3.4.1. Derivation.....	26
3.4.2. Analysis.....	27
3.4.2.1. <i>Proppant Size</i>	27
3.4.2.2. <i>Formation stress</i>	30
3.4.2.3. <i>Initial Fracture Aperture</i>	32
3.5. Key Factors.....	32
4. Numerical model	35
4.1. Model Physics.....	35
4.1.1. Geometry.....	35

4.1.2. Reservoir & Proppant	37
4.2. Discrete Element Model	39
4.2.1. Equations of motion	41
4.2.2. Collisions and contact model	44
4.2.3. YADE.....	45
4.2.4. Calibration Procedure.....	47
4.3. Finite Element Modeling	49
4.4. The One-Way Coupling Method	51
4.5. Numerical Fracture Model.....	52
4.6. One-way coupled model results	58
4.6.1. Proppant geometry	59
4.6.2. Proppant size, size distribution, and closure pressure	62
4.6.2.1. <i>Proppant size distribution and closure pressure</i>	64
4.6.3. Initial fracture geometry	67
4.6.4. Formation Young’s modulus and closure pressure	69
4.7. Model Validation.....	73
4.7.1. API RP 19D.....	74
4.7.1.1. <i>Test unit</i>	75
4.7.1.2. <i>Hydraulic load frame</i>	76
4.7.1.3. <i>Fluid drive system</i>	76
4.7.1.4. <i>Temperature control</i>	78
4.7.2. Laboratory experiment	80
4.7.2.1. <i>Oxygen removal</i>	81
4.7.2.2. <i>Procedure and data acquisition</i>	82
4.7.2.3. <i>Conductivity results</i>	85

4.7.3. Simulation results	89
5. Scientific Achievements	96
5.1. Thesis #1	96
5.2. Thesis #2	96
5.3. Thesis #3	96
5.4. Thesis #4	97
5.5. Thesis #5	97
5.6. Thesis #6	97
5.7. Thesis #7	98
6. Summary	99
7. Összefoglalás	100
8. Publications presented in the thesis' topic	101
8.1. Articles and proceedings	101
8.2. Conference presentations	102
9. References	104
10. Appendices	111
10.1. HiWay channel fracturing	111
10.2. Mesh independence analysis	112
10.3. Technical data sheet	113
10.4. Conductivity measurement	118
10.5. DEM source code with size distribution	120
10.6. DEM Source code for validation	130

TABLE OF FIGURES

Fig. 1	Schematic of hydraulic fracturing (Schlumberger, 2021).....	4
Fig. 2	Illustration of a propped fracture (Terracina & Harper, 2018)	5
Fig. 3	Two mutually squeezed elastic spheres (Li et al., 2015)	11
Fig. 4	Mutually squeezed plate and sphere (Li et al. 2015)	12
Fig. 5	Proppant placement between plates (Li et al., 2015)	13
Fig. 6	Stress analysis for a single proppant (Li et al., 2015)	13
Fig. 7	Partial mono-layer proppant pattern (Brannon et al., 2004)	16
Fig. 8	Relationship between proppant size and fracture aperture (edited by the Author)	17
Fig. 9	Change in fracture aperture as a function of closure pressure (edited by the Author).....	18
Fig. 10	Relationship between α , β , h and elastic modulus of proppant (edited by the Author)	19
Fig. 11	Relationship between the three variables and the elastic modulus of formation (edited by the Author) .	20
Fig. 12	Relationship between the three variables and the elastic modulus of Sphere 1 (edited by the Author)...	22
Fig. 13	Relationship between embedment and elastic modulus of Sphere 1 (edited by the Author)	22
Fig. 14	Proppant paving in multiple layers (Li et al., 2015)	23
Fig. 15	Relationship between the three variables and proppant diameter (edited by the Author)	24
Fig. 16	Relationship between the three variables and closure pressure (edited by the Author).....	25
Fig. 17	Capillary tube model (Balázs, 2013)	26
Fig. 18	Conductivity as a function of proppant diameter (edited by the Author)	28
Fig. 19	Fracture conductivity in the function of proppant diameter (edited by the Author)	29
Fig. 20	Fracture permeability in the function of proppant diameter (edited by the Author)	29
Fig. 21	Fracture conductivity in the function of closure pressure (edited by the Author)	30
Fig. 22	Fracture conductivity in the function of closure pressure and proppant size (edited by the Author)	31
Fig. 23	Fracture permeability in the function of closure pressure (edited by the Author)	31
Fig. 24	Fracture conductivity in the function of initial fracture aperture (edited by the Author)	32
Fig. 25	Elliptical bi-wind fractures in a vertical well (edited by the Author)	36
Fig. 26	Model geometry (edited by the Author)	36
Fig. 27	Flow regimes (Cinco et al., 1978)	38
Fig. 28	Simulation cycle of the Discrete Element Method (Park & Kang, 2009).....	41
Fig. 29	Force and torque indicated by the collision of two elements (Varga, 2018)	43
Fig. 30	BALL type model in YADE (Varga, 2018)	45
Fig. 31	YADE solver with Δt (edited by the Author)	46
Fig. 32	Gravitational silo discharge experiment (Oldal & Safranyik, 2015)	47
Fig. 33	Measured and calculated mass–time functions (Varga et al., 2020).....	48
Fig. 34	Process flow developed (edited by the Author).....	52
Fig. 35	Fracture filled by proppant (edited by the Author).....	53
Fig. 36	Numerical mesh of the formation (a) and proppant particles (b) (edited by the Author).....	54

Fig. 37 Surface pressure (a) and fixed support (b) (edited by the Author)	54
Fig. 38 Undeformed and deformed assembly (2x deformation) (edited by the Author)	55
Fig. 39 Residuals of CFD analysis (edited by the Author)	56
Fig. 40 Parallel monitors for numerical stability (edited by the Author)	56
Fig. 41 Flow velocity by streamlines (edited by the Author).....	57
Fig. 42 Numerical mesh of CFD analysis (edited by the Author).....	57
Fig. 43 Velocity and pressure distribution within the fracture (edited by the Author)	58
Fig. 44 Electron microscopic photos and DEM clumps (edited by the Author)	59
Fig. 45 Multi-sphere clumps (edited by the Author).....	59
Fig. 46 Sphere coordinates (edited by the Author)	60
Fig. 47 Duration of DEM runs (edited by the Author)	60
Fig. 48 Proppant roundness and sphericity (Liang et al., 2015).....	61
Fig. 49 Porosity and permeability for clumps (edited by the Author)	62
Fig. 50 Permeability and conductivity (edited by the Author).....	63
Fig. 51 Numerical and analytical conductivity (edited by the Author).....	63
Fig. 52 Detailed size distribution of 16/30 proppant (edited by the Author)	64
Fig. 53 Fracture permeability (edited by the Author)	65
Fig. 54 Fracture Conductivity (edited by the Author).....	66
Fig. 55 Fracture width (edited by the Author)	66
Fig. 56 Fracture width zoomed (edited by the Author).....	67
Fig. 57 Fracture widths (edited by the Author).....	67
Fig. 58 Porosity and permeability as the function of fracture width (edited by the Author).....	68
Fig. 59 Conductivity as the function of fracture width (edited by the Author).....	68
Fig. 60 Propped fracture in ANSYS SS with fine mesh (edited by the Author).....	69
Fig. 61 Young’s moduli impact on conductivity (edited by the Author)	69
Fig. 62 Young’s moduli impact on permeability (edited by the Author).....	70
Fig. 63 Young’s moduli impact on fracture aperture (edited by the Author).....	70
Fig. 64 An. and Num. conductivity results (edited by the Author)	71
Fig. 65 An. and Num. fracture width results (edited by the Author)	72
Fig. 66 Schematic of the model development process (Sargent, 2013)	73
Fig. 67 Exploded view of conductivity cell (DIN EN ISO 13503-5, 2008).....	76
Fig. 68 Schematic setup of API RP 19D (Pusztai & Koroncz, 2021).....	77
Fig. 69 Technical drawing of measurement cell with dimensions in [mm] (edited by the Author).....	78
Fig. 70 Water viscosity (DIN EN ISO 13503-5).....	79
Fig. 71 MaxPROP ISP G2 proppant (edited by the Author).....	81
Fig. 72 Proppant between cores from the Kővágószőlős Formation (edited by the Author)	81
Fig. 73 Standard conductivity measurement cell (edited by the Author).....	82
Fig. 74 Fracture conductivity measurement system in GEOCHEM’s laboratory (edited by the Author)	84

Fig. 75	Average Permeability (edited by the Author).....	87
Fig. 76	Average conductivity (edited by the Author)	87
Fig. 77	Average fracture width (edited by the Author).....	88
Fig. 78	Set of permeability points (edited by the Author)	88
Fig. 79	Set of conductivity points (edited by the Author).....	89
Fig. 80	Generation of proppant particles (edited by the Author)	89
Fig. 81	Unbalanced Force (edited by the Author).....	90
Fig. 82	Proppants placed and arranged (edited by the Author).....	90
Fig. 83	Filled API cell and fluid flow (edited by the Author).....	91
Fig. 84	Measured, numerical and analytical permeability (edited by the Author).....	91
Fig. 85	Measured, numerical and analytical conductivity (edited by the Author)	92
Fig. 86	Measured, numerical and analytical fracture width (edited by the Author).....	92
Fig. 87	Relative differences with API reference basis (edited by the Author).....	95

Appendix

Fig. I	Channel Fracturing (Gillard et al., 2010).....	111
Fig. II	Mesh independence study with element size (edited by the Author).....	112
Fig. III	Mesh independence study with element number (edited by the Author).....	112
Fig. IV	SinterLite Bauxit 20/40 (Schlumberger TDS).....	113
Fig. V	MaxPROP 16/30 (Schlumberger TDS)	114
Fig. VI	InterProp 16/30 (Saint-Gobain TDS).....	115
Fig. VII	Carboeconoprop 30/50 Page 1 (CARBO TDS).....	116
Fig. VIII	Carboeconoprop 30/50 Page 2 (CARBO TDS).....	117
Fig. IX	Conductivity measurement (edited by the Author).....	118
Fig. X	Temperature during conductivity measurement (edited by the Author).....	119

LIST OF TABLES

Table 1	Calibrated micromechanical parameters (Varga et al., 2020)	48
Table 2	The number of nodes and elements (edited by the Author).....	53
Table 3	Size distribution (edited by the Author)	64
Table 4	Difference between API RP 61 and 19D (edited by the Author)	75
Table 5	Proppant parameters (edited by the Author)	80
Table 6	Result summary (edited by the Author)	85
Table 7	Lab records (edited by the Author)	86
Table 8	Average Measured Data (edited by the Author).....	93
Table 9	One-way Coupling Results (edited by the Author)	93
Table 10	Absolute Difference (edited by the Author)	93
Table 11	Relative Difference (edited by the Author)	93

NOMENCLATURE

Symbol	Definition	Unit
A_s	strain tensor	[-]
A	cross-section of the porous media	[m ²]
A_i	cross-section along the fracture length	[mm ²]
A_{avg}	arithmetic mean of cross-sections in elliptical fracture	[mm ²]
$a(t)$	acceleration vector	[m/s ²]
C	constitutive matrix of elastic properties	[Pa]
C_1	reference centers of colliding elements	[-]
C_2	reference centers of colliding elements	[-]
C_E	constant	[MPa ⁻¹]
D	initial fracture aperture	[mm]
D_1	diameter of Sphere 1	[mm]
D_2	thickness of the formation	[mm]
e	internal energy	[J]
E_1	elastic modulus of Sphere 1	[MPa]
E_2	elastic modulus of Sphere 2	[MPa]
F	stress tensor	[Pa]
f	volumetric load vector	[N]
$F \cdot n / A_p$	loads on the surface A_p	[N]
f_{body}	total body force	[kg/ms]
F_{CD}	fracture conductivity	[μm·cm]
f_{surf}	total viscous force	[Pas]
h	value of embedment	[mm]
k	permeability	[μm ² =1 Darcy]
K	distance coefficient	dimensionless
K_i	stiffness of the i^{th} spring	[N/mm]
k_N	normal stiffness	[MPa·mm]
k_S	shear stiffness	[Pa]
L	length the fluid passes through	[m]
$LT-321/2$	levels indicated	[mm]
$M(t)$	inertia matrix	[kgm ²]
m_i	mass of the i -th particle	[kg]
P	external force on Spheres	[N]
p_0	overburden pressure	[MPa]
p_{abs}	absolute pressure	[psi]
P_c	closure pressure	[bar]
p_i	fluid pressure of fracturing fluid	[MPa]
P_p	pore pressure measured	[bar]
p_r	pore pressure	[MPa]

Symbol	Definition	Unit
q	vector field of heat flux	[kg s^{-3}]
Q	flowrate	[m^3/s]
\dot{Q}	rate of internal heat generation	[J/s]
r	the radius of pore throat	[μm]
R	the radius of Sphere 1 and 2	[mm]
r_0	the radius of pore throat at zero closure pressure	[μm]
$r1$	radius of Sphere 1	[mm]
$R2$	radius of Sphere 2	[mm]
S	salinity	[wt %]
T	temperature	[$^{\circ}\text{F}$]
t	time	[s]
u	displacement tensor	[m]
u	flow velocity	[m/s]
$u(t)$	displacement vector	[m]
$u _{A_u}$	displacement on the surface A_u	[m]
u_N	normal displacement	[mm]
u_S	shear displacement	[mm]
ν	poisson's ratio	[-]
$v(t)$	velocity vector	[m/s]
w	fracture aperture	[cm]
w_{f1}	fracture width from LT-321	[mm]
w_{f2}	fracture width from LT-322	[mm]
w_{favg}	average fracture width	[mm]
α	the radius of the boundary of the contact area	[mm]
α'	change in distance between the centers of Spheres	[mm]
β	proppant deformation	[mm]
β_1	deformations of Sphere 1	[mm]
β_2	deformations of Sphere 2	[mm]
γ	Biot's poroelastic constant	[-]
ΔD_2	deformation of the formation	[mm]
Δp	pressure drop indicated by the viscous forces against the motion	[Pa]
$\varepsilon(t)$	angular acceleration vector	[$1/\text{s}^2$]
μ	dynamic viscosity of the medium	[Pas]
μ_w	the viscosity of water in reservoir conditions	[cP]
μ_{w1}	the viscosity of water at a pressure of 1 bar	[cP]
ν_1	Poisson's ratio of Sphere 1	dimensionless
ν_2	Poisson's ratio of Sphere 2	dimensionless
ρ	fluid density	[kg/m^3]
σ_c	closure stress	[MPa]

Symbol	Definition	Unit
σ_v	overburden or vertical stress	[MPa]
τ	pore tortuosity	dimensionless
τ_0	pore tortuosity at zero closure pressure	dimensionless
φ	friction angle	[°]
Φ	porosity	dimensionless
Φ_0	the porosity of the proppant pack at zero closure pressure	dimensionless
$\omega(t)$	angular velocity vector	[1/s]
ω_{max}	highest eigenfrequency	[s-1]

ADVISOR’S FORWARD

The Author of the Thesis, Tamás Lengyel, was born in Miskolc in 1992. He finished his Earth Science Engineering (B.Sc.) and Petroleum Engineering (M.Sc.) studies with excellent results and honor at the University of Miskolc in 2015 and 2017. After that, the Author commenced his Ph.D. studies in the Mikoviny Sámuel Doctoral School of Earth Sciences and his research activity regarding hydraulic fracturing in the framework of the international project GINOP 2.3.2-15-2016-100010 “Development of enhanced engineering methods with the aim at utilization of subterranean energy resources” in the Research Institute of Applied Earth Sciences in 2017. Simultaneously, he also studied MBA (Master of Business Administration) and gained a degree certificate with an excellent qualification in 2019.

In addition to fulfilling the training requirements with outstanding performance; he started his research activity early, highlighting a particular chapter and merit of his habit. His research activity covering a broad range of hydraulic fracturing was presented in tremendous forums, including national and international competitions and conferences. Great honors were awarded for his performance:

- 2017, 2018, 2019 Scholarship by Hungarian National Bank (MBA)
- 2020, 2019, 2016 New National Excellence Research Scholarship (M.Sc., Ph.D.)
- 2015, 2016, 2017 MOL Academic Scholarship
- 2014, 2015 Republican Scholarship

In 2017, his scientific achievement was honored with the most significant scientific award established for students, the Pro Scientia Gold Medallion by the Hungarian Academy of Sciences. In 2018, he won the MOL FRESHHH international competition (5,000 participants), where he showed his competence in productively facing engineering, financial, and optimization challenges through the whole value chain of the petroleum industry. This achievement verified his skill of effectively combining analytical and pragmatic mindsets to solve complex issues.

In 2018, at the beginning of his Ph.D. studies, the Author decided to investigate the propped hydraulic fracture behavior further based on his previous research experience. Therefore, he marked the title of his research activity as the *Mechanical Analysis of Proppant Particles Used for Hydraulic Fracturing*. The significance of the selected topic is justified by the relevance of the national and international tight and shale reservoir production, which economic interest has been getting enormously crucial in the last decades. Furthermore, the lack of a comprehensive investigation of the proppant layers' behavior (geometrical deformation) in the international literature points out the unique nature of the topic. Considering the above, the topic is not only actual but also pioneering in both theoretical and practical aspects.

The Author of this Thesis successfully utilized his petroleum engineering and modeling knowledge to investigate the behavior of the propped hydraulic fractures. This type of interdisciplinary research is not very common in international practice, and the promising new results may affect the design of hydraulic fracturing treatment.

The Thesis is appropriately constructed and proves the candidate's skills in scientific research and publication. Several of the novel methods and numerical models developed by the Author can be considered as new scientific achievements in the discipline of hydraulic fracturing.

The candidate has fulfilled the requirements for the Ph.D. degree. He is the author or co-author of twelve conference articles (seven in the Hungarian language and five in English) in the Thesis' topic. Furthermore, he held eleven conference presentations in the topic at different conferences, among them the biggest Hungarian petroleum industry conference and more international conferences (Sofia, Singapore, Prague, Cambridge). In addition, he authored two international journal articles and one regional journal article.

Miskolc, June 15, 2022.



Prof. Dr. István Lakatos

Member of the Hungarian Academy of Sciences

ACKNOWLEDGMENT

Conducting research and accomplishing Ph.D. studies is a complex activity requiring continuous learning, improvement, patience, and persistence. In addition, the achievement is highly dependent on the Instructor's guidance, the topic relevance, the researcher's motivation, the research institute's facilities, the research tools available, and numerous other factors which would be hard to list and summarize shortly. However, the most crucial point is the Individuals who establish a network around the Author and have an impact in an interconnected way. Therefore, this brief chapter tries to highlight the indispensable Human Beings and the role of their contribution to the Author's research activity.

First of all, I want to express my gratitude to my consultant, Prof. Dr. István Lakatos, who supported me from the beginning of my Ph.D. and even earlier. He guided me in publishing articles and took a determinate part in my scientific approach. He also showed me the relevant directions during my research activity and put an enormous effort into establishing focal relations, which led to productive cooperation and scientific results.

Moreover, I would like to express my appreciation to the Research Institute of Applied Earth Sciences, especially Ph.D. Anita Jobbik and Ph.D. Krisztián Baracza, who supported my research activity from the very beginning and made several valuable resources available to me.

Furthermore, I would like to thank the support of the Petroleum Engineering Department, in particular, Ph.D. Zoltán Turzó, the Director of the Petroleum Engineering Department, who helped me personally and made the Department's resources accessible to me, and Éva Galvácsné Szarka, who provided me support and also kindness for many years.

I also would like to express my appreciation for Ph.D. Attila Varga introduced me to numerical modeling techniques and was a Co-Author of several fruitful publications of mine.

In addition, I appreciate the help of Tamás Székely-Szabó and István Huszár, excellent professionals of MOL Ltd. Upstream Division, who involved me in hydraulic fracturing treatments in 2016 and provided proppant samples for experiments.

Last but not least, I want to express my special gratitude to my Family, particularly my Wife, who showed vast patience and established calm and balanced conditions besides a lovely atmosphere for my research activity for a very long time.

FUNDING

The research was carried out in the framework of the GINOP-2.3.2-15-2016- 00010 “Development of enhanced engineering methods with the aim at utilization of subterranean energy resources” project of the Research Institute of Applied Earth Sciences of the University of Miskolc in the framework of the Széchenyi 2020 Plan, funded by the European Union, co-financed by the European Structural and Investment Funds.

1. INTRODUCTION AND TOPIC RELEVANCE

Due to the volatile macroeconomic environment, the Petroleum Industry has faced challenging periods in the last years or even decades. The oil price shock in 2014, the changing but continuously increasing demand for oil and gas, the transformation of oil refining: the shift from fuel-based products to more sophisticated petrochemicals with higher added value, and the spread of electrical vehicles (EV) are factors that mean trial for the Petroleum Industry and most of them emphasize hydrocarbon production optimization and made production intensification technologies as vital as it has never been.

Hydraulic fracturing is a well-known production intensification technique in the petroleum industry that aims to enhance the productivity of a well drilled mostly in less permeable reservoirs. To prevent the fracture from closure, highly conductive fractures are created and propped with a propping agent . The process's effectiveness depends on the achieved fracture conductivity, the product of fracture width and the permeability of the proppant pack placed within the fracture. The well productivity after hydraulic fracturing is affected by the interaction between proppants and fracture surface under closure pressures; the proppants embed into the formation and deform due to the closure stress, resulting in a significant reduction in fracture conductivity. Investigating the factors influencing the fracture conductivity is a relatively complex task because either the treatment's specifics or the reservoir's features impact the result, e.g., proppant size, Young's modulus, and Poisson's ratio of the proppant and the formation and closure pressure are factors that influence proppant embedment and fracture aperture. An embedment induced decrease in fracture aperture can reduce the fracture conductivity by 99 % (Mittal et al., 2018) with a subsequent reduction in oil or gas production.

Therefore, the Author developed a state-of-the-art method to model in-situ fracture behavior by coupling DEM-FEM-CFD numerical solutions with the consideration of fundamental factors, such as fracture geometry, proppant geometry, proppant size, uneven proppant arrangement, proppant size distribution, deformation, embedment, and fluid dynamics. The research conducted and summarized in the Thesis provides a better

understanding of propped fracture dynamics which may result in a more efficient fracturing treatment design for engineers working in the upstream division of the petroleum industry.

1.1. Research purpose & research conducted

The applied and analyzed research techniques are presented in the Thesis with the major achievements. The Author's research activity regarding hydraulic fracturing began in 2013 and focused on fracture conductivity in 2016. From the very beginning, the research path was well-defined based on the author's previous experience: investigating fracture conductivity in a microscale environment and describing the propped fracture behavior in a more sophisticated way than found in the literature.

The first period of the research activity was characterized by a comprehensive literature review, which resulted in perspicuous research perspectives and goals. The literature review summary is presented in **Chapter 2**, where research results are listed in order of their appearance. The literature review provided the author with an overall picture of experimental, analytical, semi-analytical, and numerical research regarding fracture conductivity and brought out exact research aims as listed below:

- Pointing out conductivity influencing factors by performing analytical analysis and showing parameters' relevance. **Chapter 3**
- Developing an innovative numerical method to describe propped fracture dynamics with sufficient accuracy for technical practice, i.e., the evolvement of a coupled numerical method integrating the fracture and proppant geometry, proppant size and size distribution, uneven proppant arrangement, deformation, embedment, and fluid dynamics. **Chapter 4**
- Analyzing the one-way coupled numerical model's results and comparing analytical and numerical findings with a particular focus on drawing relevant consequences. **Chapter 4.6**
- Carrying out experimental measurements using API standards and validating the model based on the results. **Chapter 4.7**

The analytical model presented in **chapter 3**, provides an understanding of the physics behind fracturing and highlights relevant factors that can determine the proppant embedment, proppant deformation, and the sum of these: the change in fracture aperture. The fracture

conductivity can also be computed by combining the Hertzian contact theory and the Kozeny-Carman capillary tube model. Using the analytical model, sensitivity tests could be accomplished to investigate the influence of factors. The results showed the crucial points where the emphasis should be put on.

Chapter 4. presents an innovative method developed by the Author's research activity that incorporates the benefit of the Discrete — and Finite Element Method to describe the in-situ behavior of hydraulic fractures with specific consideration of fracture conductivity. DEM (Discrete Element Method) provided the application of random particle generation and non-uniform proppant placement. FEM (Finite Element Method) Static Structural module was used to simulate the elastic behavior of solid materials: proppant, and formation, while CFD (Computational Fluid Dynamics) solver was applied to define fluid dynamics within the propped fracture.

The results of the numerical model were compared to API RP-19D laboratory measurements in **chapter 4.7**. The match of the outcomes verified the method and encouraged the Author to describe proppant deformation and embedment and their effect as precisely as possible. Furthermore, based on the results, sensitivity analysis was performed, which pointed out the impact of several factors affecting proppant embedment, deformation, and fracture conductivity and made one aware of a reasonable interpretation of propped hydraulic fracture operation.

The research techniques included all the conventional scientific solutions like:

- literature research to identify opportunities
- analytical model analysis to further concretize research perspectives
- numerical model development to describe the phenomenon
- laboratory experiments for model validation

The scientific achievements have been continuously published, and they are listed at the end of the Thesis in **chapter 8**. The author does hope that the developed coupled numerical model will be utilized in fracturing treatment design by practicing engineers, and the presented theory, methods, analysis, validation, and scientific results will be accepted to fulfill the requirements of the Ph.D. program.

2. HYDRAULIC FRACTURING & CONDUCTIVITY

Hydraulic fracturing is one of the most common improved oil recovery (IOR) methods used in the Upstream Division of the Petroleum Industry to enhance well productivity in tight gas/oil or shale gas/oil reservoirs (Denney, 2010). The purpose of fracturing is production intensification by creating highly conductive, propped fractures that provide a larger inflow surface than the cylindrical area of an ordinary well (Economides & Nolte, 2000). The fracturing procedure is controlled on the surface and executed by high-power hydraulic pumps boosting the hydraulic fluid to exceed the formation breakdown pressure at the bottom hole (**Fig. 1** represents the schematic illustration of hydraulic fracturing). The fracking fluid contains ~ 99 % water and ~ 1 % additives to increase the dynamic viscosity, thus preventing fluid leak-off and enabling pressure build-up at the bottom hole. This hydraulic fluid pressure initiates the formation to break. Meanwhile, the fracture starts to propagate according to the petrophysical properties of the given formation. Proppant is a granular media with high porosity mixed with the fracturing fluid to prop the fracture and prevent formation closure that would result in an ineffective stimulation (Barree & Conway, 1995).



Fig. 1 Schematic of hydraulic fracturing (Schlumberger, 2021)

The phenomenon investigated in the Thesis occurs after fractures are created and hydraulic pumps are stopped entailing the hydraulic fluid pressure to drop below the formation closure pressure. At this point, there is no more extra pressure energy to hold the fractures open, which leads to a closing action of the formation mitigated by proppant particles that carry the stresses of formation closure (Liang et al., 2015). **Fig. 2** demonstrates the propped fracture. The primary indicator, which characterizes the fracturing treatment, is the fracture conductivity calculated as the product of fracture width and proppant pack permeability. Since the above-described situation affects fracture conductivity significantly, it is crucial to model the problem comprehensively.



Fig. 2 Illustration of a propped fracture (Terracina & Harper, 2018)

Several earlier studies deal with proppant embedment; Huitt and McGlothlin (1958) derived an equation based on the knowledge of proppant concentration and overburden load to compute proppant embedment. It is a semi-empirical model containing two characteristic constants, which could be determined by fitting the results with experimental data. They performed relevant experiments to prove the capability of this equation, and they found that proppant embedment is a more relevant phenomenon than proppant crush under formation pressure. The factors affecting proppant embedment were determined by the formation's competency, the proppant's size, the concentration of the proppant, and the overburden pressure. They concluded that a stiffer, tougher material would be a better propping agent than sand because sand would crush rather than embed under the overburden pressure.

Volk et al. (1981) derived empirical equations based on experimental data to determine the parameters influencing proppant embedment, such as proppant concentration, size, distribution, rock type, etc.

Lacy et al. (1997) carried out experimental research on proppant embedment in non-tight reservoir cores; therefore, the results can be interpreted as limited ones. Nevertheless, the results showed that the most critical factors that have a relevant impact on proppant embedment were closure pressure, proppant size, and fluid properties. Therefore, Lacy et al. (1998) also developed a computer-controlled measurement that determined propped-fracture width and proppant embedment as a function of closure pressure, concentration of proppant paving, proppant size, core mechanical characteristics, etc.

Guo and Liu (2012) investigated the proppant embedment in core samples experimentally. They also found that the fracture width could be remarkably reduced because of the proppant embedment, especially in soft formations. They examined the experimental data of proppant embedment at different conditions, and they published empirical equations that can determine the proppant embedment as a function of formation pressure, the elastic modulus of the core, and proppant concentration.

Further experimental studies of proppant embedment and fracture conductivity were published by many researchers (Lehman et al., 1999, Fredd et al., 2000, Barree et al., 2003, Weaver et al., 2008, McDaniel et al., 2010). However, these empirical or semi-empirical solutions could provide interpretations in limited conditions. Others (Cooke, 1973, Roodhart et al., 1988, Peard et al., 1991, Milton-Tayler et al., 1992) also conducted experimental research about fracture conductivity. However, the exactness of these developed models considering the prediction of in situ fracture behavior may not be satisfactory due to the artificial conditions from which they have been derived.

The lack of a comprehensive analytical model was fulfilled by Li et al. (2015), who developed an analytical approach based on the Hertzian Contact Theory to investigate the effect of proppant deformation and embedment on fracture conductivity. Their research was derived from two mutually squeezed spheres and considered only mathematical and physical principles; therefore, it was found to be a valuable method to gain information about conductivity influencing factors. Their approach provides insights for proppant embedment, change in fracture aperture, deformation, permeability, and conductivity for single- and multi-layer

patterns. Furthermore, their equations are completely analytical, resulting in an elegant solution for fracture behavior modeling. However, it also has limitations because some random factors, like non-regular proppant shape, uneven proppant placement, uneven stress distribution, and complicated fracture geometry, cannot be described analytically.

After all, it can be stated that the detailed description of a propped fracture behavior requires a numerical solution due to the random characteristic of the phenomenon. Therefore, a few numerical approaches have already been developed. For example, Sun et al. (2014) investigated the impact of high-quality proppant on fracture conductivity and long-term production. They created a numerical model based on field case studies, and the result showed that upgrading the completion design with a high resistant proppant enhanced the production enormously.

Fan et al. (2017) investigated hydraulic fracture conductivity by creating a coupled numerical model using Particle Flow Code (PFC), which is a three-dimensional discontinuum mechanics simulator, and the lattice Boltzmann (LB) method to solve the Navier–Stokes equations. In addition, the effect of proppant concentration in the fracture and effective stress was investigated, and they found the partial mono-layer pattern with large-diameter proppants as an alternative to improve fracture conductivity.

Zhang et al. (2017) developed a DEM–CFD numerical modeling process to examine proppant embedment and fracture conductivity after hydraulic fracturing in shale formations. They concluded that shale hydration is the main reason for proppant embedment. They also found that conductivity increases with proppant concentration and size and decreases with closure pressure.

Zhu et al. (2018) examined a reasonably new fracturing technique called channel fracturing, presented in **Appendix 10.1**, in **Fig. I**. The essence of channel fracturing is promoting the hydrocarbon-bearing rock stable voids by intermittent proppant pumping and mixing fibers to the fracking fluid to prevent the dispersion of the proppant pulses. These voids serve as high conductive areas within the proppant pack to improve the oil transport into the well. The method is considered to be more effective than conventional fracturing. Finally, Zhu et al. (2018) developed a method based on DEM to optimize channel fracturing in the field.

Zhang and Dontsov (2018) dealt with hydraulic fracturing in a two-layer formation characterized by different pressures. Their research aimed to define the size of the proppant

particle, which eases the pinching effect observed at the interface of the layers. As a result, they developed a numerical method (Distinct Element Method) to estimate the pinching aperture and select the ideal size proppant for the case.

Fan et al. (2019) also conducted experimental and numerical research on fracture conductivity in narrow fractures. They used laboratory experiments and a numerical modeling approach that combines continuum mechanics, the discrete element method, and the lattice Boltzmann (LB) method. Their results showed a strong correlation between proppant embedment and mechanical rock properties. However, the results are related to narrow fractures only, characterized mainly by mono-layer proppant pattern.

In conclusion, one can ascertain that fracture conductivity is one of the most important indexes that can evaluate the impact of fracturing on production intensification, and it is affected by many factors, such as closure pressure, proppant size, the elastic modulus of proppant, and the formation, etc. Unfortunately, one can obtain that even if some articles were published on fracturing in Hungary (Nádor et al., 2016, Kiss, 2015), there is no Hungarian publication focusing on propped fracture analysis or in-situ fracture behavior.

The studies and articles listed and presented briefly above summarize the results achieved in hydraulic-fracture-behavior-related research. In the first period, mainly experimental examinations were conducted to simulate fracture conductivity. As the technology evolved and hydraulic fracturing was spread to enhance unconventional hydrocarbon production, the need for more sophisticated solutions arose. An analytical approach was developed to determine and investigate conductivity influencing parameters, and numerical models were introduced to precisely examine the problem. Proppant embedment or even proppant crush is integrated into these numerical models; nevertheless, they consider proppant particles as rigid spheres ignoring the effect of proppant deformation that may exceed the impact of embedment into the formation and particle fragmentation on fracture conductivity.

Therefore, the Finite Element Method (FEM) was integrated into my coupled numerical model not only to describe fluid dynamics in the porous media represented by the propped fracture but also to include the effect of proppant deformation. The pursuit was to develop a coupled numerical model to describe the hydraulic fracture behavior under the in-situ condition as precisely as possible. Finally, a complex workflow was invented that simulates random and uneven proppant placement, the closing action of the formation considering the rock and

proppant as elastic bodies, and involves fluid dynamics at typical fractured well flow rates. After all, the coupled numerical model results were matched with API RP19D lab data, and the method was validated. The findings of underground achievable fracture conductivity – differing from analytical model outcomes – showed the potential of DEM–FEM–CFD coupling for modeling multidisciplinary processes regarding hydraulic fracturing.

3. ANALYTICAL MODEL¹

At the beginning of the Author's scientific research activities regarding propped hydraulic fracture behavior, an analytical method developed by Li et al. (2015) based on the Hertzian Contact Theory was selected and used to point out propped hydraulic fracture specifics and highlight factors that influence fracture conductivity after all. Not only factors but also their impact could be revealed that served as a practical method that determined the scientific path and indicated the involvement of numerical methods to model in-situ fracture behavior. This chapter introduces the analytical model and the theory behind it to show the theoretical background and basics of fracture aperture closure, nevertheless highlights the significant sensitivity test results, shows the complexity of the phenomenon, and anticipates the research path forward.

In the following, one can obtain the theoretical background of the analytical model being the derivation process described below. As this mathematical approach was derived as the extension of the Hertzian Contact Theory, which assumes completely flexible spheres, the model has some limitations considering proppant and fracture behavior. During the stress/strain analysis, it was assumed that the proppant would rather deform and embed into the formation under closure stress than break, entailing no proppant crush incident. Assuming linear elastic behavior, the equations below can be used and considered valuable tools to define the trend of a propped fracture's mechanical behavior below the stress range that would cause a proppant crush.

¹ The chapter is based on the research conducted for the "National Scientific Students' Association Conference 2017"

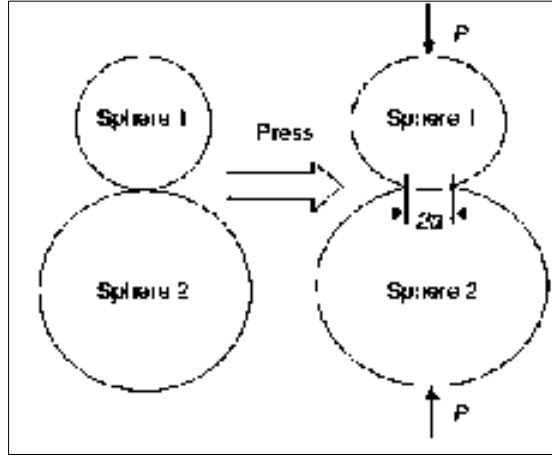


Fig. 3 Two mutually squeezed elastic spheres (Li et al., 2015)

The derivation begins with a stress-strain formula of two mutually squeezing elastic spheres, shown by Wu et al. (2001) and illustrated in **Fig. 3**, where Sphere 1 and 2 deform under balanced load. The boundary of the contact area of the Spheres is a circle, and its radius (α) can be expressed as follows:

$$\alpha = \left(\frac{3}{4} P C_E \frac{R_1 R_2}{R_1 + R_2} \right)^{\frac{1}{3}}, \quad (1)$$

where α is the radius of the boundary of the contact area, in [mm]; P is the external force on Spheres 1 and 2, in [N]; R_1 is the radius of Sphere 1, in [mm]; and R_2 is the radius of Sphere 2, in [mm]. C_E is a constant associated with the elastic moduli and Poisson's ratios of Spheres 1 and 2 in [MPa⁻¹] and it can be defined as:

$$C_E = \frac{1-\nu_1^2}{E_1} + \frac{1-\nu_2^2}{E_2}, \quad (2)$$

where ν_1 is the Poisson's ratio of Sphere 1, dimensionless; ν_2 is the Poisson's ratio of Sphere 2, dimensionless; E_1 is the elastic modulus of Sphere 1, in [MPa]; E_2 is the elastic modulus of Sphere 2, in [MPa].

Wu et al. (2001) proved that the following relationship could describe the change in distance between the centers of Spheres 1 and 2:

$$\alpha' = \frac{\frac{3}{4} P C_E}{\left(\frac{3}{4} P C_E \frac{R_1 R_2}{R_1 + R_2} \right)^{\frac{1}{3}}}, \quad (3)$$

where α' is the change in distance between the centers of Spheres in [mm].

When $R_2 \rightarrow \infty$, the surface of Sphere 2 tends to be a plane, and the two objects become mutually squeezed sphere and plane. **Fig. 4** demonstrates the interaction between the sphere and the plane. One can observe that α' is affected by two factors: change in radius of Sphere 1 (called deformation) and embedment.

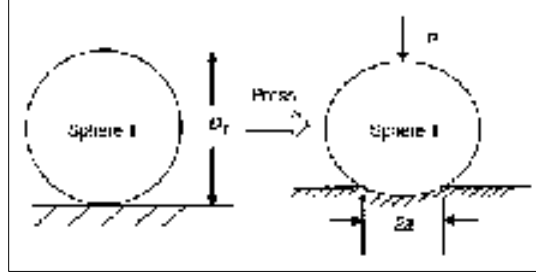


Fig. 4 Mutually squeezed plate and sphere (Li et al. 2015)

For the situation in Fig. 4, a modified formula can be derived on the basis of Eq. 3:

$$\alpha' = \frac{2(\frac{3}{8}PC_E D_1)^{\frac{2}{3}}}{D_1}, \quad (4)$$

where D_1 is the diameter of Sphere 1, in [mm].

At this step, **Eq. 4** contains two factors; these are the change in radius of Sphere 1 (deformation) and the embedment. To derive the deformation of Sphere 1 (β) from **Eq. 4**, the other influencing factor - which is the embedment - must be separated. Therefore, assume that the elastic modulus of the plate (E_2) is infinite, so Sphere 1 does not embed into the plate. In this case, α' is affected only by deformation. Thus, the formula of deformation of Sphere 1 (β) can be expressed as the following relationship:

$$\beta = \frac{2(\frac{3}{8}PD_1 \frac{1-\nu_1^2}{E_1})^{\frac{2}{3}}}{D_1}. \quad (5)$$

From **Eq. 5**, it can be stated that deformation is influenced only by the values of external force, the diameter, elastic modulus, and Poisson's ratio of Sphere 1 but is not affected by any plate parameters.

Since α' was interpreted as the sum of the embedment and the deformation, subtracting **Eq. 5** from **Eq. 4**, the formula of the embedment of Sphere 1 can be expressed as:

$$h = \alpha' - \beta = \frac{2(\frac{3}{8}PD_1)^{\frac{2}{3}}}{D_1} \left[\left(\frac{1-\nu_1^2}{E_1} + \frac{1-\nu_2^2}{E_2} \right)^{\frac{2}{3}} - \left(\frac{1-\nu_1^2}{E_1} \right)^{\frac{2}{3}} \right], \quad (6)$$

where h is the value of embedment, in [mm].

3.1. Proppant within fracture

To approximate the actual condition of the fracture, the situation of spheres being squeezed by two horizontal plates must be described. The analytical model (Li et al., 2015) assumes that the weight of spheres can be ignored, and the stress on spheres and contact areas of the upper and lower plate is the same, meaning a perfectly even stress distribution on the bodies. To create the model more realistic, Sphere 1 is considered to be equivalent to the proppant and Sphere 2 to the formation, i.e., the upper and lower plates. The proppants are also assumed to be evenly distributed on the formation (mono-layer pattern). Li et al. (2015) introduced a so-called distance coefficient K which helps to represent the distance between the centers of two adjacent proppants as KD_1 . K is equal to unity when proppants are touched by each other and greater than unity if not. **Fig. 5** represents the placement of proppants (single layer) in the fracture.

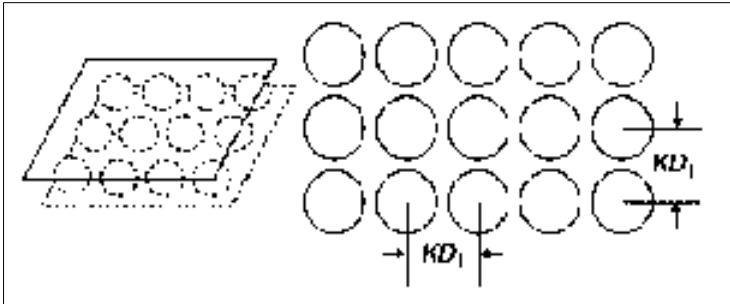


Fig. 5 Proppant placement between plates (Li et al., 2015)

The distance coefficient K is unnecessary to present the model application and therefore disregarded for demonstrating the theoretical background of fracture behavior. **Fig. 6** shows the stress analysis for a single proppant. Comparing **Fig. 6** and **Fig. 4**, it should be noted that the stress unit is [MPa] in **Fig. 6**, but the load unit is [N] in **Fig. 4**.

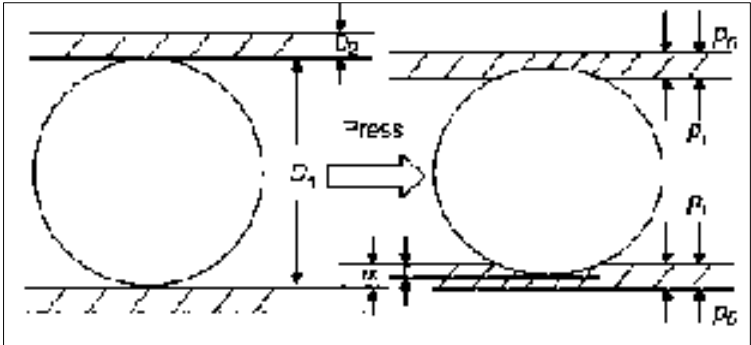


Fig. 6 Stress analysis for a single proppant (Li et al., 2015)

The forces between the plates and proppants are acting on the contact areas, and the following relationship between the load and stress can be derived:

$$P = p(KD_1)^2, \quad (7)$$

where P is the load acting on the contact areas in [N]; p is closure pressure in [MPa], K is distance coefficient, dimensionless; and D_1 is the diameter of proppant, in [mm].

Furthermore, a relationship can be derived for closure pressure which is the difference between overburden pressure and fracturing fluid pressure:

$$p = p_0 - p_i, \quad (8)$$

where p_0 is overburden pressure in [MPa]; and p_i is fluid pressure of fracturing fluid in [MPa].

It should be noted that when $p_0 < p_i$, which happens during the fracturing process - the pressure of fracturing fluid overcomes the in-situ stress of the given rock, fracture aperture is initiated, and fracture starts to propagate -, the proppants neither deform nor embed into the formation. When $p_0 > p_i$, which always happens at the end of the fracturing treatment, - pumps are switched off, and due to this, there is no more extra pressure energy that would exceed the formation's breakdown pressure, so the fracking fluid leaks off, and the pressure drops, - the proppants deform and embed. Equations obtained in the following can be used only when $p_0 > p_i$; in another case, the equations have no practical physical meaning.

The thicknesses of the formation in the upper and lower boundary are the same (**Fig. 6**) and are denoted as D_2 . Therefore, the formation deforms under closure pressure, and the deformation can be calculated according to Hooke's law:

$$\Delta D_2 = D_2 \frac{p}{E_2}, \quad (9)$$

where D_2 is the thickness of the formation, in [mm]; and ΔD_2 is the deformation of the formation, in [mm]. The deformation of the formation is reflected in the form of proppant embedment because the thickness of the formation that does not contact with proppants is returned to the initial value. Substituting **Eq. 7** and **Eq. 9** into **Eq. 4**, one can obtain the following equation:

$$\alpha = 1.04D_1(K^2pC_E)^{\frac{2}{3}} + D_2 \frac{p}{E_2}, \quad (10)$$

where α is the change in fracture aperture, in [mm]. Li et al. (2015) noted that the value of α is half of the change in fracture aperture, but for convenience, it is referred to as a change in fracture aperture. Later, in fracture conductivity calculations, α is the half of the fracture closure and is considered accordingly.

Continuing the substitution (Eq. 7 into Eq. 5; Eq. 7 and Eq. 9 into Eq. 6), one can obtain the following equations:

$$\beta = 1.04D_1(K^2p \frac{1-\nu_1^2}{E_1})^{\frac{2}{3}}, \quad (11)$$

$$h = 1.04D_1(K^2p)^{\frac{2}{3}} \left[\left(\frac{1-\nu_1^2}{E_1} + \frac{1-\nu_2^2}{E_2} \right)^{\frac{2}{3}} - \left(\frac{1-\nu_1^2}{E_1} \right)^{\frac{2}{3}} \right] + D_2 \frac{p}{E_2}, \quad (12)$$

where β is the proppant deformation, in [mm]; h is the proppant embedment, in [mm]; E_1 is the elastic modulus of proppant, in [MPa]; and E_2 is the elastic modulus of the formation, in [MPa].

So far, all the necessary equations have been derived and explained, which is required to investigate the single-layer pattern behavior. However, one should be aware that applying mono-layer patterns during hydraulic fracturing treatment is highly challenging in practice. In addition, a full mono-layer pattern application would not make sense because the conductivity of this type of layer is relatively low compared to multi-layer patterns (Darin & Huitt, 1959). Nevertheless, Darin and Huitt (1959) demonstrated an areal proppant concentration - below a full proppant mono-layer concentration - in which the resulting conductivity is much higher than in the case of a full mono-layer pattern, called partial mono-layer. Furthermore, they found the optimal proppant concentration value of about 0.1 lb/ft² in the case of 20/40 mesh sand at low closure pressure, which is at least a magnitude lower compared to multi-layer patterns with a proppant concentration of about 2 - 4 lb/ft².

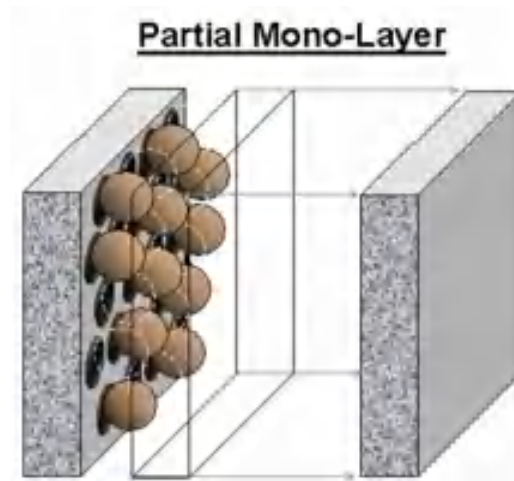


Fig. 7 Partial mono-layer proppant pattern (Brannon et al., 2004)

The application of a partial mono-layer pattern gained real sense when ultra-lightweight proppant was developed in the last decade, facilitating effective proppant transport and limited proppant settlement in the vicinity of the wellbore.

The next chapter presents the sensitivity test results of a mono-layer pattern calculated by the abovementioned equations to show the model's feasibility and the theory behind fracture aperture-closing.

3.2. Mono-layer pattern results

In this section, the application of the derived equations is presented. Several sensitivity tests were conducted in given conditions to present how the factors influence the fracture aperture, proppant embedment, and proppant deformation. In most cases, a reasonably soft formation type was chosen to make the tests more sensitive and highlight the physics behind the interactions between the proppant particles and the rock itself. It means an elastic modulus of 1,100 [MPa], which may represent a coalbed accumulation and anticipate the results of a hydraulic fracturing application in shallow coalbed methane (CBM) formation (Robertson & Christiansen, 2007). The known conditions are noted in every case of the sensitivity analysis to make the tests reproducible. The conditions are defined to represent usual parameters for a fracked well drilled in a compact conventional or a less extreme unconventional hydrocarbon-bearing reservoir. The investigation aims to highlight the physical background of the phenomenon and markup important observations that made the Author aware of focal points and focused on crucial factors in building up the numerical model.

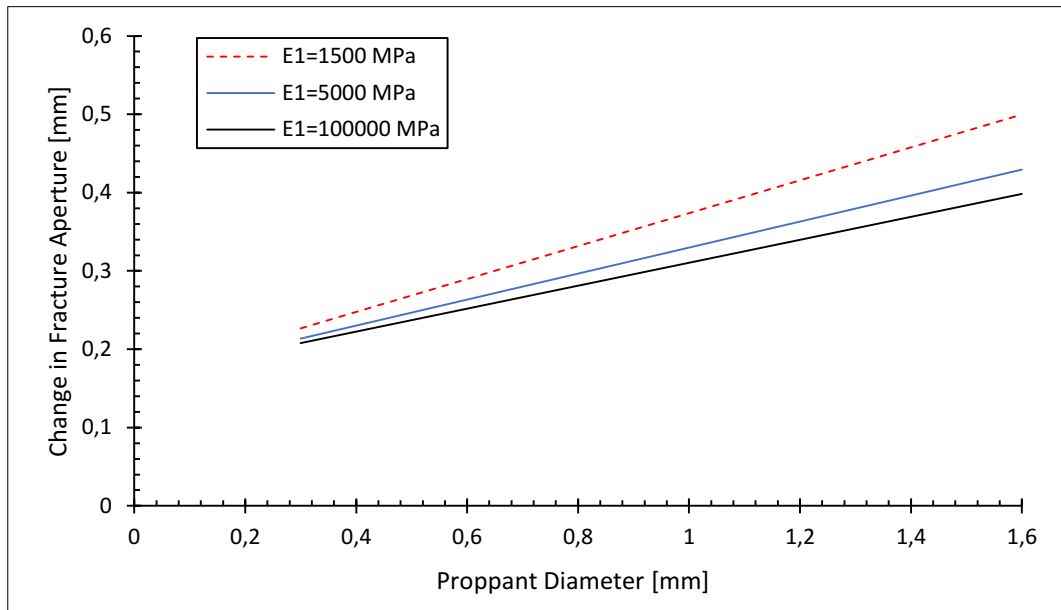


Fig. 8 Relationship between proppant size and fracture aperture (edited by the Author)

The known conditions were taken to be $\nu_1=\nu_2=0.2$, $E_2= 1,100$ [MPa], $D_2=3$ [mm], $p=60$ [MPa] and E_1 was 1,500, 5,000 and 100,000 [MPa]. **Fig. 8** represents the change in fracture aperture as a function of the proppant diameter. It can be observed that a straight line characterizes the relation of the variables. As the proppant diameter increases, the change in fracture aperture is also increasing. On the other hand, with an increasing elastic modulus of proppant, decreasing change in fracture aperture – less deformation– can be realized with the same condition. However, the fracture aperture change increases with the proppant size, which means a greater closure action, i.e., more significant deformation and embedment. One should note that the fracture conductivity increases with the proppant agent's particle size due to the much higher permeability value of greater proppant size. This important remark will be discussed in more detail later.

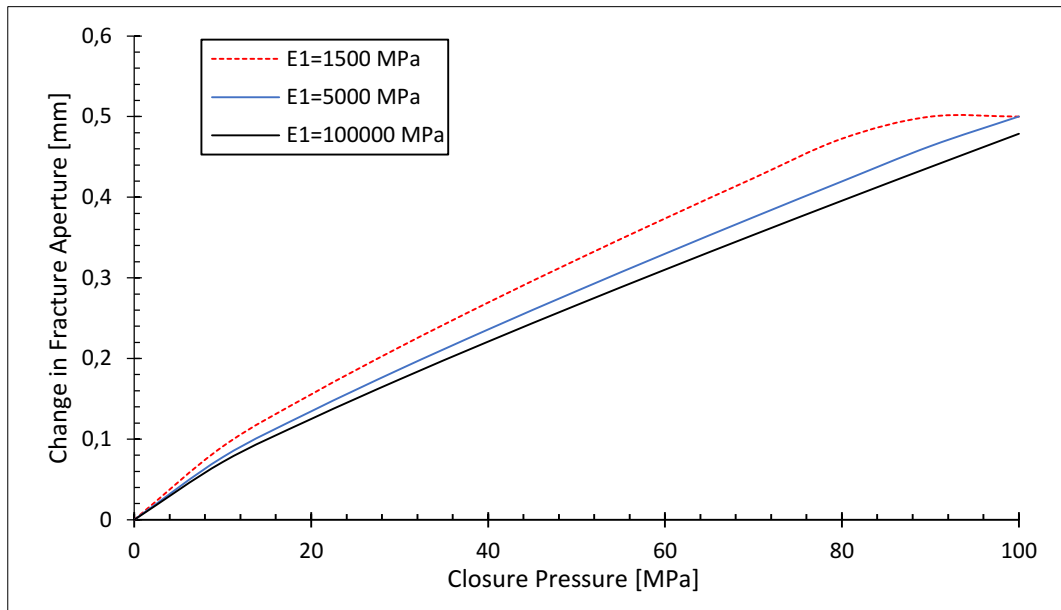


Fig. 9 Change in fracture aperture as a function of closure pressure (edited by the Author)

In the next case, the known conditions were taken to be $\nu_1=\nu_2=0.2$, $E_2= 1,100$ [MPa], $D_1=1$ [mm], $D_2=3$ [mm] and E_1 was 1,500, 5,000 and 100,000 [MPa]. As expected and observed in **Fig. 9**, the fracture closing action is more relevant when the formation closure pressure is higher, or the elastic modulus of the proppant is smaller. It can also be noticed that the change in fracture aperture increases to a specific value, which is the proppant radius, as the proppant diameter was set at 1 [mm]. This situation means a completely closed fracture since, indeed, the change in fracture aperture represents half of the fracture closure.

Two additional tests were conducted to demonstrate the change in fracture aperture as a function of the elastic modulus of proppant and formation. In **Fig. 10**, the relationship between the change in fracture aperture, deformation, embedment, and proppant's elastic modulus can be realized. It was assumed that the known conditions were $\nu_1=\nu_2=0.2$, $E_2= 1,100$ [MPa], $D_1=1$ [mm], $D_2=3$ [mm], and $p= 60$ [MPa]. The proppant deformation approximates zero -, infinite proppant Young's modulus means zero deformation, i.e., the horizontal axis acts as an asymptote of proppant deformation function - while the change in fracture aperture decreases to a specific value. These observations are concluded from the function origin: the change in fracture aperture is the sum of proppant deformation and embedment, and it equals the embedment if the deformation is zero.

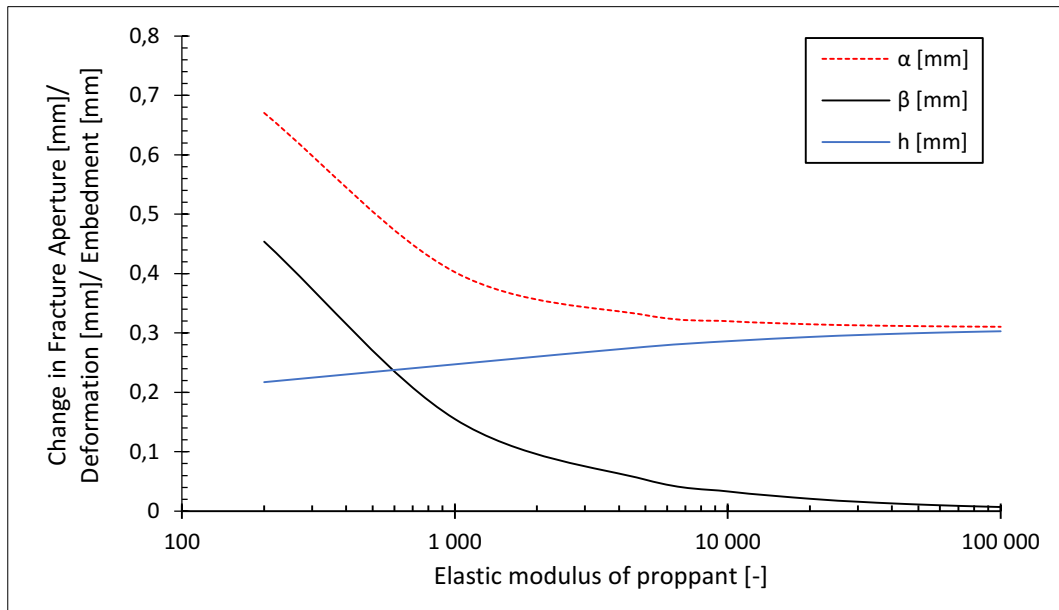


Fig. 10 Relationship between α , β , h and elastic modulus of proppant (edited by the Author)

When the elastic modulus of the proppant is smaller than the elastic modulus of the formation, the proppant particles rather deform than embed. In this case, the proppant deformation is the leading cause of the change in fracture aperture, i.e., the propped fracture closure. On the other hand, when the elastic modulus of the proppant is getting greater, the proppant embedment becomes the main reason for the decrease in fracture aperture since the proppant will be more rigid than the formation, which is a usual situation in practice.

In the next case, the known parameters were defined as $\nu_1=\nu_2=0.2$, $E_1= 10,000$ [MPa] (representing a less tough proppant type), $D_1=1$ [mm], $D_2=3$ [mm], $p= 60$ [MPa] and E_2 ranged from 400 to 100,000 [MPa]. As shown in **Fig. 11**, proppant embedment and the fracture aperture change decrease as the formation's elastic modulus increases. One can also see that proppant deformation is independent of the elastic modulus of formation, and it stays constant since the deformation is influenced only by the elastic modulus of the proppant and the external forces acting on the proppant pack. Proppant embedment is more significant than proppant deformation when the elastic modulus of the proppant is greater than the elastic modulus of the formation, and they are the same when the elastic modulus of the formation reaches the value of about 11,000 [MPa]. After this point, the change in fracture aperture gradually approaches the proppant deformation, and the embedment approximates zero showing the same behavior

as presented in **Fig. 10** . In this case, the formation is tougher than the proppant, and the main cause of the change in fracture aperture is the proppant deformation.

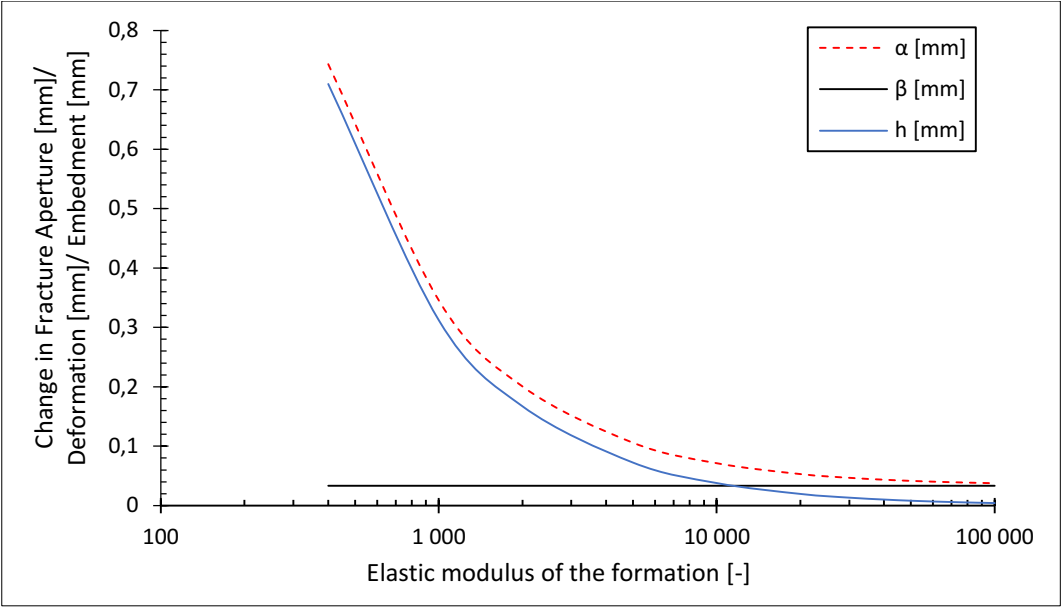


Fig. 11 Relationship between the three variables and the elastic modulus of formation (edited by the Author)

3.3. Multi-layer pattern

In the previous chapter, a single-layer pattern was assumed to present proppant embedment, deformation, and fracture aperture change. However, in practice, the multi-layer pattern is more common to be developed during the hydraulic fracturing process instead of the mono-layer pattern. Furthermore, during general fracturing treatments, the proppants squeeze mutually, and also the interaction between proppant and formation takes place; therefore, it is also necessary to analyze the deformation and embedment between proppants.

3.3.1. Interaction of proppants

By the derivation of equations used to calculate proppant embedment and deformation, the radius of Sphere 1 and 2 is considered to be equal. This approximation solves the model's mathematics and lets the problem be described analytically; however, this generous assumption also limits the model. Nevertheless, this finding is one of the issues that made the Author confident to proceed with a numerical solution of the propped fracture behavior modeling.

In case the radius of Sphere 1 and 2 are the same, i.e., $R_1=R_2=R$, **Eq. 3** can be reduced to:

$$\alpha' = \frac{2(\frac{3}{8}PC_ER)^{\frac{2}{3}}}{R}, \quad (13)$$

where α' is the change in distance between the centers of Sphere 1 and 2, in [mm]; and R is the radius of Sphere 1 and 2, in [mm]. The deformation of Sphere 1 and 2 is expressed as:

$$\beta_1 = \frac{(\frac{3}{8}PR)^{\frac{2}{3}}(2\frac{1-\nu_1^2}{E_1})^{\frac{2}{3}}}{R}, \quad (14)$$

$$\beta_2 = \frac{(\frac{3}{8}PR)^{\frac{2}{3}}(2\frac{1-\nu_2^2}{E_2})^{\frac{2}{3}}}{R}, \quad (15)$$

where β_1 and β_2 are the deformations of Sphere 1 and 2 respectively, in [mm]. As previously applied in deriving the embedment of Sphere and plate - in **Eq. 6**, the deformation was separated from the change in fracture aperture - the embedment of the Spheres is calculated by combining **Eq. 13**, **Eq. 14**, and **Eq. 15**.

$$h = \alpha' - \beta_1 - \beta_2 = \frac{(\frac{3}{8}PR)^{\frac{2}{3}}}{R} \left[2\left(\frac{1-\nu_1^2}{E_1} + \frac{1-\nu_2^2}{E_2}\right)^{\frac{2}{3}} - \left(2\frac{1-\nu_1^2}{E_1}\right)^{\frac{2}{3}} - \left(2\frac{1-\nu_2^2}{E_2}\right)^{\frac{2}{3}} \right], \quad (16)$$

where h is the embedment between Sphere 1 and 2, in [mm].

Fig. 12 and Fig. 13 represent the results gained using **Eq. 13**, **Eq. 14**, **Eq. 15**, and **Eq. 16**. The known conditions were taken to be $\nu_1=\nu_2=0.2$, $E_2= 1,500$ [MPa], $R_1=R_2=R= 0.5$ [mm], $P= 60$ [N]. **Fig. 12** shows how the change between the centers of Spheres decreases as the elastic modulus of Sphere 1 increases and how the deformation of Spheres 1 and 2 changes in the function of E_1 .

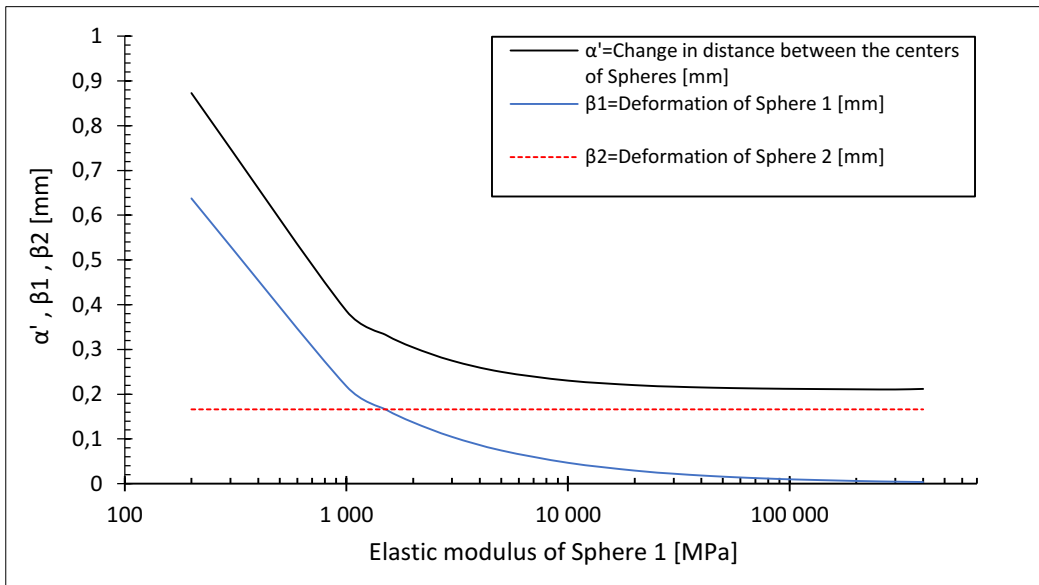


Fig. 12 Relationship between the three variables and the elastic modulus of Sphere 1 (edited by the Author)

One can observe that the change in distance between the centers of Spheres and the deformation of Sphere 1 decreases with an increasing elastic modulus of Sphere 1. Sphere 2 deformation is constant because it is independent of the elastic modulus of Sphere 1.

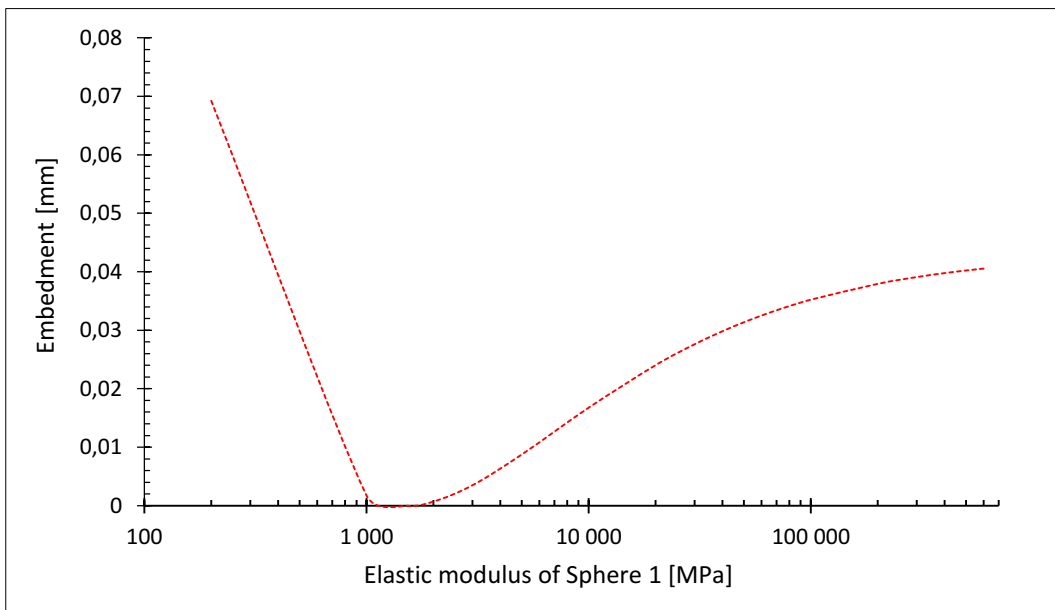


Fig. 13 Relationship between embedment and elastic modulus of Sphere 1 (edited by the Author)

Fig. 13 demonstrates that the embedment (Sphere 2 embedding into Sphere 1) decreases as the elastic modulus of Sphere 1 increases until the elastic modulus of Sphere 2 exceeds the elastic modulus of Sphere 1. When $E_1 = E_2$, the embedment equals zero, and the contact area of

the mutually squeezed spheres is a plane. When E_1 gets greater than E_2 , the embedment (Sphere 1 embedding into Sphere 2) increases but at a lower rate as before since one of the elastic moduli is greater than earlier. **Fig. 12** and **Fig. 13** demonstrate that the leading cause of change in distance between the centers of spheres is the deformation and not the embedment.

3.3.2. Embedment of multi-layers

The interaction between proppant and formation was presented up to this section, i.e., the mono-layer situation and the interaction between proppants; however, the proppants are mostly paved in multiple layers in practice; therefore, it is necessary to analyze the proppant embedment into the rock in case of a multi-layer pattern.

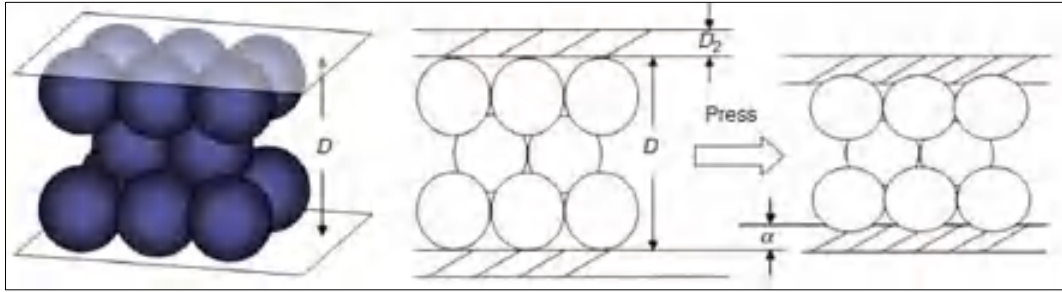


Fig. 14 Proppant paving in multiple layers (Li et al., 2015)

As shown in **Fig. 13**, there is no proppant embedment between proppants when the elastic modulus and the size of proppants are the same, which means that only proppant deformation and embedment into the formation have an effect if uniform proppant particles are considered. In the case of a multi-layer pattern, the deformation can be approximated as the superposition of each proppant layer's deformation. At the same time, the proppant embedment (into the formation and not into each other) is the same as in the case of a single-layer pattern because only the top and the bottom layer are in direct contact with the rock surface. Based on the previous assumptions and the single-layer pattern model, the corresponding equations can be expressed as follows:

$$\alpha = 1.04D(K^2p)^{\frac{2}{3}} \left\{ \left(\frac{1-\nu_1^2}{E_1} \right)^{\frac{2}{3}} + \frac{D_1}{D} \left[\left(\frac{1-\nu_1^2}{E_1} + \frac{1-\nu_2^2}{E_2} \right)^{\frac{2}{3}} - \left(\frac{1-\nu_1^2}{E_1} \right)^{\frac{2}{3}} \right] \right\} + D_2 \frac{p}{E_2}, \quad (17)$$

$$\beta = 1.04D(K^2p)^{\frac{2}{3}} \left(\frac{1-\nu_1^2}{E_1} \right)^{\frac{2}{3}}, \quad (18)$$

$$h = 1.04D_1(K^2p)^{\frac{2}{3}} \left[\left(\frac{1-\nu_1^2}{E_1} + \frac{1-\nu_2^2}{E_2} \right)^{\frac{2}{3}} - \left(\frac{1-\nu_1^2}{E_1} \right)^{\frac{2}{3}} \right] + D_2 \frac{p}{E_2}, \quad (19)$$

where D is the initial fracture aperture - shown in **Fig. 14** , in [mm]; α is the change in fracture aperture of multi-layer pattern, in [mm]; β is the proppant deformation of multi-layer pattern, in [mm]; and h is the proppant embedment into the formation of a multi-layer pattern, in [mm].

3.3.3. Multi-layer results

In the following, two examples are introduced to demonstrate the results of the above-derived equations (Eq. 17, Eq. 18, and Eq. 19). Fig. 15 demonstrates how the proppant embedment, deformation, and the change in fracture aperture vary with increasing proppant size. The known parameters were taken to be $\nu_1=\nu_2=0.2$, $E_1= 10,000$ [MPa], $E_2= 1,100$ [MPa], $p= 20$ [MPa], $D= 5$ [mm], $D_2=20$ [mm] and the proppant diameter ranged from 0.2 to 1.6 [mm]. Substituting these values into Eq. 17, Eq. 18, and Eq. 19, one can observe that deformation is constant while proppant embedment and the change in fracture aperture linearly increases as the proppant diameter increases. An important conclusion of the sensitivity test is that the deformation is not affected by the proppant diameter, while the fracture closure is still the sum of the deformation and embedment.

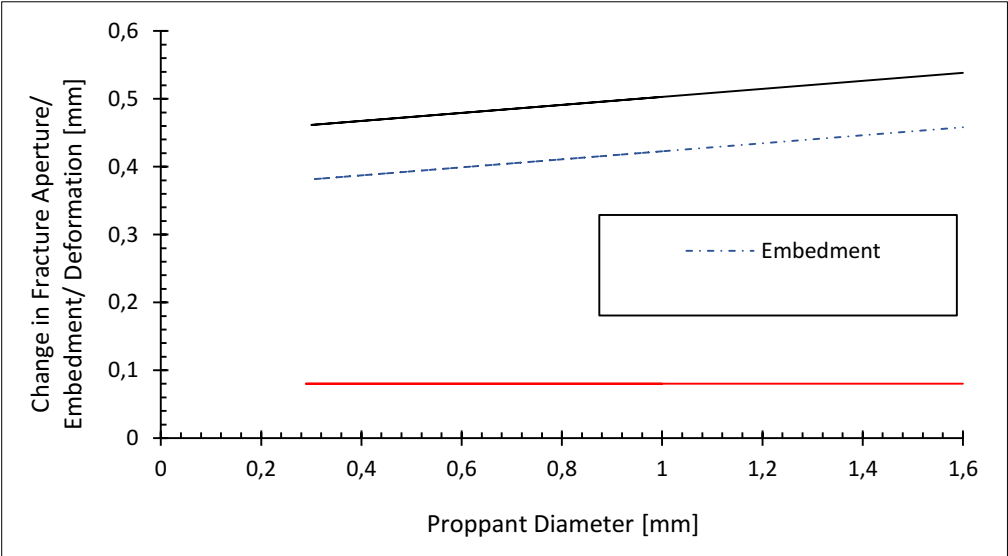


Fig. 15 Relationship between the three variables and proppant diameter (edited by the Author)

Fig. 16 demonstrates how the proppant embedment, deformation, and the change in fracture aperture alter with closure pressure. The known parameters were taken to be $\nu_1=\nu_2=0.2$, $E_1= 10,000$ [MPa], $E_2= 2,000$ [MPa], $D= 5$ [mm], $D_1=1.328$ [mm], $D_2=20$ [mm] and the closure pressure ranged from 0 to 20,000 [psi]. Substituting these values into **Eq. 17**,

Eq. 18, and **Eq. 19**, one can observe that each variable increases as the closure pressure increases. Since the elastic modulus of the proppant is high compared to the formation's Young's modulus, the main cause of the change in fracture aperture is the proppant embedment.

So far, the mechanical investigation of monolayer and multi-layer patterns was presented based on the Hertzian Contact Theory extended and specialized by Li et al. (2015). The observations of the sensitivity analysis aided the Author in gaining the basics of propped fracture behavior and highlighted the critical factors on which the numerical model was based. Although the mechanical investigation was performed, the results should be interconnected with the discipline of fluid dynamics to examine fracture conductivity.

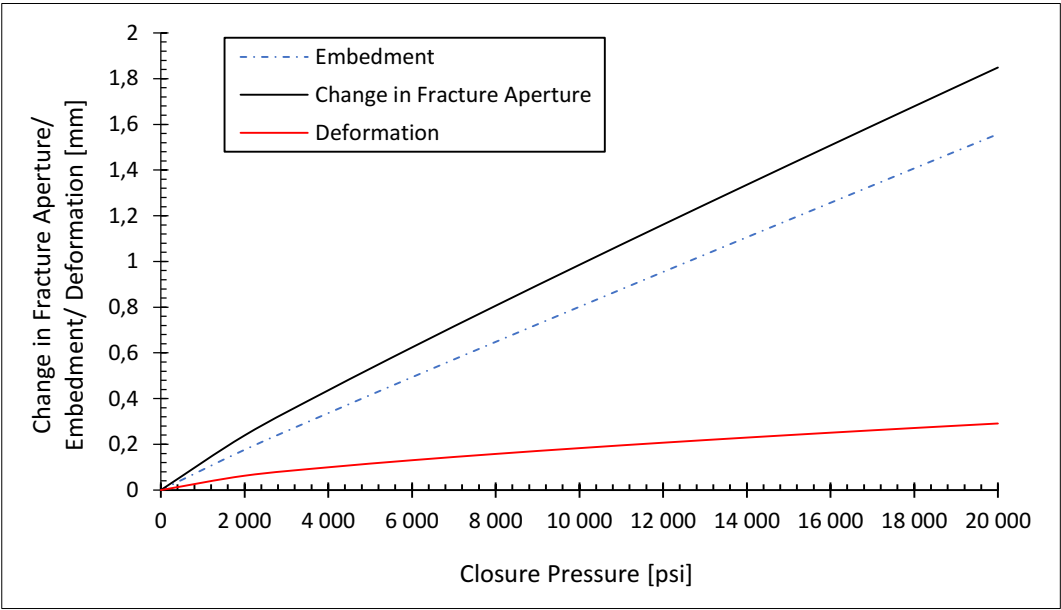


Fig. 16 Relationship between the three variables and closure pressure (edited by the Author)

3.4. Fracture conductivity

The fracture conductivity is the product of fracture permeability and fracture width. The permeability of a propped fracture - as the permeability of all kinds of porous media - is related to its porosity, radius of pore throat, and pore tortuosity. These parameters are influenced by the factors (proppant embedment, proppant deformation, and the change in fracture aperture) presented in the previous chapters.

3.4.1. Derivation

Based on the well-known Kozeny-Carmen tube model - demonstrated in **Fig. 17** -, the permeability can be expressed as:

$$k = \frac{\Phi r^2}{8\tau^2}, \quad (20)$$

where k is permeability, in [$\mu\text{m}^2=1$ Darcy]; Φ is the porosity, dimensionless; r is the radius of pore throat, in [μm]; and τ is the pore tortuosity, dimensionless. Tortuosity can be defined in several different ways, but for simplification, it is the ratio of actual flow path length to the straight distance between the ends of the flow path.

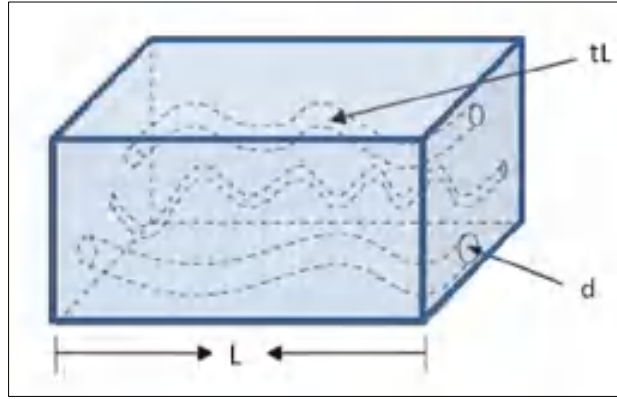


Fig. 17 Capillary tube model (Balázs, 2013)

For the proppant pack shown in **Fig. 14** , disregarding the pore-distribution differences in the layers, the equations of porosity, the radius of pore throat, and pore tortuosity can be derived for the case when the closure pressure is equal to zero. The equations are:

$$\phi_0 = \frac{4\sqrt{2}R_1^3 - \frac{4}{3}\pi R_1^3}{4\sqrt{2}R_1^3} = 0,25951, \quad (21)$$

$$r_0 = 1000 \frac{2\sqrt{3}-3}{3} R_1, \quad (22)$$

$$\tau_0 = \frac{\sqrt{\left(\frac{2}{3}R_1\right)^2 + \left(\frac{\sqrt{2}}{3}R_1\right)^2}}{\frac{2}{3}R_1} = \frac{\sqrt{6}}{2}, \quad (23)$$

where Φ_0 is the porosity of the proppant pack when closure pressure is equal to zero, dimensionless; r_0 is the radius of pore throat when closure pressure is equal to zero, in [μm]; τ_0 is the pore tortuosity when closure pressure is equal to zero, dimensionless; R_1 is the radius of proppant, in [mm].

When closure pressure is greater than zero, the porosity, radius of pore throat, and pore tortuosity approximately satisfy the following relationships (Li et al., 2015):

$$\phi = \frac{D\phi_0 - 2\beta}{D - 2\beta}, \quad (24)$$

$$r = \left(\frac{D - 2\beta}{D}\right) r_0, \quad (25)$$

$$\tau = \sqrt{\left(\frac{D - 2\beta}{D}\right)^2 (\tau_0^2 - 1) + 1}, \quad (26)$$

where β is the proppant deformation calculated by **Eq. 18** in [mm], and D is the initial fracture aperture in [mm]. According to the concept of fracture conductivity and combining **Eq. 21**, **Eq. 25**, **Eq. 26**, and **Eq. 27**, the following equation can be obtained:

$$F_{CD} = kW = \frac{(D\phi_0 - 2\beta)(D - 2\beta)r_0^2}{80\left[\left(\frac{D - 2\beta}{D}\right)^2 (\tau_0^2 - 1) + 1\right]D^2} (D - 2\alpha), \quad (27)$$

where F_{CD} is the fracture conductivity, in [$\mu\text{m}^2 \cdot \text{cm}$]; w is the fracture aperture under closure pressure, in [cm]; and α is the half of the change in fracture aperture calculated by **Eq. 17**, in [mm].

3.4.2. Analysis

The main influencing factors that impact fracture conductivity are the closure pressure, proppant size, the elastic modulus of proppant and formation, Poisson's ratio of proppant and formation, and initial fracture aperture. The following charts attempt to describe and demonstrate the indicators' effect to present the most important relations.

3.4.2.1. Proppant Size

Fig. 18 shows the results according to the parameters: $\nu_1 = \nu_2 = 0.2$, $E_2 = 2,000$ [MPa], $D = 5$ [mm], $D_2 = 20$ [mm], $p = 20$ [MPa], E_1 ranged from 2,000 to 100,000 [MPa], and the proppant diameter ranged from 0.3 to 1.6 [mm].

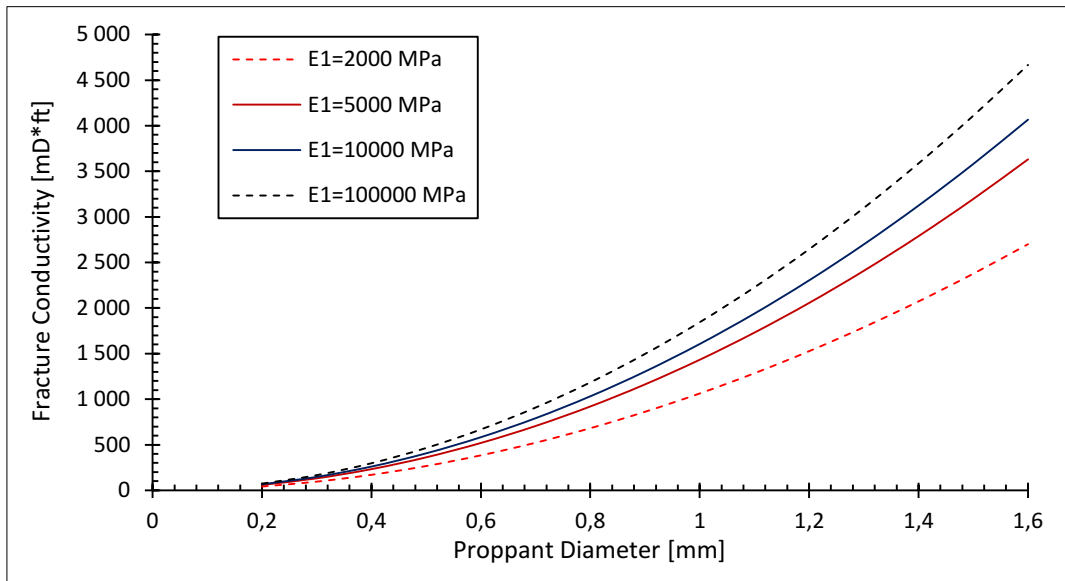


Fig. 18 Conductivity as a function of proppant diameter (edited by the Author)

Investigating **Fig. 18**, one can observe that a greater proppant diameter produces higher fracture conductivity. Meanwhile, in the previous examples, increasing proppant size resulted in greater embedment, deformation, and fracture closure. The concept of proppant permeability explains it, i.e., the greater the proppant, the higher the permeability. In **Eq. 27**, one can perceive that the fracture conductivity depends on the square of the pore throat calculated at zero closure pressure. Nevertheless, the value of pore throat depends on the proppant diameter. Therefore, the proppant size affects the permeability more than the proppant embedment and deformation. The fracture conductivity's dependence on the proppant's elastic modulus can also be observed in **Fig. 18**. The greater the proppant's elastic modulus, the higher the value of fracture conductivity since the proppant deformation is less prominent, resulting in higher pore space that affects the permeability expressively.

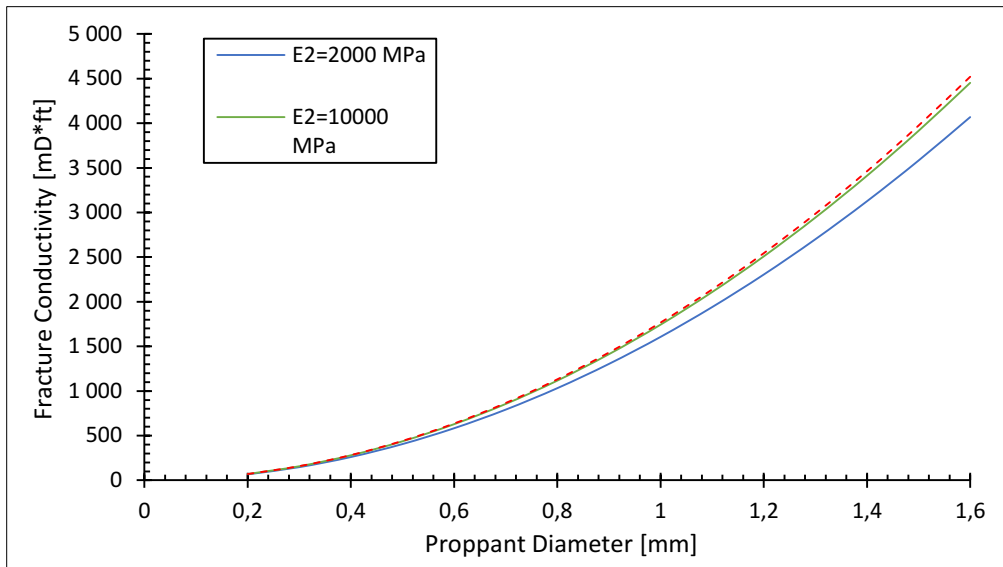


Fig. 19 Fracture conductivity in the function of proppant diameter (edited by the Author)

For presenting **Fig. 19**, the same condition was taken as in the case of **Fig. 18**, and the only difference is that E_1 was set at 10,000 [MPa] and E_2 ranged from 2,000 to 30,000 [MPa]. The main conclusion of this figure is that the elastic modulus of formation has less impact on fracture conductivity than the elastic modulus of proppant in the previous case. Therefore, one can conclude there is no difference in fracture conductivity values in the case of the elastic modulus of the formation being 10,000 and 30,000 [MPa].

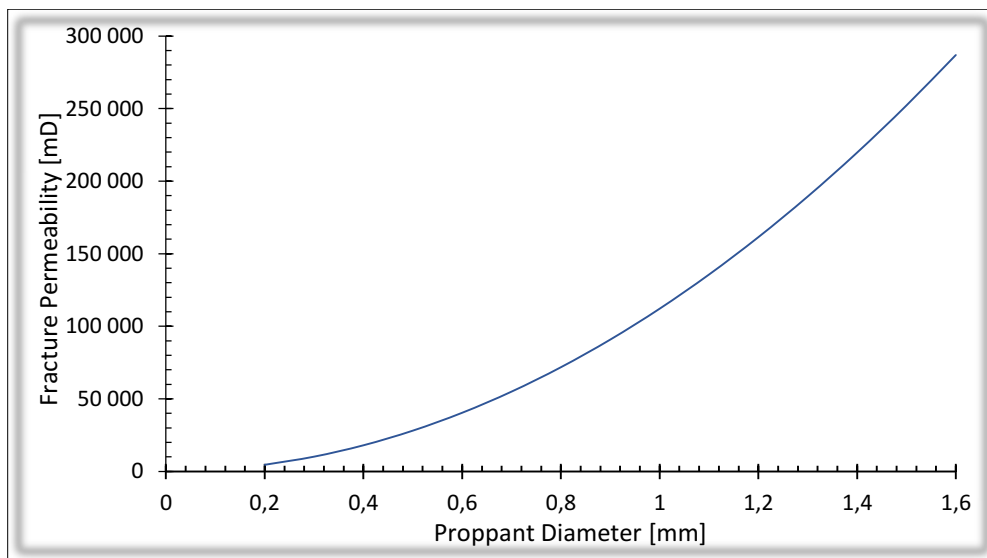


Fig. 20 Fracture permeability in the function of proppant diameter (edited by the Author)

Fig. 20 was performed to demonstrate the phenomenon described in the case of **Fig. 18** . The fracture permeability increases exponentially with the proppant diameter, highlighting the effect of proppant agent size on fracture conductivity exceeding the contrary impact on fracture width, as illustrated in **Fig. 15** .

3.4.2.2. Formation stress

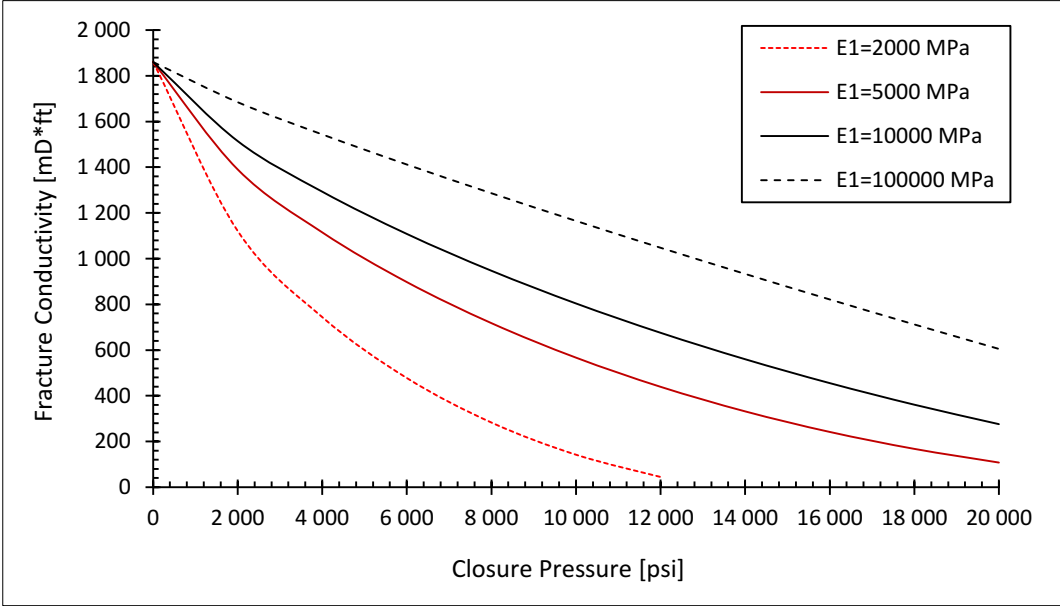


Fig. 21 Fracture conductivity in the function of closure pressure (edited by the Author)

In **Fig. 21** the known conditions were taken to be $\nu_1=\nu_2=0.2$, $E_2=2,000$ [MPa], $D=5$ [mm], $D_1=0.936$ [mm], $D_2=20$ [mm], E_1 ranged from 2,000 to 100,000 [MPa], and closure pressure ranged from 0 to 20,000 [psi]. An important observation can be that the impact of formation closure pressure dramatically affects the resulting fracture conductivity. Another apparent point is the proppant toughness. The theoretical proppant with Young’s modulus of 2,000 [MPa] is compressed totally at the closure stress of 12,000 [psi]. Conductivity values vary broadly in respect of different proppant Young’s modulus, which is an important conclusion of this figure.

The conditions demonstrated in **Fig. 22** were taken to be $\nu_1=\nu_2=0.2$, $E_1=10,000$ [MPa], $E_2=2,000$ [MPa], $D=5$ [mm], $D_2=20$ [mm], proppant size ranged from 12/18 mesh to 40/70 mesh and p ranged from 0 to 20,000 [MPa]. Fracture conductivity decreases when closure pressure increases, and it can also be observed that significantly higher fracture conductivity

values can be achieved with greater proppant size. However, when closure pressure increases, the differences between fracture conductivity values related to different proppant sizes become smaller, balancing the advantage of applying bigger proppants over small ones.

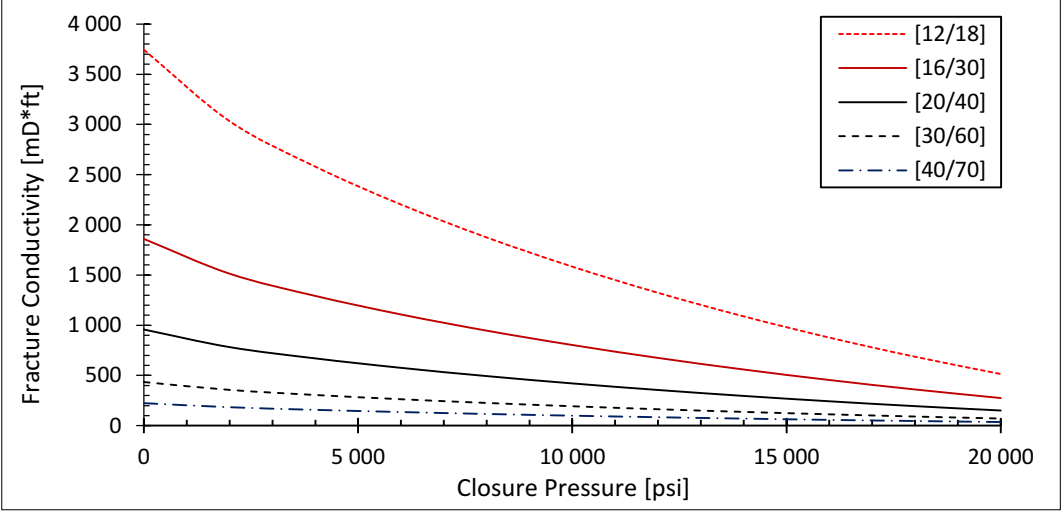


Fig. 22 Fracture conductivity in the function of closure pressure and proppant size (edited by the Author)

In **Fig. 23**, the same conditions are valid as in **Fig. 22**. Similar trend of the lines is expected, but the curves' steepness is more declivous than in the case of fracture conductivity. This observation can be explained by the impact of formation stress on fracture width, i.e., with increasing closure pressure, not only the fracture permeability but also the fracture width decreases.

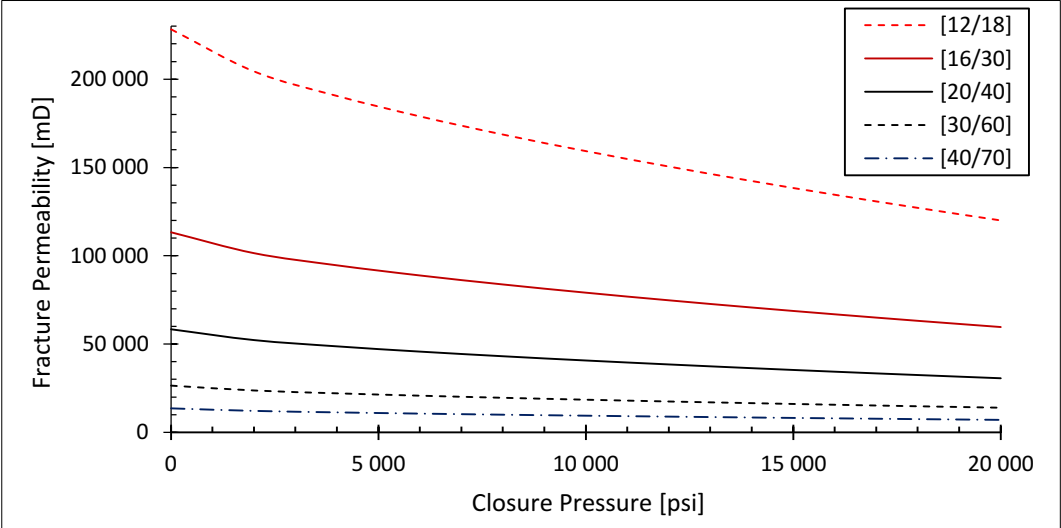


Fig. 23 Fracture permeability in the function of closure pressure (edited by the Author)

3.4.2.3. Initial Fracture Aperture

In practice, influencing the size of fracture width is quite tricky. The size of fracture aperture is the consequence of many factors like in-situ stress condition of the formation to be fracked, the bottom hole pressure boosted by the complex system of high power hydraulic pumps on the surface (which fluctuates many times), the effectiveness of proppant transport, TSO (Tip Screen-out), etc. These parameters are out of exact control, resulting in technical limitations for influencing the fracture aperture in the case of hydraulic fracturing.

The sensitivity analysis presented in **Fig. 24** was performed to show the effect of initial fracture aperture on conductivity. The known conditions for the analysis are the same as in the previous example in **Fig. 22**. This test resulted in a vital conclusion: the fracture conductivity is vastly dependent on the initial fracture aperture entailing the intention of fracturing engineers in creating fractures as thick as possible limited by the factors described below.

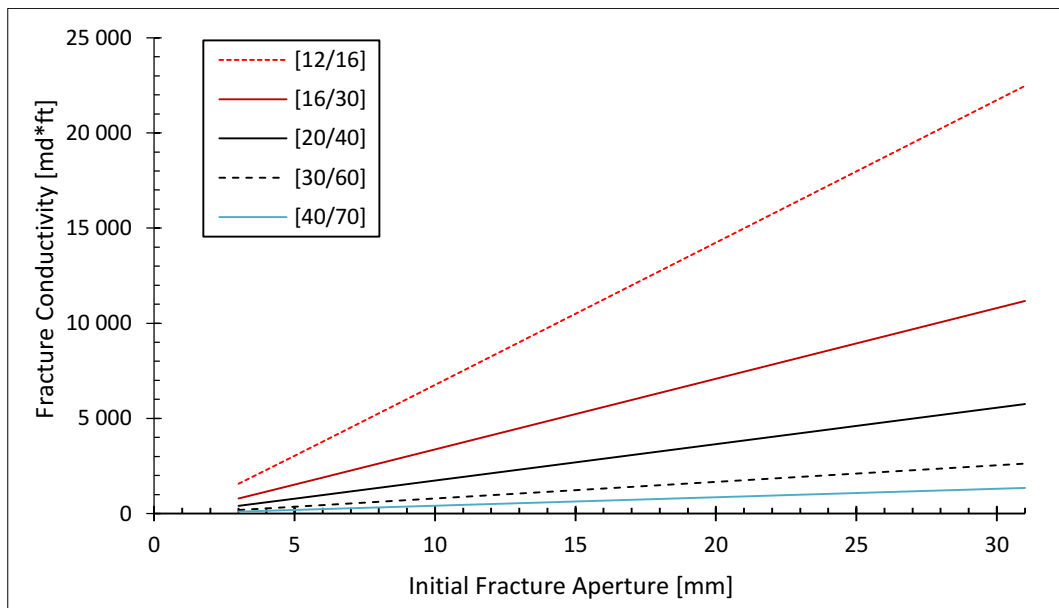


Fig. 24 Fracture conductivity in the function of initial fracture aperture (edited by the Author)

3.5. Key Factors

The analytical model, introduced and described in this chapter, could give a good approximation of the proppant embedment, proppant deformation, and the sum of these: the change in fracture aperture in an elegant way using the Contact Theory developed by Heinrich

Hertz in 1881 (Hertz, 1881). Moreover, the fracture conductivity can also be computed by combining the model with the Kozeny-Carmen approach.

Using the analytical model, sensitivity tests could be performed to investigate the impact of factors. Investigating the outcomes, one can conclude that the closure pressure vastly influences proppant embedment and deformation. Furthermore, the impact of the elastic modulus of proppant and formation was also tested, and the results showed that Young's modulus of proppant has a more significant effect on the change in fracture aperture than Young's modulus of the formation.

Tests were also conducted to examine the influencing factors of fracture conductivity. In conclusion, it can be stated that the fracture conductivity increases with increasing proppant size, initial fracture aperture, and the elastic modulus of formation and proppant, and it decreases with increasing formation closure pressure.

The Hertz model used for the analytical investigation of proppant embedment and deformation is based on assumptions that limit the accuracy of the outcomes. For example, the model supposes perfect spheres with the same diameter for all the particles; however, the granular media is sorted by sieves with a given size distribution, and their shape is characterized by sphericity and roundness indices. Furthermore, the model supposes perfectly even proppant pavement being the particles one-point-contacted and squeezed, i.e., uniform stress distribution. Another boundary condition of the model is the assumption of no friction between the particles, i.e., no tangential displacement component - friction traction - is considered. Moreover, the Hertz model supposes that the contact surface developed between the contacting objects is flat; nonetheless, it is only valid if the same materials are considered; otherwise, the stiffer body deforms into the softer object, which is the case of the contact of proppant and the rock surface. In addition, the model is based on infinitesimal strain assumptions, which may conclude errors due to geometrical nonlinearities of finite deformation (Dintwa, 2007). Another limiting factor is the assumption of the Kozeny-Carman model, i.e., it is only useable for laminar flow. The deviation between the analytical model and experiments are demonstrated in **chapter 4.7.2.3**, in **Fig. 84 Fig. 85 Fig. 86** highlighting the limitation of the model.

Performing the experiments and acquiring the knowledge of the outcomes which highlighted, inter alia, the randomness of the phenomenon and the discrepancies described above, the more detailed investigation of a propped fracture behavior can only be executed by numerical modeling. Therefore, the points to be examined by numerical solutions are:

- Uneven proppant placement in typical fracture geometry - implementing contact models including friction - entailing multi-point-contacted particles and non-uniform stress distribution within the bodies.
- Different proppant diameters within a given propped fracture, i.e., applying the particle size distribution characteristic of the granular media determined by typical sieve analysis.
- Proppant geometry analysis including non-regular particle shapes differing from spheres
- Permeability and conductivity based on computational fluid dynamics (CFD), which can compound the pressure difference of the flowing media within the porous space represented by the proppant pack with an arbitrary particle arrangement.

4. NUMERICAL MODEL²

This chapter presents the second part of materials and methods developed by the Author to establish a numerical model to analyze propped fracture behavior during his Ph.D. research activities. The session is a comprehensive overview and a technical manual, including the physics of model build-up, the numerical methods used and coupled, the modeling process workflow, the results, and validation.

4.1. Model Physics

4.1.1. Geometry

During the building up of the model concept, a conventional vertical well was considered to be fractured. In a vertical well, a classic bi-wing fracture formation takes place (assuming ideal in situ stress conditions) with the dimensions of fracture height, width, and half-length. In the 20th century, 2D models were developed and used for hydraulic fracture simulation. Basically, three models were used: radial, KGD³, and PKN⁴, where KGD and PKN are named after their inventors.

Various radial models were introduced, but all could be characterized by a fracture height directly related to fracture length and described by the radius. The KGD model, introduced by Zheltov and Khristianovic (1955), uses a fixed fracture height and a width proportional to the fracture length. Perkins and Kern (1961) developed the PKN model, and it assumes a constant fracture height as well but a proportional fracture width to the fracture height. However, these models were used widespread, the desire for a more sophisticated solution arrived, and 3D models came into prominence. In the Author's coupled model, an elliptical fracture was created to consider the TSO (Tip Screenout) effect and represent flow patterns occurring in that case. **Fig. 25** illustrates the schematic of the model geometry.

² The chapter is based on the article of "Coupled Numerical Method to Model Propped Fracture Behavior" (Lengyel et al., 2021) with the permission of the Journal's Editor and the Co-Authors

³ Khristianovic-Geertsma-de Klerk

⁴ Perkins-Kern-Nordgren

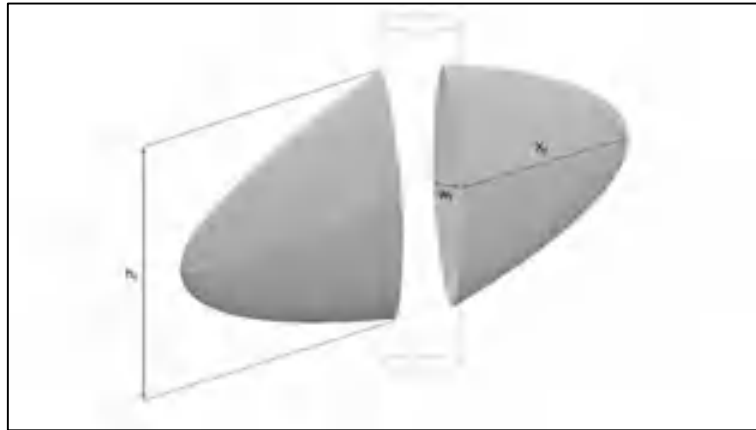


Fig. 25 Elliptical bi-wing fractures in a vertical well (edited by the Author)

In reality, even with available micro-seismic data, simplifications are applied to model the hydraulic fracture. The main examined parameter, the fracture conductivity, is the product of permeability and fracture width, which enables one to investigate the phenomenon in a scaled-down but representative environment. According to the fluid dynamics, permeability does not depend on the spatial dimensions allowing the fracture length and height reduction, which may take more than 100 and 40 [m] in a well, respectively. Considering the complexity of the industrial problem and the calculation limit of both the software and computers - even supercomputers - a pragmatic approach was applied, and the fracture geometry was defined as presented in **Fig. 26** , where the fracture length is 27 [cm], the fracture height is 32.4 [cm], and the fracture width is 6.48 [mm].

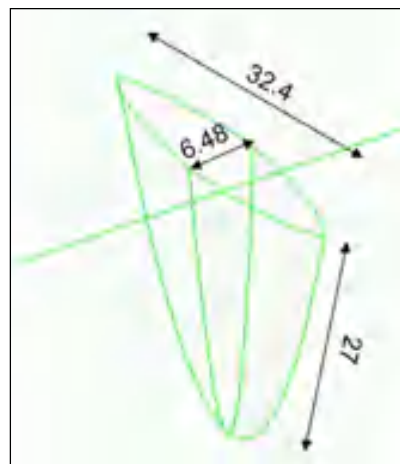


Fig. 26 Model geometry (edited by the Author)

4.1.2. Reservoir & Proppant

As described in the introduction, the fracture conductivity is investigated after hydraulic fractures are created, propped, and the high-pressure hydraulic pumps placed at the surface are stopped, entailing the formation to close again. Boundary conditions for the reservoir and the proppant itself were defined to investigate the behavior of the fracture.

The hydrocarbon-bearing reservoir characteristics directly impact the Young's modulus and Poisson's ratio of the formation, closure pressure, fluid pressure, and fluid flow. Therefore, the boundary condition for Young's moduli of rock was defined for a wide range providing an environment to investigate the effect of formation elasticity to proppant embedment and fracture conductivity in soft, well-consolidated, or even tough deposits, igneous or metamorphic rocks. The minimum value for formation Young's moduli was defined as 2 [GPa] according to the research conducted by Lacy et al. (1997), who examined proppant embedment and fracture conductivity in soft formations. Max and mean values were defined as 30, and 15 [GPa] referred to the scientific work conducted by Malkowski and Ostrowski (2017), in which more than 500 core samples have been measured to determine Young's moduli of rock. Since Poisson's ratio of the reservoir does not have a significant influence on the examined phenomenon, it was fixed to 0.22 [-], referring to the article published by Chan et al. (2018). The latter studied the depth of proppant embedment in hydraulic fractures.

For the relation of overburden, pore, and closure pressure, the widely known Hubbert and Willis formula was used (Hubbert & Willis, 2003):

$$\sigma_c = \nu / (1 - \nu) * (\sigma_v - \alpha p_r) + \gamma p_r \quad (28)$$

where σ_c is closure stress [MPa], ν is Poisson's ratio [-], σ_v is overburden or vertical stress [MPa], γ is Biot's poroelastic constant [-], and p_r is pore pressure [MPa]. One should note that this equation proposes that the uniaxial vertical strain generates the in situ horizontal stress without any tectonic activity. The pore pressure in the reservoir is supposed to be hydrostatic. In contrast, the overburden pressure was considered by the weight of the rocks assuming a medium sandstone density of 2.67 [g/cm³] according to Alvaro and Jimenez (2003) who studied rock moduli and density determination using wireline data. Finally, the limits of closure pressure values were defined as 2,000 and 12,000 [psi]. These closure pressure values cover a

wide range for investigating the effect of closure pressure in a shallow, medium, and even deep well with high overburden pressure.

Another relevant parameter to investigate the fracture behavior and conductivity is the fluid flow in the fracture. In the case of hydraulic fracturing, several flow regimes are interpreted during the production period of the well. Cinco et al. (1978) defined four flow patterns for hydraulically fractured wells: fracture linear flow, bilinear flow, formation linear flow, and pseudo-radial flow, as shown in **Fig. 27**. The conductivity is independent of the flow patterns and can be used for all the cases.

Although the flow rate in the model can be changed, this parameter's investigation was eliminated from the research to make the outcomes comparable. Instead, the mass flow rate was fixed to 1.74 [g/min], proportional to the scaled-down fracture dimensions, meaning an approximated water flow rate of 0.6 [m³/h] projected to a fracture with 10 [m] height, 50 [m] length, and 6.48 [mm] width.

Since permeability is independent of the medium (both the Darcy and the Navier-Stokes equation contain fluid physical properties: viscosity and density), water with 2 [%] of KCl content was applied in the CFD model because its rheological parameters are well-known. As a result, the water's density and viscosity flowing through the propped fracture were 998 [kg/m³] and 0.001003 [Pas].

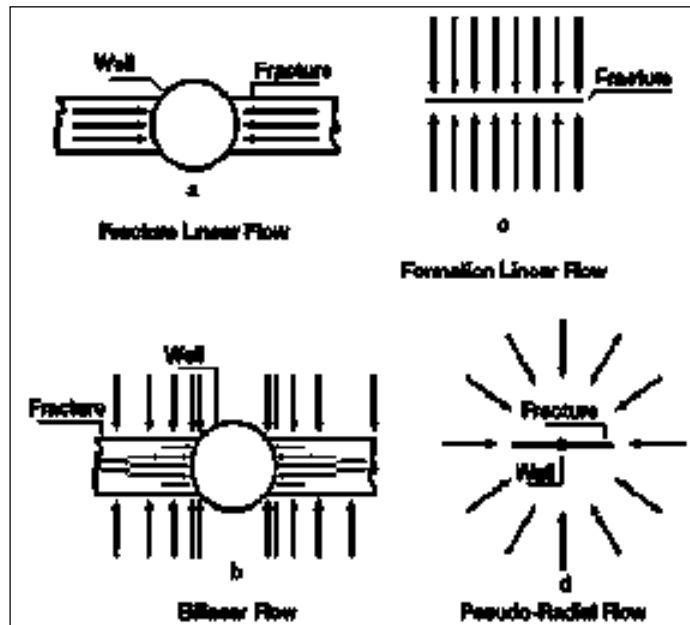


Fig. 27 Flow regimes (Cinco et al., 1978)

Proppant mechanical characteristics were defined after Chen et al. (2018), who examined proppant with Young's modulus of 41,306 [MPa], Poisson's ratio of 0.25, and proppant density of 2.8 [g/cm³]. Proppant geometry was considered to be spherical; however, the application of non-regular geometry was also examined. Simulations were run for cases of the proppant particle diameter of 0.720 [mm], 1.004 [mm], and 1.417 [mm], which sizes represent the average proppant size in a wide range of available proppants on the industrial market: 20/40, 16/30, 12/18, respectively.

4.2. Discrete Element Model

The Ph.D. research focuses on propped fracture conductivity analysis, for which the physical model was introduced and described above. The following chapters explain the numerical tools used to model the phenomenon with its randomness.

Based on the conclusions drawn, using the analytical model - summarized in **chapter 3.5** - and the fact that proppant is a granular media, Discrete Element Modeling was applied to accomplish the original geometry, which describes random proppant placement in the fracture just as it is developed during a hydraulic fracking treatment.

Examining the propped hydraulic fracture, one can identify the interactions of three materials, the reservoir rock (i.e., the fracture wall), the proppant particles which prevent the fracture closure that would occur due to the in-situ stress condition, and the medium flowing through the proppant particles in the direction of well bottom. Proppant is a granular media, i.e., it consists of small, discrete, solid particles which constitute a conglomeration of the granular material having a relevant extent compared to the element size and behave as a complex mechanical system (Bagi, 2012). The granular media, containing separated particles rolling and sliding each other, exhibits unique properties and, according to specific interpretations, does not form a single phase of matter but has properties like solids and liquids. For instance, the aggregation of limestone pieces can withstand the applied load of railways, i.e., behaves as solid materials; however, the sand particles in an hourglass flow like a fluid, or the granulate is filled from silos into bags in a similar way. Nevertheless, in certain conditions, the particles flowing through an orifice may form a bridge above the aperture, also demonstrating solid properties.

There are two options to describe granular conglomerates' behavior. One method applies the tools of the classical continuum mechanics, e.g., the strength of materials. The continuum

model assumes the granular media is filling the given volume continuously, and therefore, the mechanical characteristics can be described with continuous functions utilizing the measured properties of materials (Poisson's ratio, Young's modulus, yield strength, etc.). Furthermore, the state of the conglomeration is also described with continuous functions, while the state variables change according to the system of partial differential equations (Csizmadia & Nándori, 2002; Moharos et al., 2011; Égert & Keppler, 2007) presented in **Eq. 29** (balance equation of elasticity), **Eq. 30** (equation of geometry), **Eq. 31** (relation between stress and strain tensor), **Eq. 32** (kinematic boundary condition), and **Eq. 33** (dynamic boundary condition).

$$\mathbf{F} \cdot \nabla + \mathbf{f} = 0 \quad (29)$$

$$\frac{1}{2}(\mathbf{u} \cdot \nabla + \nabla \cdot \mathbf{u}) = \mathbf{A}_s \quad (30)$$

$$\mathbf{C}\mathbf{A} = \mathbf{F} \quad (31)$$

$$\mathbf{u}|_{A_u} = \mathbf{u}_0 \quad (32)$$

$$\mathbf{F} \cdot \mathbf{n}|_{A_p} = p_0 \quad (33)$$

In the equations, \mathbf{F} represents the stress tensor [Pa], \mathbf{f} is the volumetric load vector [N], \mathbf{u} demonstrates the displacement tensor [m], \mathbf{A}_s is the strain tensor [-], \mathbf{C} is the constitutive matrix of elastic properties [Pa], $\mathbf{u}|_{A_u}$ is the displacement on the surface A_u [m], and $\mathbf{F} \cdot \mathbf{n}|_{A_p}$ is the load on the surface A_p [N]. The system of differential equations above gives a solution (existence) that is exclusive (uniqueness) and proved. However, the exact solution for most engineering problems does not exist. The main issue of the continuum model application is the separation and aggregation of the elements. Therefore, numerical approximation methods should be applied instead.

The other method, DEM (Discrete Element Method), was developed for those complex engineering tasks in the 1970s and spread subsequently with the improvement of computers in the late 1990s (Bagi, 2012). Researchers and practicing engineers have successfully applied DEM in numerous areas of engineering areas such as the pharmaceutical industry (Ketterhagen et al., 2007), agriculture (Oldal et al., 2012), food industry (Yuan et al., 2011), storing grain crops (Gonzalez-Montanello et al., 2011), and even the nuclear industry (Keppler, 2013).

DEM describes the interactions between particles by solving the equations of motions for the particles numerically and determines the characteristic displacements of particle

systems. The peculiarity of the process is that it solves the governing equations of motion for each particle through a series of but finite time intervals. A discrete element model constitutes the state change processes as a series of small-displacement, while the actual displacement equals the sum of these displacement increments. The interaction forces resulting from the collisions of the particles are evaluated by a contact model (Cundall & Strack, 1979).

4.2.1. Equations of motion

The approximation method is based on the repeated solution of Newton’s second law of motion and the general rotational equation according to all single elements implemented in the model (shown in **Fig. 28** where t_i is the i^{th} time step, Δt is the time increment between the timesteps, and T is the threshold limit of timestep which still gives reasonable outcome of the solution). As an initial condition, the position and geometry of particles, the elastic properties of elements and relations, and the static state of elements and relations, i.e., external loads like gravity, must be known. Furthermore, the solution must detect particle-particle and particle–wall collisions during the solution. The main steps of a discrete element model are generating particles, determining the relations between the elements, computing forces and torques indicated between particles, solving the equation of motion, calculating the elements’ new position, and determining the new interactions, i.e., forces (Raji & Favier, 2004). Model failures may occur due to the element geometry, the selected element properties (rigid or deformable), or the micromechanical parameters which determine the interactions between particles.

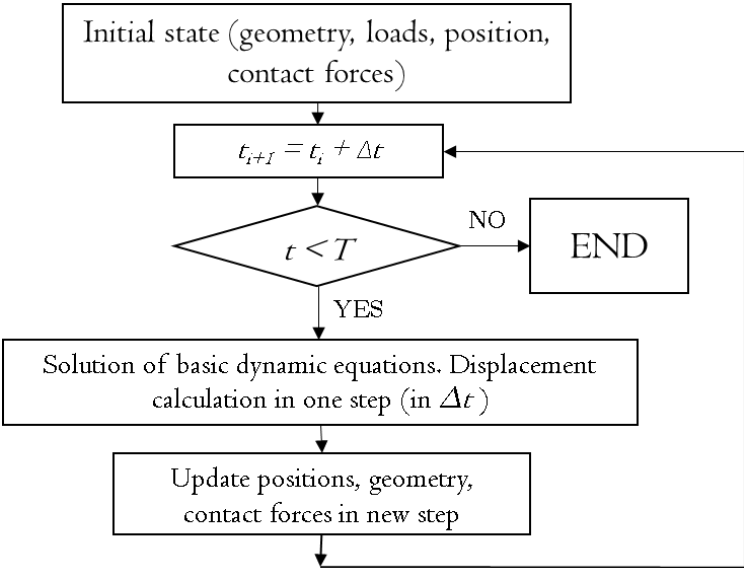


Fig. 28 Simulation cycle of the Discrete Element Method (Park & Kang, 2009)

The contact model allows the interaction force system for every collision to be calculated, and, based on initial displacements of single elements, new positions can also be evaluated. Subsequently, it is necessary to upgrade the kinematic parameters of the whole system, and the simulation cycle has to be repeated. Thus, by the continuous solution of fundamental laws of dynamics, the granular assembly's displacement, velocity, and acceleration field can be determined (Cundall & Strack, 1979). The displacement vector of element p^{th} - $\mathbf{u}^p(t)$ - is calculated from the components of shifts (\mathbf{u}) and rotation ($\boldsymbol{\varphi}$) of and around reference points (Bagi, 2012):

$$\mathbf{u}^p(t) = \begin{bmatrix} u_x^p(t) \\ u_y^p(t) \\ u_z^p(t) \\ \varphi_x^p(t) \\ \varphi_y^p(t) \\ \varphi_z^p(t) \end{bmatrix} \quad (34)$$

The displacement vector of the system, $\mathbf{u}(t)$, is gained by setting up the displacement and rotation vectors for each element (Bagi, 2012):

$$\mathbf{u}(t) = \begin{bmatrix} \mathbf{u}^1(t) \\ \mathbf{u}^2(t) \\ \vdots \\ \mathbf{u}^N(t) \end{bmatrix} \quad (35)$$

System displacement is approximated by the series of small displacements, assuming they are small enough within an iteration step. The velocity and acceleration vectors of element p^{th} and the system are defined according to Newton's second law of motion in **Eq. 38**, **Eq. 39**; and **Eq. 38**, **Eq. 39**, respectively (Bagi, 2012).

$$\mathbf{v}^p(t) = \begin{bmatrix} v_x^p(t) \\ v_y^p(t) \\ v_z^p(t) \\ \omega_x^p(t) \\ \omega_y^p(t) \\ \omega_z^p(t) \end{bmatrix} \quad (36)$$

$$a^p(t) = \begin{bmatrix} a_x^p(t) \\ a_y^p(t) \\ a_z^p(t) \\ \varepsilon_x^p(t) \\ \varepsilon_y^p(t) \\ \varepsilon_z^p(t) \end{bmatrix} \quad (37)$$

$$v(t) = \frac{du(t)}{dt} \quad (38)$$

$$a(t) = \frac{d^2u(t)}{dt^2} \quad (39)$$

Where $v(t)$ is the velocity vector [m/s], $\omega(t)$ is the angular velocity - rotation speed - vector [1/s], $a(t)$ is the acceleration vector [m/s²], $\varepsilon(t)$ is the angular acceleration vector [1/s²], and $u(t)$ is the displacement vector [m].

The displacement equation of a rigid element with general geometry can be gained by developing kinematics impulse and angular momentum theorems for each element, meaning six scalar equations per particle. For instance, in the impulse-momentum theorem, force (F_t and F_n are the tangential and normal force, respectively) and torque (M_g) - shown in **Fig. 29**, can be determined by reducing the system of forces acting on the elements into the reference points of particles.

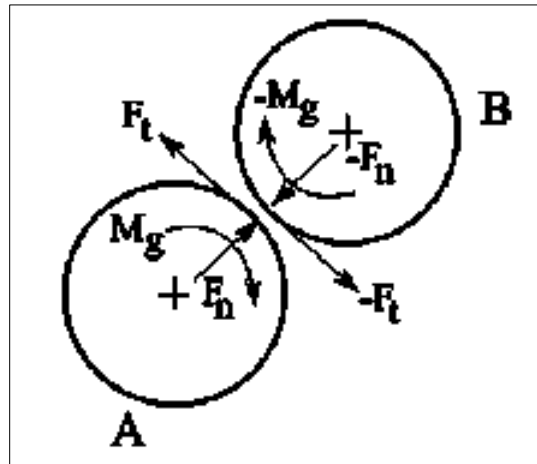


Fig. 29 Force and torque indicated by the collision of two elements (Varga, 2018)

The equation of motion for element p^{th} can be derived based on the explanation above (Bagi, 2012):

$$M_p(t)a_p(t) = f_p(t, u(t), v(t)), \quad (40)$$

where the matrix \mathbf{M}_p represents the mass and inertia - [kgm²] - of element p and depends on time because the rotation of element p impacts the inertia except for the element with spherical symmetry, while vector \mathbf{f}_p depends on the displacement and velocity of element p and others which may interact with p .

As in the case of the displacement vector, the equation of motion for the system - **Eq. 41** - can be achieved by developing all particles' equations of motion (Bagi, 2012).

$$\mathbf{M}(t)\mathbf{a}(t) = \mathbf{f}(t, \mathbf{u}(t), \mathbf{v}(t)), \quad (41)$$

where $\mathbf{M}(t)$ is the block diagonal matrix – also called inertia matrix [kgm²] - formed from the $\mathbf{M}_p(t)$ blocks.

4.2.2. Collisions and contact model

Generally, collisions are estimated by a spring-dashpot system. There are at least five different micromechanical parameters for each material in the simplest scenario and other model parameters, e.g., element shape, or simulation time step. Determining the micromechanical parameters of granular media makes numerical modeling very complicated and time-consuming. In most cases, it takes more research and time to calibrate the parameters than to develop and solve a discrete element model (Bagi, 2012). The main reason for the problem is that modeling results depend primarily on the mechanical constants of the interactions between the discrete elements, i.e., on the micromechanical parameters characteristic of the given assembly.

Due to the numerical approximation, in many cases, the experimentally determined value of some micromechanical parameters gained from direct measurements does not lead to the most real consequences. Still, the behavior of the whole assembly can be described with sufficient accuracy, even with several combinations of parameters. It might be happening that there are multiple combinations of micromechanical parameters that result in the same macro behavior of the granular assembly - which might be called the problem of ambiguity -; hence the calibration procedure must be very rigorous to get proper parameters. Properties of individual particles may be determined by comparing measured and numerical macro behavior of a particular physical process, i.e., by a calibration procedure presented in **chapter 4.2.4** (Keppler et al., 2016).

4.2.3. YADE

Freeware software YADE (Šmilauer & Chareyre, 2010) was used for the numerical calculations of proppant placement. YADE uses perfectly rigid, so-called BALL type elements - **Fig. 30** shows the series of two springs representing normal stiffness of contact between two spheres -and generally normal k_N [N/m] and shear stiffness k_S [Pa] to describe interactions.

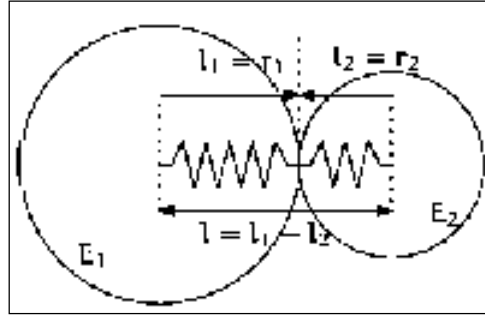


Fig. 30 BALL type model in YADE (Varga, 2018)

If the colliding elements have Young's modulus E_1 and E_2 [MPa], radiuses r_1 and r_2 [mm], respectively, the normal stiffness of colliding particles is

$$k_N = \frac{2E_1 r_1 E_2 r_2}{E_1 r_1 + E_2 r_2} \quad (42)$$

The value of shear stiffness can be calculated by a predefined ratio of normal stiffness value (Oldal et al., 2012). The displacement coordinates of individual elements - normal u_N and shear displacement u_S - are calculated by geometrical parameters of interactions. The normal displacement u_N is

$$u_N = |C_2^\circ - C_1^\circ| = |C_2 - C_1|, \quad (43)$$

where C_1 and C_2 [-] denote reference centers of colliding elements when the interaction is established, while C_1° and C_2° correspond to centers of interacting particles as these can move during the simulation. Shear displacement u_s [mm] is calculated by adding the motion of the contact point in global space and the joint movement of colliding elements (Šmilauer & Chareyre, 2010).

Normal and shear components of interaction forces are calculated by the contact model considering both of the displacements:

$$F_N = k_N u_N \quad (44)$$

$$F_S = \begin{cases} F_N \tan\phi & \text{if } |k_S u_S| > F_N \tan\phi, \\ k_S u_S & \end{cases} \quad (45)$$

where ϕ denotes friction angle [°] between colliding elements (Šmilauer & Chareyre, 2010).

Ensuring numerical stability of discrete element simulations, there is a threshold limit (Keppler, 2013) of the simulation time step Δt_{crit} in YADE:

$$\Delta t_{crit} = \frac{2}{\omega_{max}} = \min_i \sqrt{2} \sqrt{\frac{m_i}{K_i}} \quad (46)$$

where ω_{max} [s⁻¹] corresponds to the highest eigenfrequency within the model, m_i [kg] denotes the mass of the i^{th} particle, and K_i [N/mm] is the stiffness of the i^{th} spring. The unbalanced force is used for characterizing the numerical stability of models in YADE. This artificial force is calculated by the ratio of summarized forces on all bodies and mean forces acting on interactions. If the system is in perfectly static equilibrium, the summarized force on all bodies tends to be zero. Thus, the unbalanced force will converge to zero in a quasi-static state (Šmilauer & Chareyre, 2010). **Fig. 31** presents the Δt equals $1.4 \cdot 10^{-7}$ determined by the YADE solver based on the input model.



Fig. 31 YADE solver with Δt (edited by the Author)

4.2.4. Calibration Procedure

In the Author's prior work (Varga et al., 2020), proppant particles' shape and micromechanical parameters were determined by calibration, where the silo outflow experiment was designated as a parameter identification technique.

The experimental investigation of the outflow of a cylindrical silo was performed with a model silo equipped with a data measuring and processing system. The model silo body - shown in **Fig. 32** - consists of a 110 [mm] diameter and 700 [mm] long PVC cylinder with a removable conical hopper, including a 35 [mm] diameter outlet. The cone half-angle of the bin was 60°. The total mass of the granular media, i.e., the proppant particles, was 1.7 [kg].

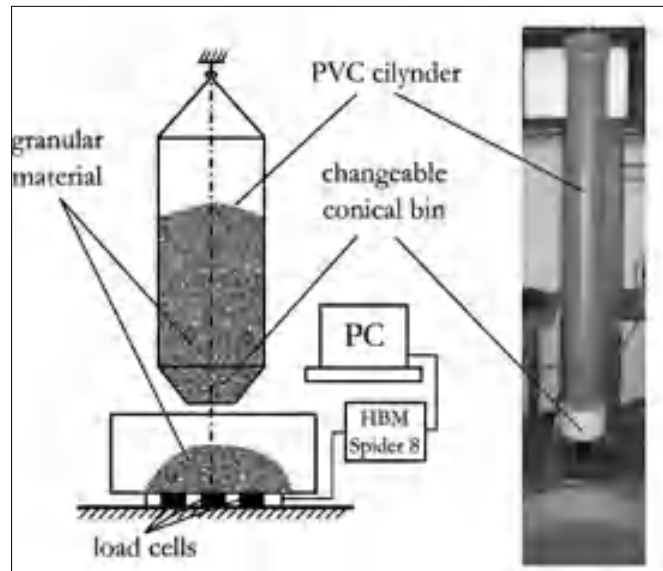


Fig. 32 Gravitational silo discharge experiment (Oldal & Safranyik, 2015)

During the experimental investigations, the discharged mass was measured by three HBM (Hottinger Baldwin Messtechnik) C9B force transducers. In addition, an HBM Spider8 measuring amplifier was installed for data acquisition with a 50 [Hz] sampling rate. The gained mass-time data were plotted in a standard coordinate system for the data processing period, and the average mass flow discharged was determined. Due to the linear nature of the phenomenon, the usage of linear regression was a straightforward solution to directly determine the average mass flow rate, i.e., the slope of the linear mass-time function in **Fig. 33**. The measurement was repeated five times, and the average discharge rate was obtained at 0.47 ± 0.002 [kgmin⁻¹].

The steps of the simulation process were the same described in **chapter 4.2.1**. First, the software YADE randomly created particles inside the silo. Subsequently, the particles fell by

gravity. Before the silo would have been opened, the granular assembly had to get the quasi-static state because the contact model presented in **chapter 4.2.3** describes the interaction of particles with springs and damping systems, i.e., the steady-state condition must be reached when vibrations become damped. Afterward, the outlet of the silo was opened, and the particles flowed out of the silo (**Fig. 33**).

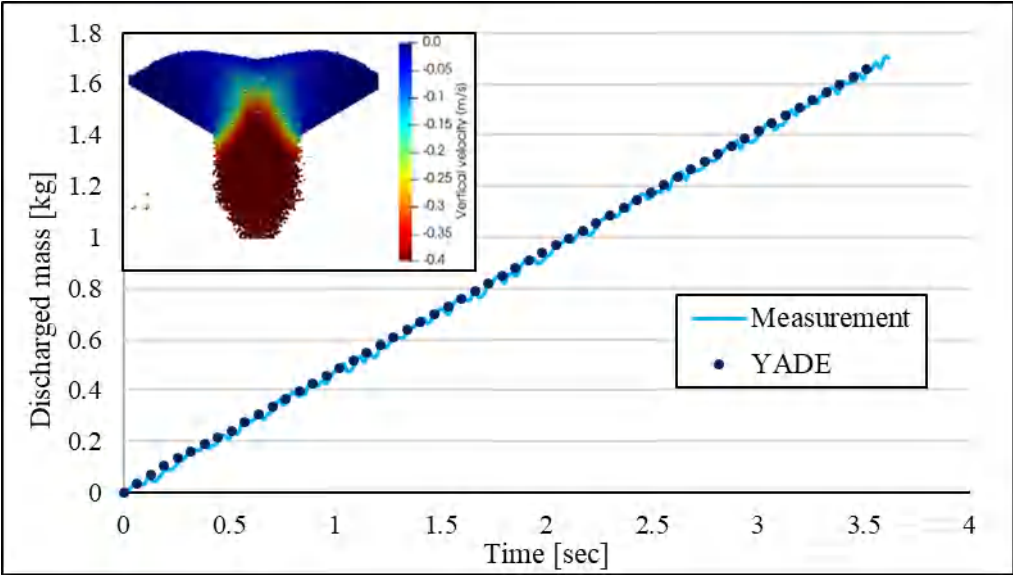


Fig. 33 Measured and calculated mass–time functions (Varga et al., 2020)

Using the parameters in **Table 1**, the computed and measured discharge rates showed sufficient fitting in **Fig. 33**, where falling particles also can be seen colored by vertical velocity. This result implies that the calibrated set of micro parameters can be utilized for modeling proppant particles displacement within fractures.

Table 1. Calibrated micromechanical parameters (Varga et al., 2020)

Parameter	Proppant	Silo
Poisson-ratio, ν [-]	0.25	0.3
Young modulus, E [Pa]	$4.13 \cdot 10^{10}$	-
Density, ρ_e [kg/m ³]	2800	5100
Friction angle, φ [°]	10	1
Coeff. of rolling friction, f [m]	0.0001	0

4.3. Finite Element Modeling

4.3.1. Mechanical analysis

To determine the proppant pack's deformation, finite element analysis was applied. The concept of this method was developed in the mid-1950s by Turner et al. (1956) and has become an indispensable tool in engineering practice in recent decades.

Finite element modeling enables one to create a mathematical model that includes geometry, material models of the individual elements, boundary conditions, and contacts between the elements. The essence of the method is decomposing the investigated geometry into finite but tiny elements connected by nodes – meshing - i.e., the problem is discretized, which allows numerical approximation of analytically non-solvable partial differential equations. At these nodes, the solution of the system of equations is searched that describes the relationship between input and output quantities. For instance, in stress analysis, the input quantity is the force from some load, and the output quantity is the displacement. Stiffness creates a connection between these quantities. During the preprocessing, one creates geometry, performs possible simplifications on the given geometry, and defines the material models of each part and the necessary contacts. The next step is to make the numerical mesh and then precisely specify the loads and boundary conditions that describe reality. In the physical aspect, the boundary conditions represent a natural part of the model, e.g., loads and constraints in mechanics or flowrate inlet-outlet in fluid dynamics. However, boundary conditions and the initial data conclude a particular solution among the infinitely many alternatives from the mathematical point of view.

During the solution, the load vector (F) and the stiffness matrix (K) are produced, and the displacement (U) of the nodes is found by solving the prescribed system of equations:

$$K \times U = F \rightarrow U \quad (47)$$

Based on the force-displacement diagram of the given task, linear and nonlinear problems are distinguished. If the model contains contacts, a nonlinear problem is examined. In this case, **Eq. 47** is modified to the following expression:

$$K(U) \times U = F \rightarrow U \quad (48)$$

This way, the secondary quantities, deformations, and stresses can be determined (Varga et al., 2020).

The accuracy of any Finite Element Method is directly correlated to the finite element mesh applied. The finite element mesh is used to discretize the model and segment it into more minor elements connected by nodes in which the set of equations is solved. These equations approximate the governing equation of interest by constructing and solving the set of polynomial functions. Being the mesh refined, the calculated result approaches the real solution; however, it also affects the computational time and cost. Hence, it is a crucial point to find the mesh density, which gives a rational solution but enables the solver to remain in a reasonable calculation timeframe.

During the Author's research, one of the most popular FEM software, the ANSYS Static Structural module, was utilized to simulate proppant deformation and embedment.

4.3.2. Computational Fluid Dynamics

After the fracture was filled and the deformation of proppant particles and formation was examined, fluid flow through the deformed propped fracture was investigated using computational fluid dynamics (CFD) software. In physics and engineering, fluid dynamics describes the flow of fluids, i.e., liquids and gases. According to John (1995), three approaches exist in the history of fluid dynamics. The first approach is experimental fluid dynamics, laid in the 18th century in England and France. There was a gradual development of theoretical fluid dynamics in the 18th and 19th centuries, primarily in Europe. In the 1990s, the appearance of high-speed computers and the development of accurate numerical algorithms revolutionized fluid dynamics. The third approach has been introduced as computational fluid dynamics. The CFD solvers are based on the fundamental governing equations of fluid dynamics. They use the continuity, momentum, and energy equations to describe fluid dynamics.

The essence of the continuity equations is that mass is neither created nor destroyed in the control volume. The control volume is a closed volume within the finite region of the flow. The integral form of the continuity equations can be written as:

$$\frac{\partial}{\partial t} \iiint_V \rho dV = - \iint_S \rho u \cdot dS, \quad (49)$$

where ρ is the fluid density [kg/m³], \mathbf{u} is the flow velocity [m/s] and t is time [s]. On the left side rate of change of mass can be found, while the term on the right side means the net inflow of mass.

The momentum equations are based on Newton's second law of motion. The point is the equilibrium of the fluid's rate of change of momentum to the external forces acting on the fluid within the control volume, i.e., the Navier-Stokes equation developed by Navier, Poisson, Saint-Venant, and Stokes between 1827 and 1845 (Darrigol, 2002). The integral form of momentum equations:

$$\frac{\partial}{\partial t} \iiint_V \rho \mathbf{u} dV = - \oint_S (\rho \mathbf{u} \cdot d\mathbf{S}) \mathbf{u} - \oint_S p d\mathbf{S} + \iiint_V \rho \mathbf{f}_{body} dV + F_{surf} \quad (50)$$

The term on the left side of the equation is the momentum change within the control volume, while on the right side, the terms represent the net inflow of momentum, total pressure, total viscous force, and total body force (John, 1995).

The third type of equation is the energy equation, which states that the energy can convert from one form to another, and the total energy in a closed system remains constant. For example, the energy equation can be written in the following form (Bathe and Saunders, 1984):

$$\rho \frac{De}{Dt} = -\nabla \cdot \mathbf{q} - \rho(\nabla \cdot \mathbf{V}) + \dot{Q} \quad (51)$$

where ρ is the density [kgm⁻³], e is the internal energy [J], \mathbf{q} is the vector field of the heat flux by thermal conduction [kgs⁻³], \mathbf{V} is the velocity vector [ms⁻¹], and \dot{Q} [J/s] is the rate of internal heat generation by the effects such as viscous friction or radiation).

For numerical calculations in case of fluid flow through the proppant particles, ANSYS CFX software was utilized.

4.4. The One-Way Coupling Method

The Author developed the so-called one-way coupling method to describe a propped fracture's complex mechanical behavior and describe the phenomenon with an advanced process. This method contains the results of DEM, FEM (structural analysis), and CFD. First, the particles generated and placed in the fracture by DEM (YADE) software were converted into FEM static structural module, where proppant deformation and embedment - due to the closure pressure - were determined. Subsequently, the deformed assembly was converted into a CFD environment where pressure drop due to the "resistance" of the propped fracture to the

fluid flow could be calculated. The flow chart of the developed method can be seen in **Fig. 34** and it is detailed in the following chapters.

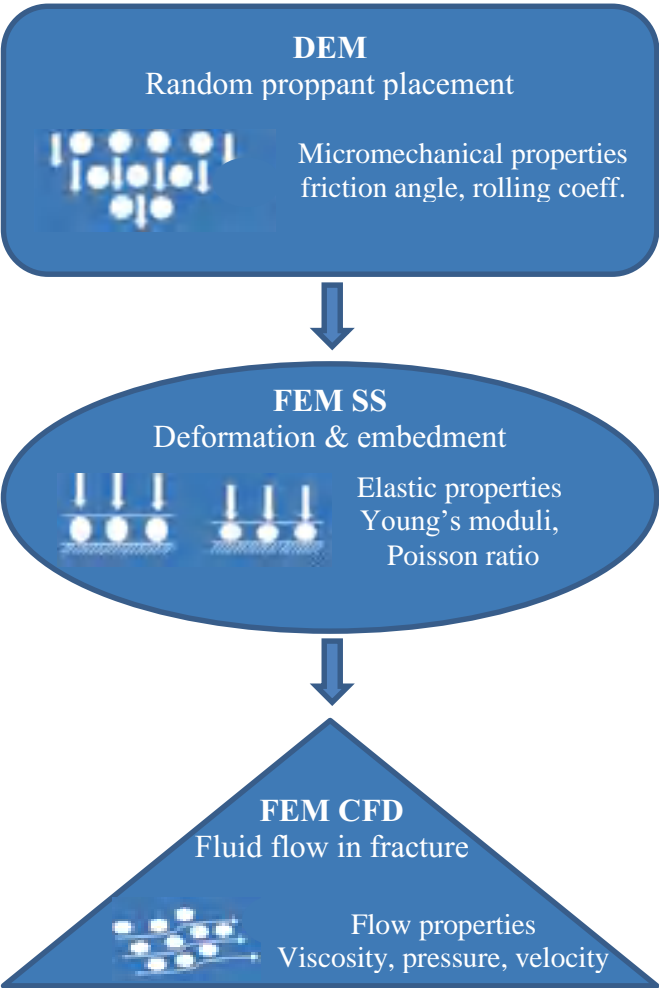


Fig. 34 Process flow developed (edited by the Author)

4.5. Numerical Fracture Model

As introduced above, DEM simulation generated fracture that is filled by proppant particles. The first step is generating the particles in the model space casually. Although a regular layout is easy to create, this particle generation procedure can distort the behavior of the particle assembly (Šmilauer & Chareyre, 2010). Due to this reason, YADE software applies a random particle generation technique. At the beginning of the simulation, proppant particles were accidentally generated in a closed virtual box placed above the fracture. The box was closed until the summarized kinetic energy of elements approximated zero (the system reached a quasi-static state). Then the bottom of the box was opened, and the particles could fall into

the fracture by gravity. This random particle placement procedure allows the representation of proppant transport and placement by the fracturing fluid, neglecting particle settlement by gravity. The filled fracture can be seen in **Fig. 35** . The YADE source code with an example of a proppant size distribution setup is presented in **Appendix 10.5**.



Fig. 35 Fracture filled by proppant (edited by the Author)

The resulting geometry was pushed by an artificial assembly from the top of the fracture with 500 [psi] to enable proppant pavement, compaction, and slippage, which occur during actual fracturing and is also considered in API standard proppant conductivity measurements by applying an initial stress (Renkes et al., 2017), and then converted into FE software environment.

Table 2. The number of nodes and elements (edited by the Author)

Proppant diameter [mm]	Nodes	Elements
0.720	2 879 043	1 587 117
1.004	2 005 523	1 013 071
1.417	1 473 046	743 518

The first step in the FEA analysis was to specify the material properties. As described in **chapter 4.1.2**, the proppant Young’s modulus and Poisson ratios were 41,306 [MPa] and 0.22. The Young’s modulus of the formation was systematically varied in a range of 1,000 to 30,000 [Mpa]. The Poisson ratio was 0.22 in each case. The second step was to create a

numerical mesh; then, the parts were meshed using second-order tetrahedron elements. Finally, mesh refinements were applied to the stress concentration areas, such as the particles and surfaces of the fracture. The mesh of the assembly can be seen in **Fig. 36** , while **Table 2** summarizes the nodes and elements in each case.

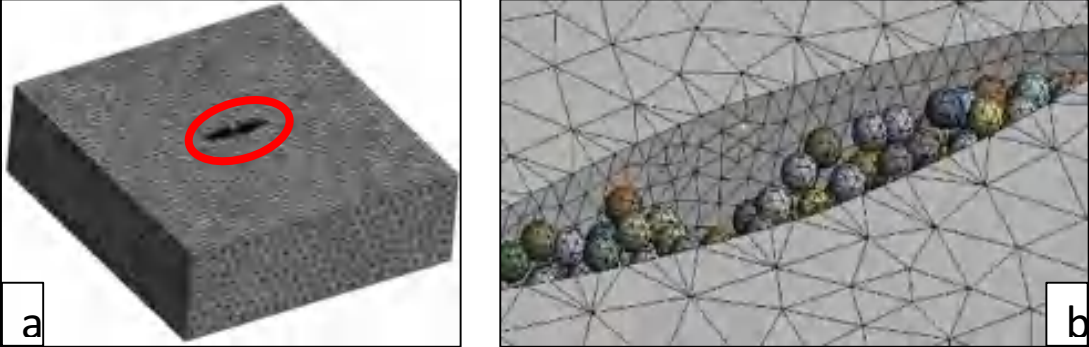


Fig. 36 Numerical mesh of the formation (a) and proppant particles (b) (edited by the Author)

One constraint was applied during the simulations to model fracture behavior: fixed support was used at the bottom of the formation presented in **Fig. 37 b**. In contrast, negative pressure was applied on the inside surfaces of the fracture to demonstrate the closure pressure acting as the initiator of deformation and embedment shown in **Fig. 37 a**.

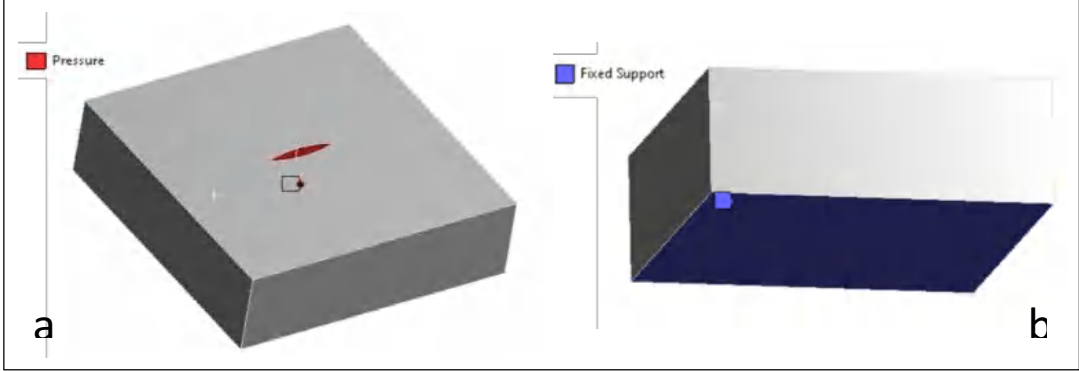


Fig. 37 Surface pressure (a) and fixed support (b) (edited by the Author)

Contact behavior was applied and modeled on connecting surfaces. The model had only bonded contacts, entailing no sliding or separation between faces or edges. In addition, automatic contact detection was utilized in the FEA software. The default contact formulation was adjusted Multi-Point Constraint (MPC) to bonded contacts. In **Fig. 38** , an undeformed and deformed assembly can be seen colored by the extent of total deformation. The deformed body is represented at two times magnification to get the results perceived. Comparing and analyzing

the assemblies, one can obtain that the contacts duly worked according to the rock and proppants' visible displacement and deformation.

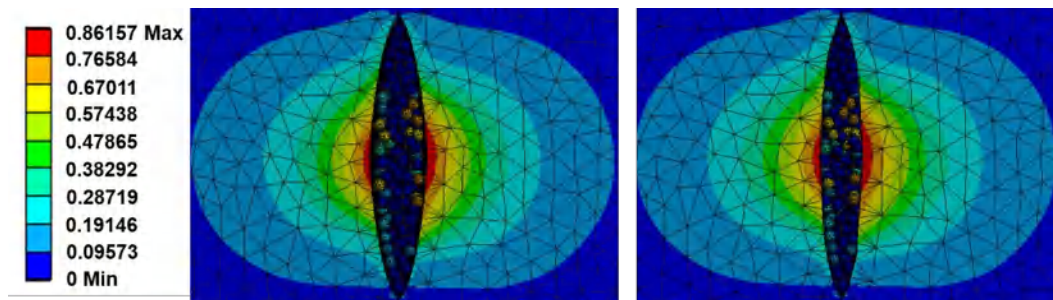


Fig. 38 Undeformed and deformed assembly (2x deformation)
(edited by the Author)

After FEM simulated deformation, the deformed geometry in the static structural analysis was exported into the ANSYS CFD environment. The model build-up steps in CFD are similar to the structural analysis, i.e., geometry definition – deformed assembly imported – meshing, model setup, solution, and results.

Meshing is crucial in every finite element analysis; however, it represents another aspect in computational fluid dynamics runs. For example, the static structural analysis involves body meshing to compute deformation and displacement according to the applied external loads and boundary conditions. On the contrary, CFD requires pore space meshing to determine fluid dynamics between the deformed assembly, i.e., meshing the space between proppant particles and the fracture wall which forms the porous media. Therefore, the pore space was meshed using second-order tetrahedron elements with an element size of 0.4 [mm] ($\sim 1.37 \cdot 10^{-7}$ element), which satisfied the mesh independence criteria, i.e., the smaller element size did not result in a different outcome (shown in Appendix 10.2). In addition, mesh refinement was applied to the areas between the particles to make the model fine-meshed instead of course.

In model setup, general settings, e.g., transient or steady-state type analysis, relative or absolute velocity, etc.; materials; boundary and cell zone conditions; reporting option; solution control and method; monitors; graphics; and plots can be defined. The number of iterations is a relevant aspect that can be defined experimentally by checking the stability of residuals and a predefined output parameter in parallel, e.g., area-weighted velocity, pressure, or pressure drop. In **Fig. 39**, the residual plot is presented, indicating an essential monitor to control the simulation convergence criteria, where the minimum level is 10^{-4} in CFD software. Although monitoring the residuals is necessary but not a sufficient condition. A user-defined parameter,

e.g., pressure drop, should be monitored in parallel to check the numerical stability, shown in Fig. 40 .

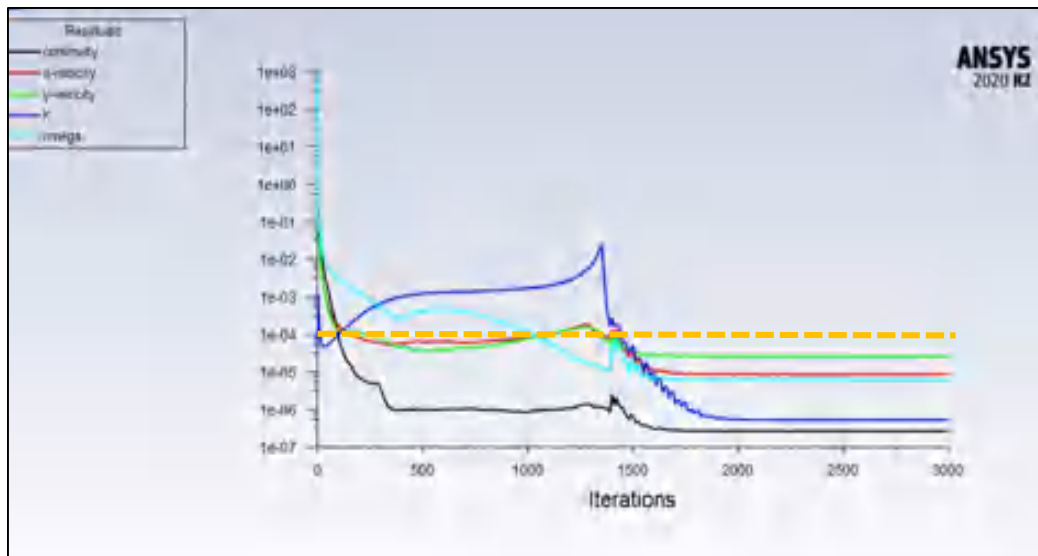


Fig. 39 Residuals of CFD analysis (edited by the Author)

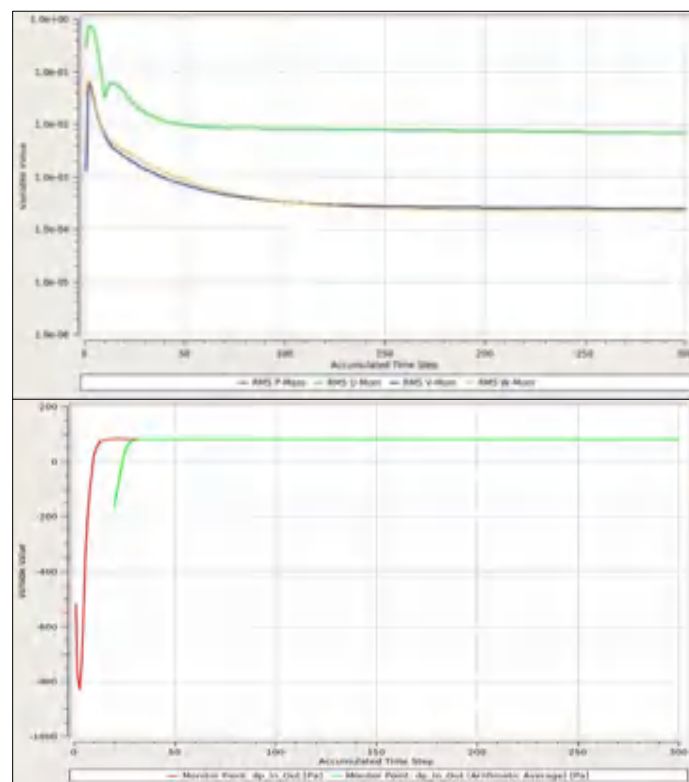


Fig. 40 Parallel monitors for numerical stability (edited by the Author)

Afterward, the simulation is solved, and the results are available, i.e., the fluid dynamics are determined, and the flow velocity and pressure distribution can be monitored. **Fig. 41** shows the streamlines representing the fluid flow velocity in the cross-section between the particles.

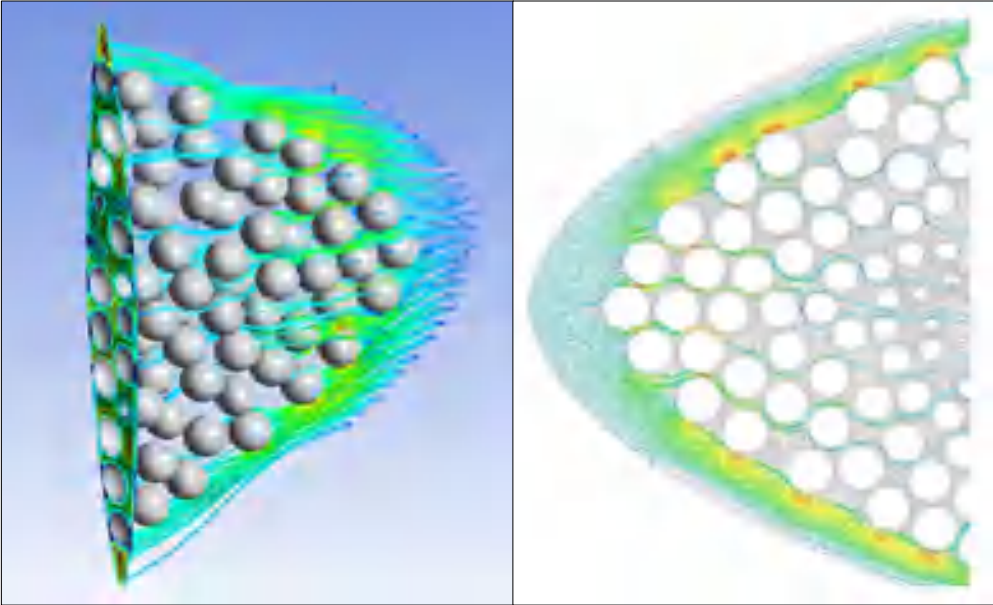


Fig. 41 Flow velocity by streamlines (edited by the Author)

During the CFD analysis, the pressure drop was determined. To investigate real well flowrates at which turbulence may take place, one of the most commonly used turbulence models, the k-omega turbulence model, was applied to describe the fluid flow.

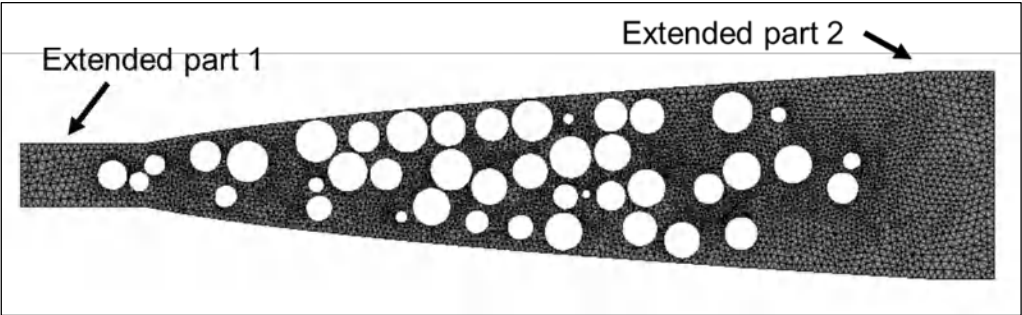


Fig. 42 Numerical mesh of CFD analysis (edited by the Author)

The fracture's bottom and top were extended to define the boundary conditions well. The pore pressure was defined as hydrostatic before in **chapter 4.1.2**; however, during the set of simulations, it was considered to be constant to allow comparisons, i.e., pore pressure impact was excluded from the analysis to get focused on more relevant factors like closure pressure, proppant geometry, rock Young modulus. **Fig. 42** shows the numerical mesh of the CFD model

in a 2D cross-section, while **Fig. 43** represents a typical case of velocity distribution within the fracture from the top view. The arithmetic mean of the cross-section was defined to calculate apparent permeability by the formula in **Eq. 52**:

$$A_{avg} = \frac{1}{n} \sum_{i=0}^n A_i, \tag{52}$$

where A_i are the cross-sections [mm²] defined along the fracture length, and A_{avg} is the arithmetic mean.

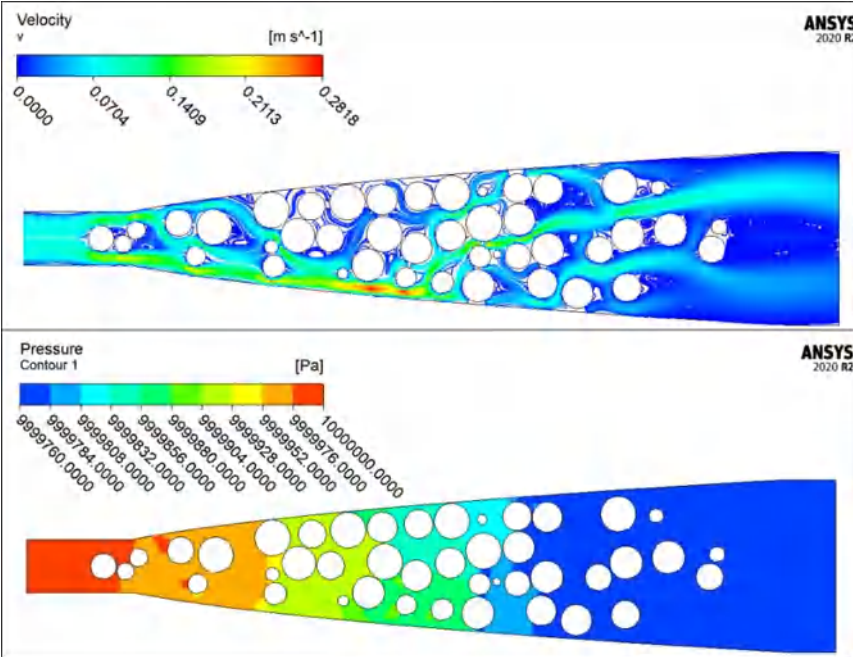


Fig. 43 Velocity and pressure distribution within the fracture (edited by the Author)

4.6. One-way coupled model results

As indicated in **chapter 3.5**, several factors were examined to gain relevant consequences regarding fracture behavior, i.e., fracture width reduction and fracture conductivity. First, DEM was utilized to investigate the effect of proppant geometry and particle size distribution, i.e., the size variance of the granular media representing the sieving process during proppant production which implies how well the particles are sorted. Subsequently, the closure pressure and the hydrocarbon-bearing reservoir’s Young’s modulus were inspected and incorporated with proppant size influence. In addition, the initial fracture geometry was studied and presented below.

4.6.1. Proppant geometry

Proppant samples – technical datasheets are attached in **Appendix 10.3** – gained from industrial players were examined with an electron microscope to understand their original shape. **Fig. 44** . demonstrates the pictures and the discrete element model solutions to approximate the difference from the perfect spherical assumption. The so-called clumps – the combination of two or more spheres – can be applied in DEM to define forms.

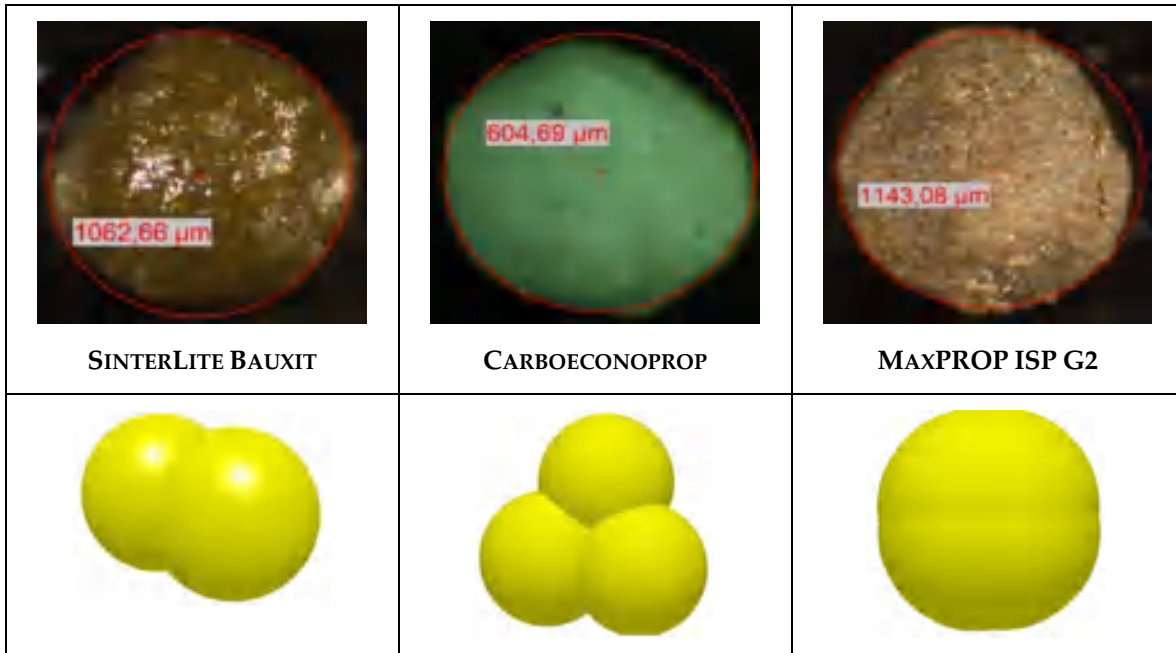


Fig. 44 Electron microscopic photos and DEM clumps (edited by the Author)

The clumps are multi-sphere particles defined to represent unusual geometry, shown in **Fig. 45** . The sphere radius was determined to develop the same volume of 2.01 [mm³] – the volume of a 1.6 [mm] radius sphere – of the particles to make the results comparable.

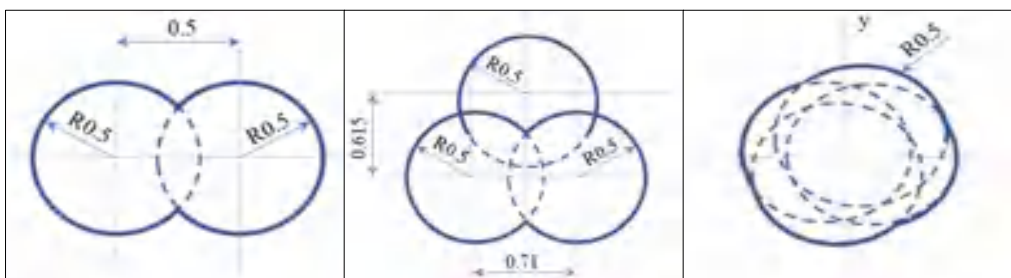


Fig. 45 Multi-sphere clumps (edited by the Author)

The clump of 4 spheres forms the most complicated geometry, which approximates the real proppant shape the greatest among the examined alternatives. The coordinate setup for that case is presented in **Fig. 46**.

Name	Position X (mm)	Position Y (mm)	Position Z (mm)	Physical Radius (mm)
1 sphere 0	0.096	0.026	0	0.5
2 sphere 1	-0.096	-0.026	0	0.5
3 sphere 2	-0.026	0.096	0	0.5
4 sphere 3	0.026	-0.096	0	0.5

Fig. 46 Sphere coordinates (edited by the Author)

Fig. 47 presents the duration of simulation runs for each type of clump. The more sphere forms the clump from the figures; the more time is needed to compute the simulation. This observation is concluded from the DEM operation presented in **chapter 4.2**. More spheres generate more interaction between the particles entailing a higher number of systems of equations calculating load and torque at collisions.

From the proppant technical data sheet, one can observe that the physical appearance of proppant geometry is characterized by sphericity and roundness. Sphericity is the ratio of the surface area of a sphere to the particle’s surface area. Consequently, the sphericity is 1 for a sphere and is less than 1 for any other geometry. Roundness describes the particle smoothness, i.e., the ratio of the average radius of curvature of the edges to the radius of curvature of the maximum inscribed sphere (Guo et al., 2017).

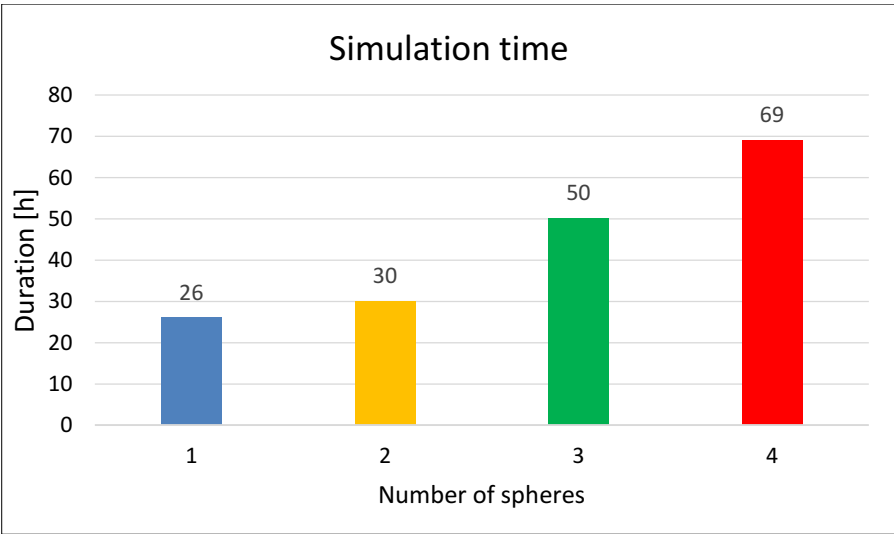


Fig. 47 Duration of DEM runs (edited by the Author)

Fig. 48 demonstrates the sphericity and roundness indices and shows that in case of ceramic proppants both the sphericity and roundness is rather high (~ 0.9).

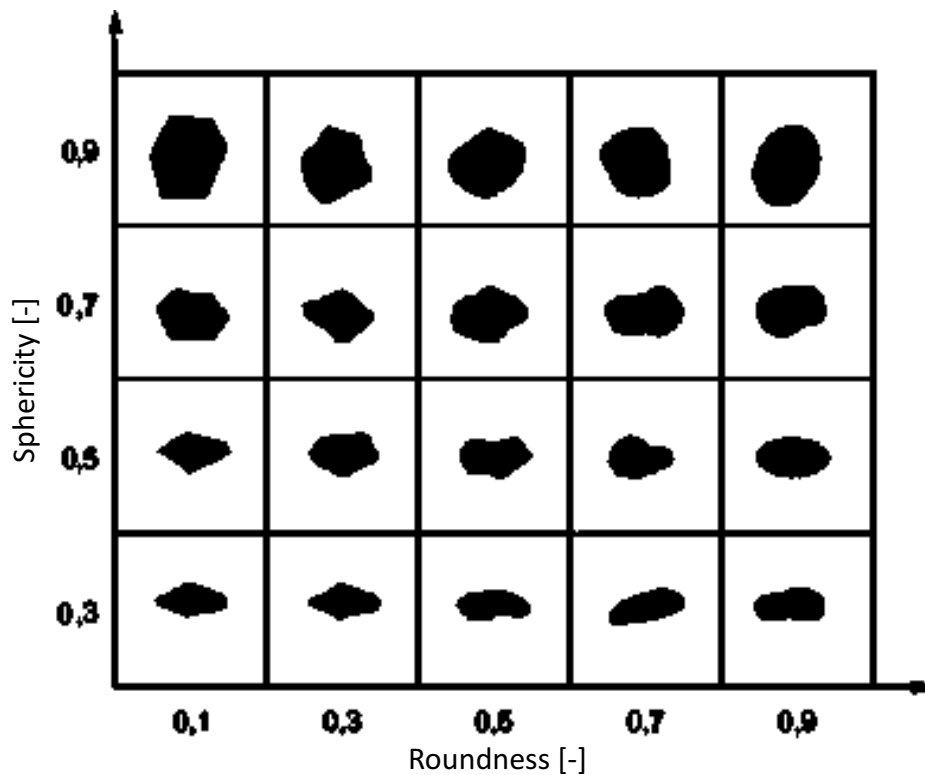


Fig. 48 Proppant roundness and sphericity (Liang et al., 2015)

The one-way coupled simulations resulted in exciting outcomes considering the porosity and permeability values for the geometries created to investigate the effect of forms differing from spheres. **Fig. 49** (red dashed lines show the value of single spheres) presents the results, demonstrating the irrelevance of clumps formed by two and three spheres. Applying two and three spheres to approximate the geometry of proppant particles resulted enormously high porosity and permeability, which values exceed the reasonable representation of propped fractures and made the Author conclude to exclude them from the investigation.

However, the clump results created from four spheres showed a much more rational interpretation. The porosity and permeability for that case align with the expectations gained by the measurements in **chapter 4.7.2.3** and the proppant data sheets in **Appendix 10.3** since they are slightly greater than in the case of spheres. Although the results of the clump formed by four spheres are sufficient, they do not show relevant differences compared to the outcomes of single spheres. In the meantime, they require computational resources with more magnitude

higher than the application of individual spheres. Therefore, the application of clumps was eliminated from further examination.

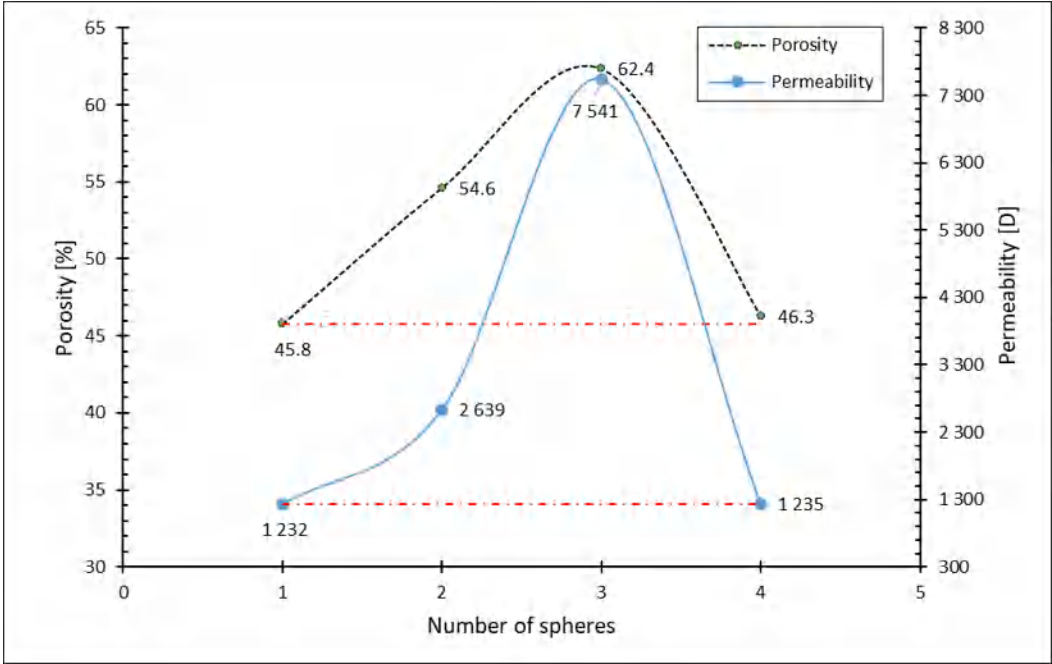


Fig. 49 Porosity and permeability for clumps (edited by the Author)

4.6.2. Proppant size, size distribution, and closure pressure

As presented in **chapter 3**, one of the most critical parameters affecting fracture permeability and conductivity is the proppant size. It significantly impacts the hydraulic fracturing treatment, and this is the factor that can be planned and optimized by engineering. The sensitivity analysis below adjusted the closure pressure to 25 [Mpa] and the formation Young’s modulus to 15 [Gpa], representing a medium-deep formation. **Fig. 50** summarizes the results of the simulations run, while **Fig. 51** makes a comparison between the analytical and numerical results.

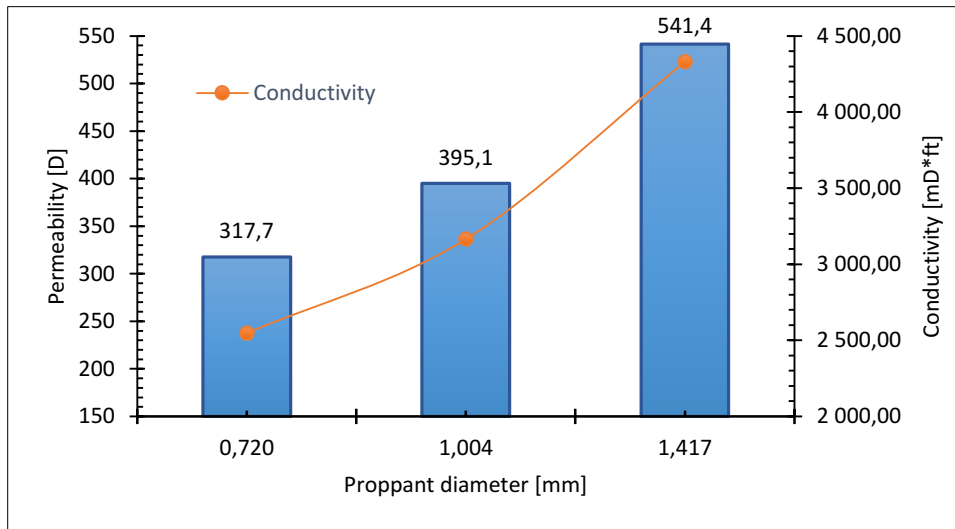


Fig. 50 Permeability and conductivity (edited by the Author)

As expected, both the permeability and conductivity increase significantly with the proppant diameter. From **Fig. 51**, one can conclude that the numerical, one-way coupling method resulted in higher conductivity values. The reason can be traced back to more factors. One is the non-uniform stress distribution within the proppant particles and the fracture wall. The random proppant placement enables the particles to support each other in every direction, while the analytical solution supposes uniaxial displacement. Another relevant difference comes from the fluid dynamics assumptions. The analytical model uses the Kozeny-Carman tube model and does not consider geometrical facilities that may expedite the fluid flow in special edges of the fracture, shown in **Fig. 41**.

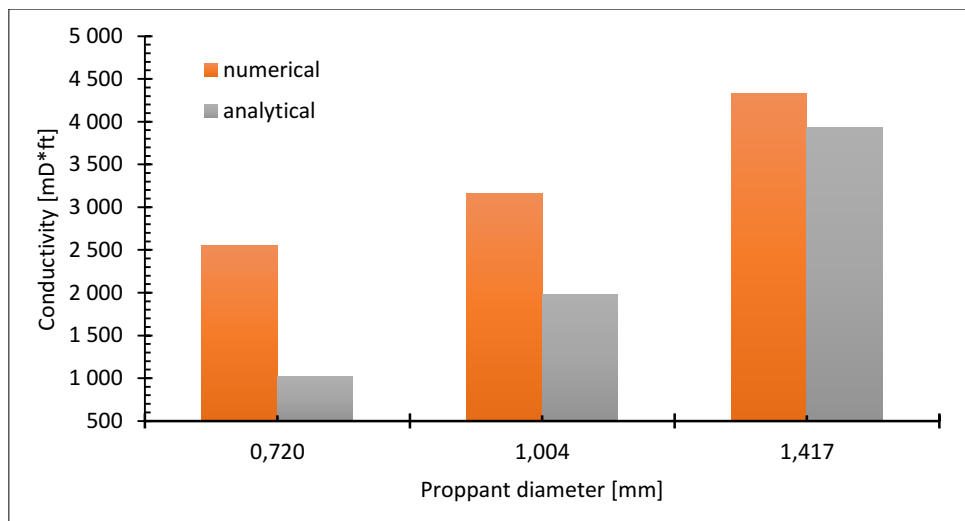


Fig. 51 Numerical and analytical conductivity (edited by the Author)

4.6.2.1. Proppant size distribution and closure pressure

One of the numerous benefits of DEM is applying size distribution, i.e., it is capable of generating different diameter particles within the given ranges for a certain granular media. The relevance of size distribution investigation stems from the fact that the smaller particle fragments can be placed within the pore throat of larger elements reducing the interconnected effective porosity of the proppant pack. Nevertheless, on the other hand, it can also support particles limiting deformation by carrying the distributed load.

Based on the TDS (Technical Data Sheet) in **Appendix 10.3**, the size distribution is given in **Table 3**. The size distribution is determined by sieve analysis; one more detailed distribution is presented in **Fig. 52**.

Table 3. Size distribution (edited by the Author)

20/40			16/30			12/18		
Mesh	Size [μ]	Weight [%]	Mesh	Size [μ]	Weight [%]	Mesh	Size [μ]	Weight [%]
16	1,190	0.01	12	1,680	0.04	12	1,680	4.00
20	841	8.07	16	1,190	0.93	16	1,190	91.00
25	707	38.55	18	1,000	55.86	18	1,000	5.00
30	595	46.90	20	841	31.42	20	841	0.00
35	500	5.60	25	707	10.64	25	707	0.00
40	400	0.71	30	595	1.07	30	595	0.00
50	297	0.14	40	400	0.07	40	400	0.00

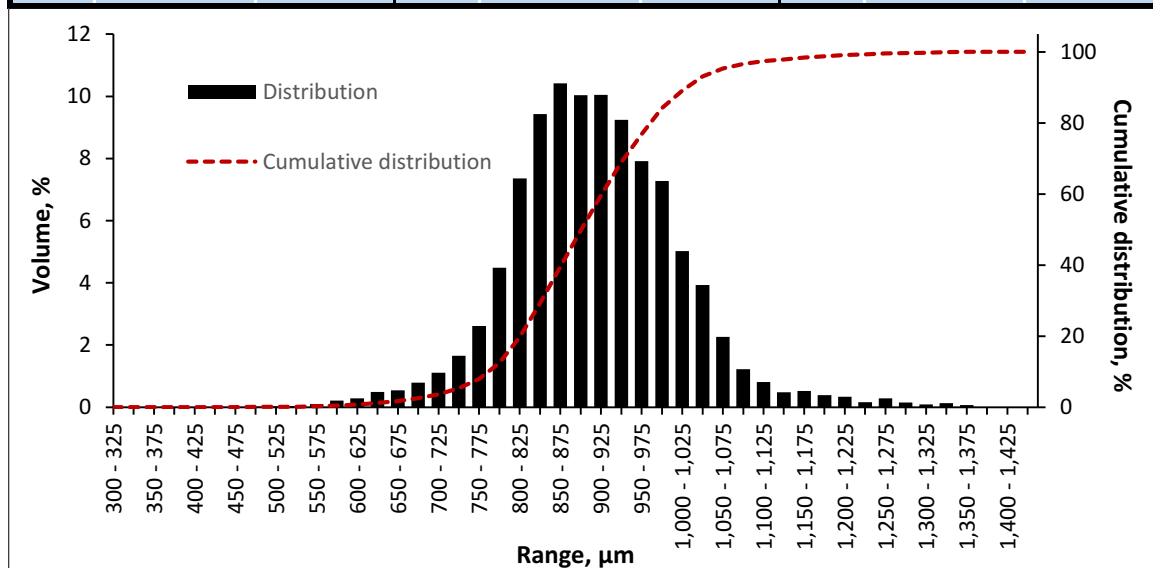


Fig. 52 Detailed size distribution of 16/30 proppant (edited by the Author)

The impact of size distribution and closure pressure is presented in the integrated sensitivity test in Fig. 53 , Fig. 54 , Fig. 55 , and Fig. 56 . The test was implemented for six DEM model setups regarding the granular media. The particles were generated according to the size distribution given in Table 3, and the same simulations were run for the spheres with a uniform diameter of the conglomerate mean size; 720, 1004, 1417 [μ], for the [20/40], [16/30], and [12/18] sorted proppants, respectively. In the figures, the legend assigns *[mesh]* for the model results with size distribution – demonstrated with a dashed line – and *S mesh* for the uniform spheres – presented with a solid line –, e.g., [20/40] for the simulation with size distribution and *S 20/40* for the simulation of uniform (720 μ) diameter spheres.

As expected, the proppant pack with unsorted particles indicates lower permeability and conductivity values; however, the difference in conductivity is slightly less. This phenomenon can be explained in Fig. 55 , where the fracture width in the function of the closure pressure is presented. In addition, one can observe that the fracture aperture is greater for the proppant pack with particle size distribution entailing a balancing effect concerning fracture conductivity. This analysis proves the double effect of unsorted granular materials, i.e., it blocks pore throats for fluid flow but mitigates deformation and fracture aperture reduction.

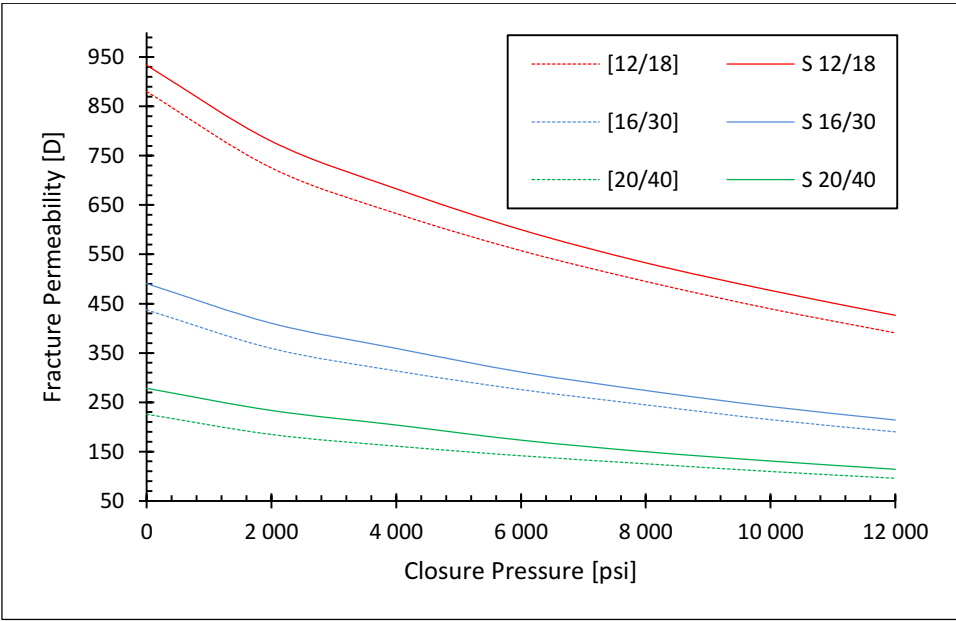


Fig. 53 Fracture permeability (edited by the Author)

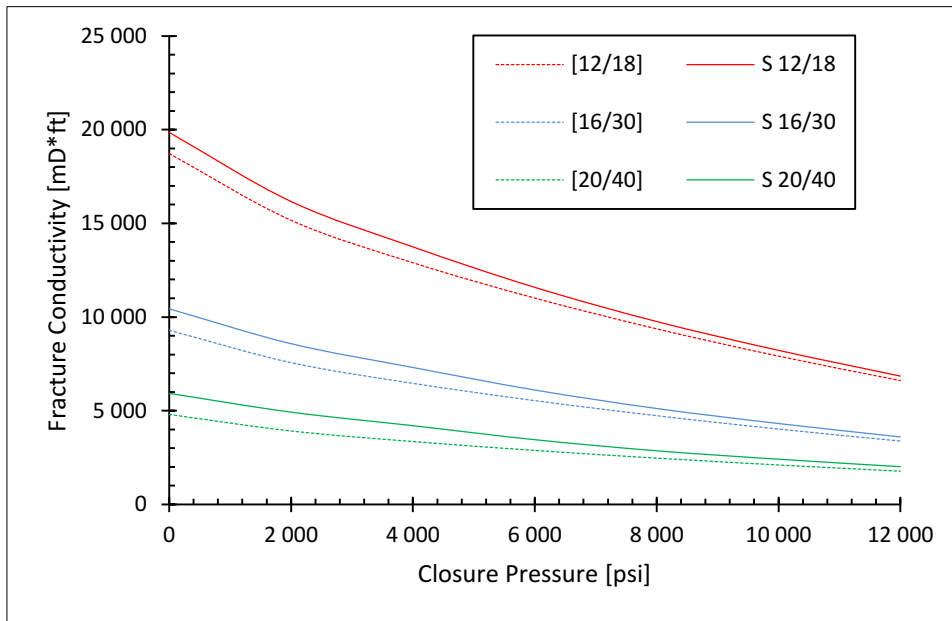


Fig. 54 Fracture Conductivity (edited by the Author)

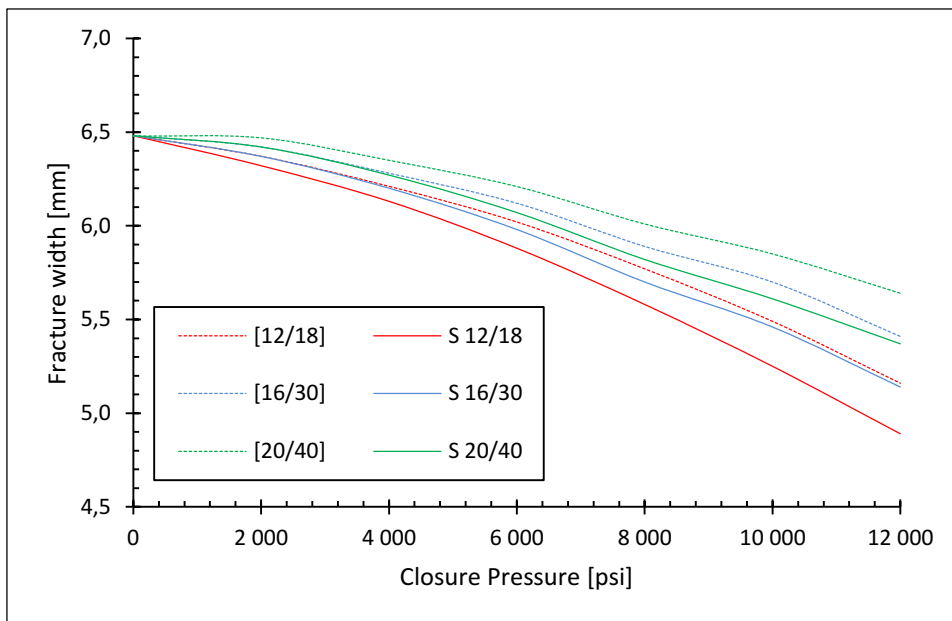


Fig. 55 Fracture width (edited by the Author)

Besides **Fig. 55**, **Fig. 56** was also created to highlight the impact of sorted proppant by eliminating the curves of [16/30] and S 16/30.

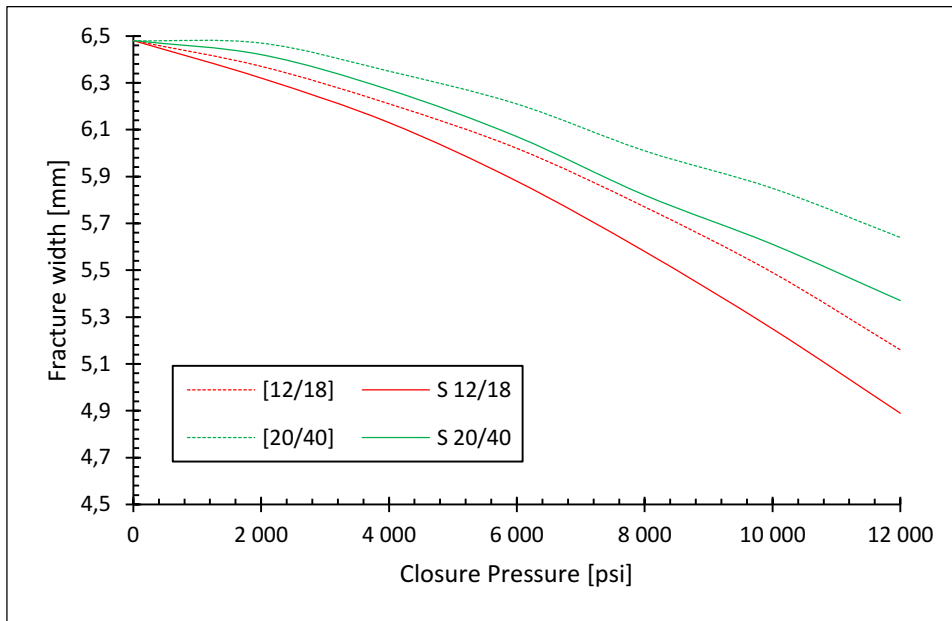


Fig. 56 Fracture width zoomed (edited by the Author)

4.6.3. Initial fracture geometry

Based on the sensitivity analysis results in **chapter 3.4.2.3**, the impact of initial fracture width was examined using the above numerical tools. In **Fig. 57**, one can see three different fracture widths of 4.23, 6.53, and 8.46 [mm].

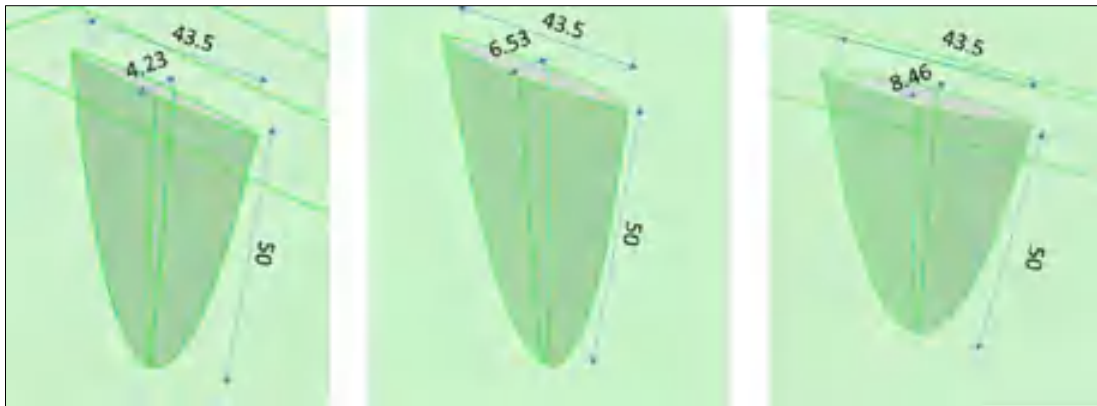


Fig. 57 Fracture widths (edited by the Author)

The variables, like closure pressure, formation Young's modulus, and proppant size, were fixed to median values of 50 [Mpa], 15 [Gpa], and 1 [mm], respectively, to eliminate the problem of ambiguity. With the application of the one-way coupling method, prominent results are achieved and demonstrated in **Fig. 58**.

Analyzing the results, one can obtain a controversial conclusion. The porosity and permeability decrease with increasing initial fracture aperture, while in the meantime, the fracture conductivity increases, as shown in **Fig. 59** . However, the analytical model did not show similar characteristics (in theory permeability remains constant according to the analytical model). The concept behind porosity reduction with increasing initial fracture width is the proppant arrangement — the greater the aperture, the greater the space, enabling the particles to pave more orderly, making the proppant pack more compact. This scientific finding is a relevant conclusion that may affect the fracturing treatment design perspectives.

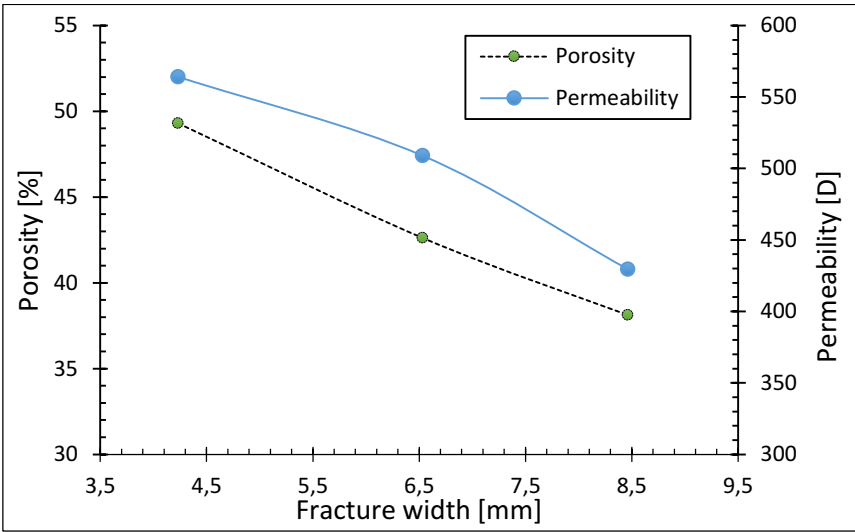


Fig. 58 Porosity and permeability as the function of fracture width (edited by the Author)

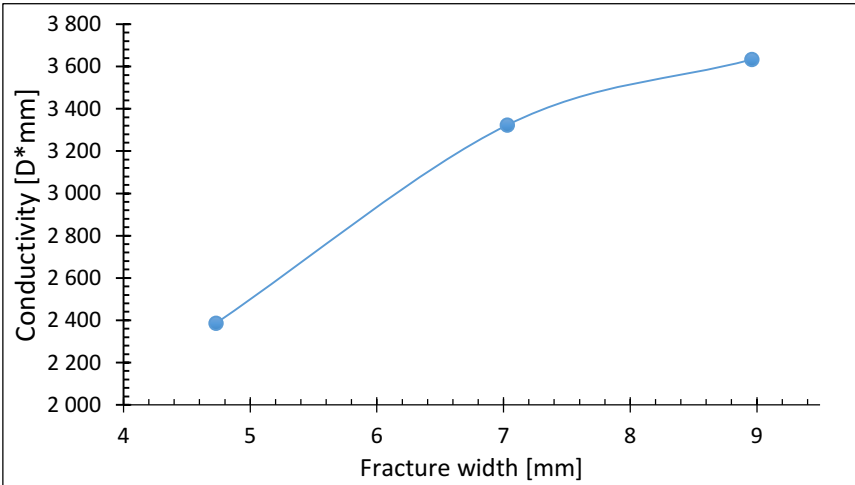


Fig. 59 Conductivity as the function of fracture width (edited by the Author)

4.6.4. Formation Young's modulus and closure pressure

The Young's modulus of the formation is a crucial parameter that the petroleum engineers planning and executing fracking jobs do not influence; however, it must be accounted for in hydraulic fracturing planning. This chapter provides sensitivity analysis based on the one-way coupling method presented above. The proppant deformation and embedment into the fracked rock induced by the closure stress are simulated in ANSYS SS, shown in **Fig. 60** .



Fig. 60 Propped fracture in ANSYS SS with fine mesh (edited by the Author)

The investigation was carried out for the formation Young's modulus of 2, 15, and 30 [Gpa], as described in model physics in chapter 4.1. The simulation results are demonstrated in **Fig. 61** , **Fig. 62** , and **Fig. 63** . As anticipated from previous results, the fracture permeability and width decrease with increasing closure pressure. Nonetheless, a significant difference is highlighted for the formations with varying elasticity.

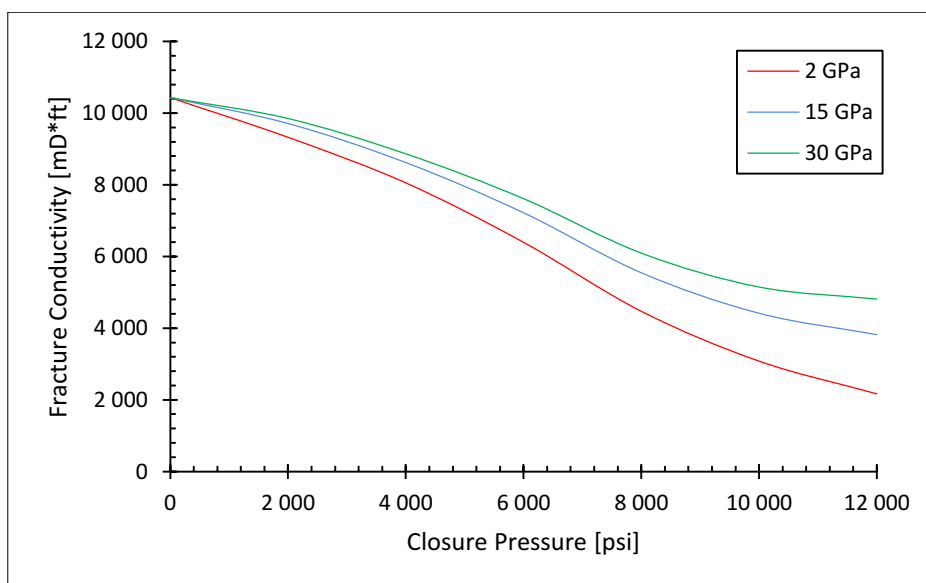


Fig. 61 Young's moduli impact on conductivity (edited by the Author)

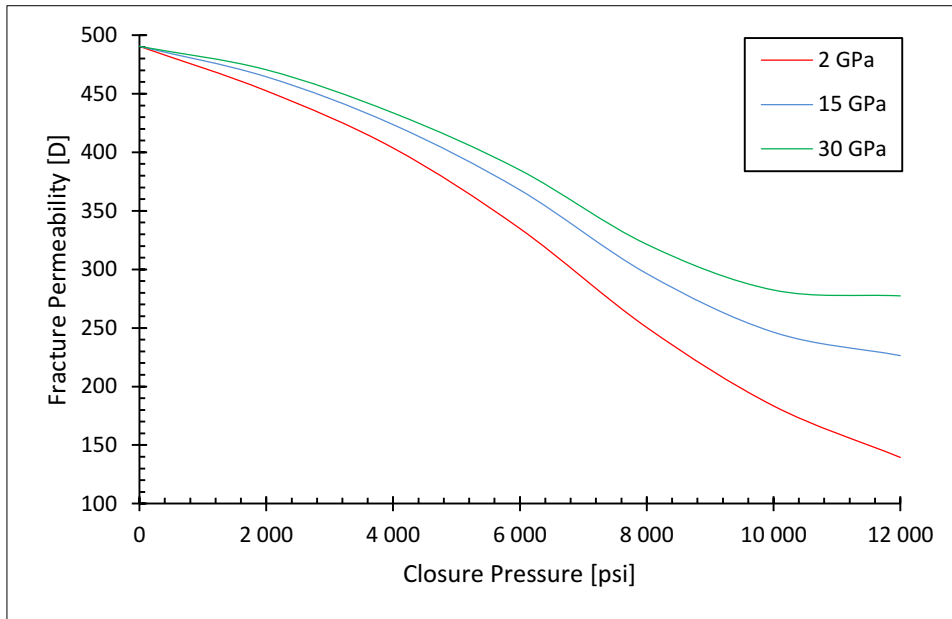


Fig. 62 Young's moduli impact on permeability (edited by the Author)

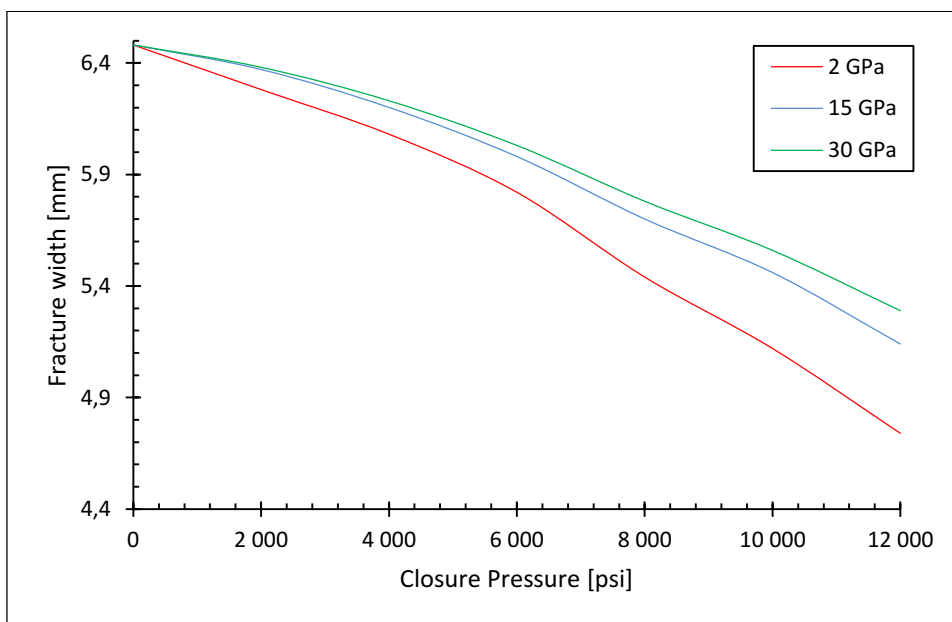


Fig. 63 Young's moduli impact on fracture aperture (edited by the Author)

The trends are aligned with expectations based on the analytical model findings. The greater the closure stress, the more relevant differences are marked for the given rock types. The difference between the 2 and 15 [Gpa] curves is much higher than between 15 and 30 [Gpa] ones, proving that above a certain elastic modulus, the mechanical deformation is driven asymptotically.

Fig. 64 was constructed to compare analytical -, analytical curves are dashed and labeled with An., - and numerical model results. One can notice the significant difference, though the curves' trends are similar and characteristic. The comparison demonstrates the limits of the analytical solution and highlights how much it underestimates even the initial conductivity.

The main reason for the underrated analytical conductivity can be the maximum achievable porosity of the proppant pack defined in 0.259 in chapter 3.4. However, in the contrary, the one-way coupling method also showed porosity above 0.35.

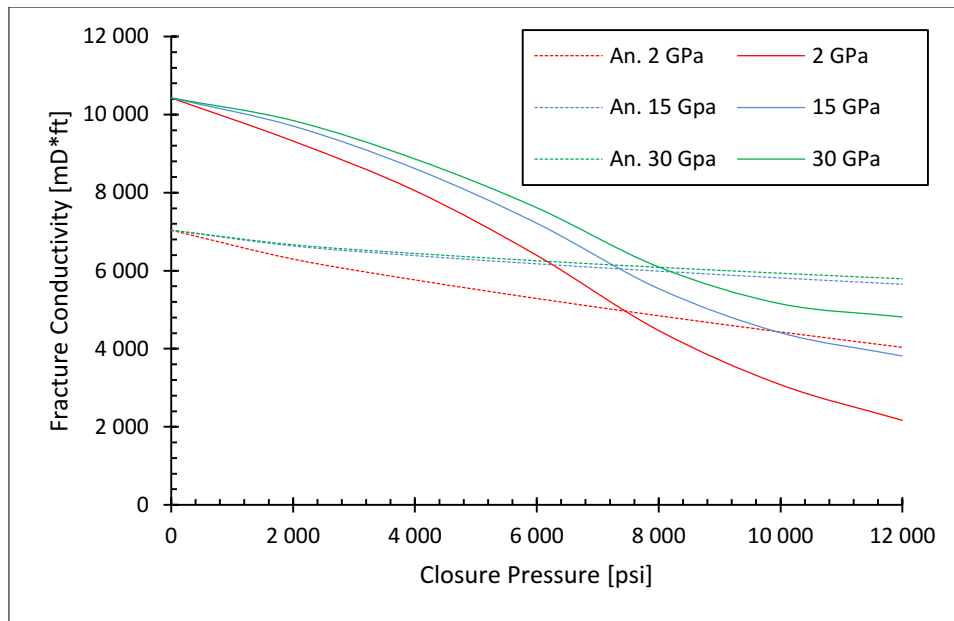


Fig. 64 An. and Num. conductivity results (edited by the Author)

To further investigate the reason behind the discrepancies, **Fig. 65** was created to separate the conductivity influencing factors, the permeability, and the fracture width. Simplified, the investigation of fracture width shows the mechanical deformation, and the permeability reflects the fluid dynamics. Therefore, analyzing **Fig. 65** and **Fig. 64**, one can conclude that the analytical method gives a significant error in permeability calculation because the analytical fracture width is greater than the numerical in **Fig. 65**, entailing a much less permeability.

In fact, the analytical method accounts for the capillary tube model for fluid flow within the pore space, which restricts the boundary condition – valid for laminar flow – and neglects many fluid dynamical considerations, e.g., lower pressure drop caused by non-regular geometry (in contrary with theory, channels may be formed due to the non-regularity).

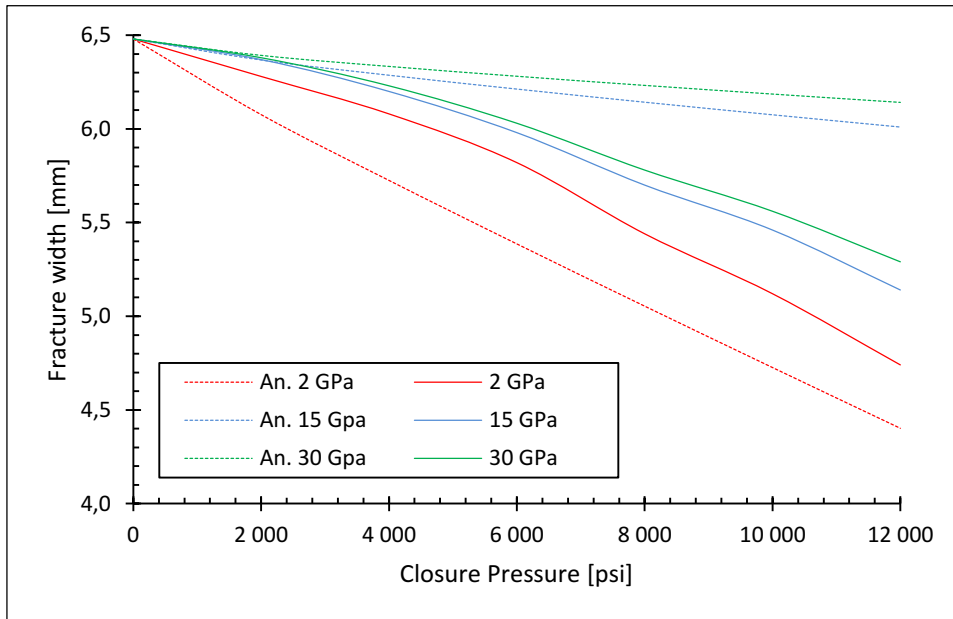


Fig. 65 An. and Num. fracture width results (edited by the Author)

4.7. Model Validation

Simulation models are used to examine a problem entity system, in this case, the system of a hydraulically cracked propped fracture, the proppant agent, the fluid media, and the interactions of these driven by the forces initiated by the pore – and closure pressure of the hydrocarbon-bearing reservoir. The validation and verification process belongs to the model development procedure, see **Fig. 66** , and makes the user ensured that the model behavior and outcomes are correct and the consequences drawn based on the results are truthful. Although the meaning of validation and verification is close to each other – and these terms are often used interchangeably, obviously incorrectly – it has a significant difference according to their definition.

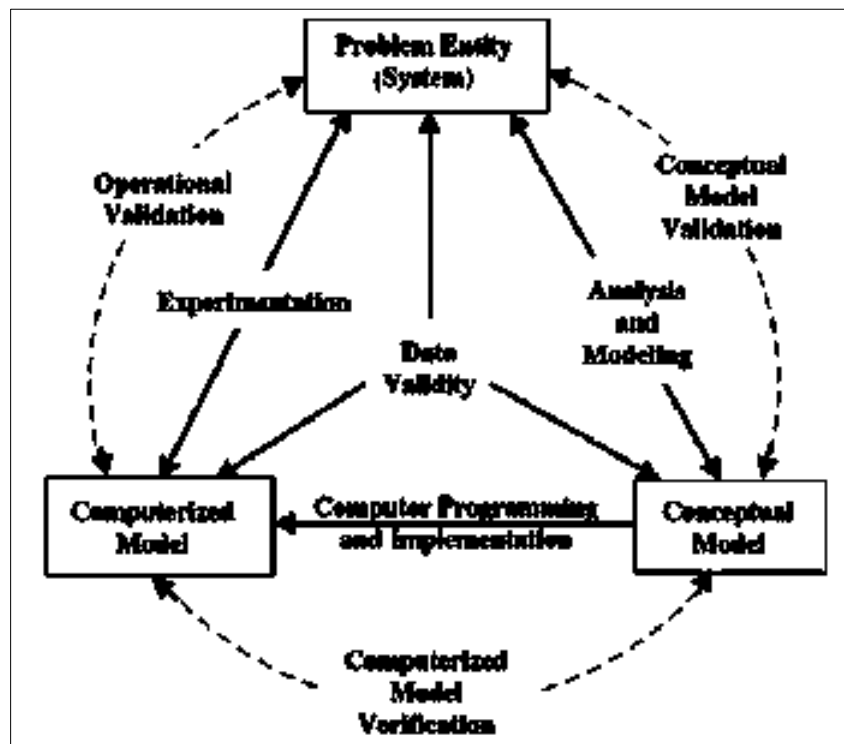


Fig. 66 Schematic of the model development process (Sargent, 2013)

Verification is the procedure that confirms that the model is producing the correct outcomes based on the relationships of input and output parameters built into the model. Contrary to the validation process, the verification does not rely on or compare to the problem entity system. Verification aims to confirm the model behavior and not the results' accuracy. Examining the results through sensitivity analysis – as it was done in **chapter 3** in the case of

the analytical model – is an impressive way to let the model be verified; therefore, it is presented in **chapter 4.6**.

Validation substantiates that a model within its domain of applicability holds a suitable range of accuracy compared to the real-world system, i.e., represents and approximates the phenomenon intended to be modeled adequately. There are many techniques to validate a computerized simulation model listed and summarized by Sargent (2013) like animation, face validity, extreme condition test, degenerate test, historical data validation, internal validity, data relationship correctness, predictive validation, structured walkthrough, multistage validation, philosophy of science, etc.

The method used to validate the coupled numerical model is comparing and matching the outcomes, i.e., propped width, permeability, and conductivity, with measured laboratory data, which process forms the part of both the multistage validation and the philosophy of science method. The multistage validation was introduced by Naylor and Finger (1967), who incorporated the elements of the philosophy of science method: rationalism, empiricism, and positive economics, into a multistep validation process. Rationalism involves a model to be rationally developed from a set of clearly declared assumptions, while empiricism entails the outcomes to be empirically, or most of the time, experimentally validated. The third term, positive economics, anticipates the model not to be disturbed by assumptions or the structure of the model.

4.7.1. API RP 19D

The empirical validation may rely intensely on the data collected from experiments; therefore, it is crucial to carry out measurements and percept data reasonably and precisely. The first intention to measure the rational parameter of manufactured proppants aroused in the late 1980s when the earliest standard for proppant permeability and conductivity measurement was introduced by the American Petroleum Institute in 1989 under the code of API RP 61, and the name of *Recommended Practices for Evaluating Short Term Proppant Pack Conductivity*. Since the experiment had a high uncertainty, an amendment was applied to the methodology, and a new apparatus began to spread in the Petroleum industry (Penny, 1987). The new method was more precise and enhanced to determine proppant conductivity under realistic conditions. The International Organization for Standardization adopted the method in 2008 under the code

DIN EN ISO 13503-5. The modified procedure got more popular than the original one; therefore, the American Petroleum Institute declared a new standard under the code of API RP 19D and with the name Recommended Practice for Measuring the Long-term Conductivity of Proppants. The main differences between the standards are summarized in **Table 4**. (Pusztai & Koroncz, 2021), and one can realize the most significant deviance in the temperature and duration of pressure steps which makes the API RP 19D last for 7-13 days; meanwhile the API RP 61 can be executed within hours.

Table 4. Difference between API RP 61 and 19D (edited by the Author)

Parameter	API RP 61	API RP 19D
Temperature	75 °F (24 °C)	250 °F (121 °C)
Fluid medium	Demineralized water	2% KCl solution
Closure body	Stainless steel	Ohio sandstone
Closing pressure	1,000 – 14,000 psi with 1,000 psi increment	2,000 – 10,000 psi with 2,000 psi increment
Loading rate	-	100 psi/min ± 5%
Duration of closing pressure	15 min	50 hours ± 2 hours

4.7.1.1. Test unit

Based on the standard DIN EN ISO 13503-5, the test unit shall be a linear flow design with a 64.5 cm² (10 in²) proppant bed area. **Fig. 67** demonstrates the details of the conductivity cell assembly. The pistons and test chamber shall be constructed of 316 stainless steel or Hastalloy material. Filters for the test unit may be constructed using Monel wire cloth with an opening of 150 [µm] or equivalent (100 US mesh).

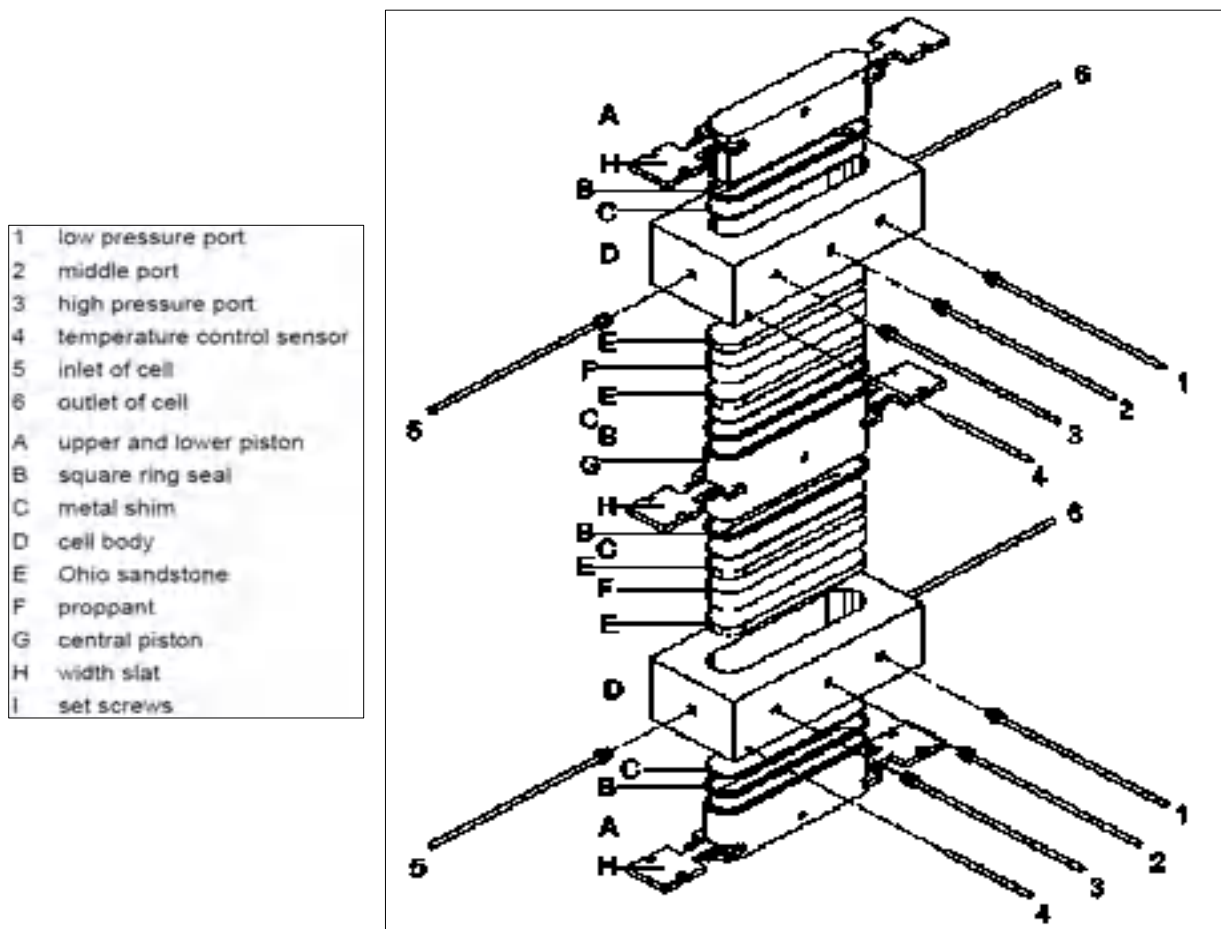


Fig. 67 Exploded view of conductivity cell (DIN EN ISO 13503-5, 2008)

4.7.1.2. Hydraulic load frame

The hydraulic load frame shall have sufficient capacity to develop 667 [kN] (150,000 lbs), which can generate ~ 1034 [bar] pressure within the cell. To ensure uniform stress distribution, the platens shall be placed parallel. The hydraulic pressurization source shall be capable of holding any desired closure stress [$\pm 1,0$ % or 3.4 bar, whichever is greater] for 50 [h]. The hydraulic load frame shall be capable of loading rate changes of 6.8 [bar/min]. A calibrated electronic load cell shall be used to calibrate the stress between the hydraulic ram and the opposing platen of the load frame.

4.7.1.3. Fluid drive system

A schematic diagram of the experimental setup is shown in **Fig. 68** . A high-precision metering pump (HPLC) provided a pulsation-free constant flow rate with a built-in pulsation

dampener unit. As per DIN EN ISO 13503-5, the injected fluid flows through a silica saturation cell and is filtered by a 0.5 micron sintered stainless-steel filter before entering the test cell. This fluid preparation step prevents the sandstone – and proppant dissolution, which boundary condition is also applied in the CFD model by assuming no reaction during fluid flow. The pressure drop between the pressure ports, measured with a differential pressure transducer with a range of 0.001 [kPa], is the main indication of the experiment and is used to determine the proppant pack permeability according to Darcy’s law :

$$k = \frac{Q \times \mu \times L}{A \times \Delta p}, \tag{53}$$

where k is the permeability in [$m^2=10^{-15} D$], Q is the flowrate in [m^3], μ is the dynamic viscosity of the medium in [Pas], L is the length the fluid passes through, i.e., the length between the pressure transducer ports, in [m], A is the cross-section of the porous media in [m^2], and Δp is the pressure drop indicated by the viscous forces against the motion in [Pa].

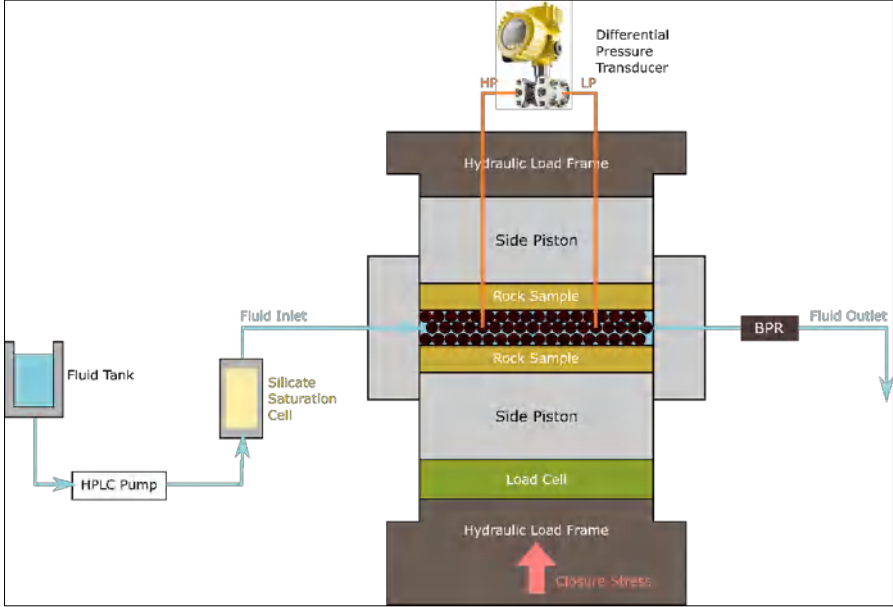


Fig. 68 Schematic setup of API RP 19D (Pusztai & Koroncz, 2021)

To represent the pore pressure, a back-pressure regulator (BPR) is used at the downstream side of the setup, which shall maintain a pressure of 20.7 to 34.5 [bar] according to DIN EN ISO 13503-5. Indeed, the stress applied to the cell shall consider the back-pressure for closure stress. For instance, if the backpressure is 3.45 [Mpa], the applied stress shall be 3.45 [Mpa] greater to consider the pressure exerted outward from the pistons.

Proppant is placed into the proppant conductivity cell between two sandstone cores, which, of course, have the same dimensions as the piston to perfectly match into the void of the measurement cell shown in **Fig. 69** . The dimensions of the cores, in fact, are slightly less than the dimensions of the piston because a thin RVT (room temperature vulcanizing) layer is applied to the slides of the cores, getting in touch with the cell's wall to prevent fluid leakage and make the system sealed.

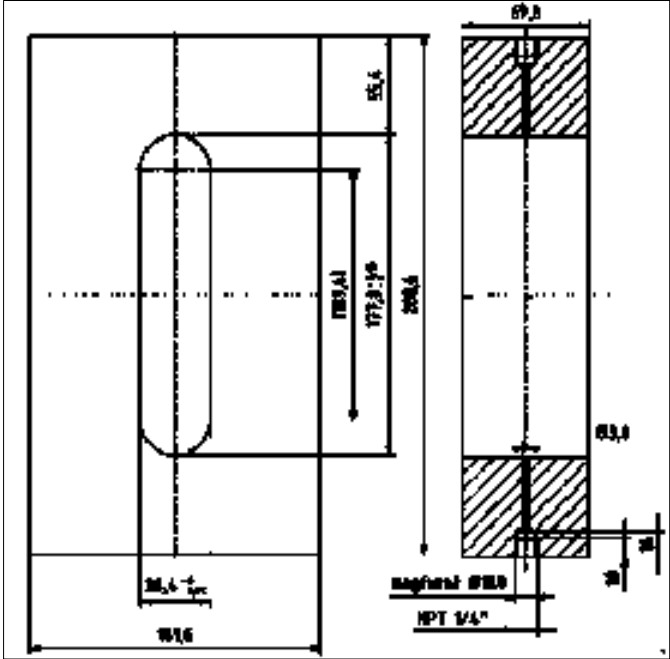


Fig. 69 Technical drawing of measurement cell with dimensions in [mm] (edited by the Author)

The width of the proppant pack is measured with two laser distance sensors with a range of 0.001 [cm] at both sides of the assembly. Initial zero pack width is measured without the proppant pack and used to calibrate the distance measurement system.

4.7.1.4. Temperature control

As per DIN EN ISO 13503-5, the test cell and proppant pack shall be maintained at the desired temperature ± 1 °C during the process. The temperature for the test conditions is measured in the temperature port of the conductivity cell shown in **Fig. 67** and used to determine the fluid viscosity, which is necessary to accurately calculate the permeability by Darcy's law (**Eq. 53**). The viscosity can be determined from viscosity tables (an example shown in **Fig. 70**) which consider the water temperature and salinity.

Table C.1 — 2 % KCl viscosity vs. temperature

Temperature			Viscosity								
°C	°F	cP	°C	°F	cP						
21,3	70	1,000 0	35,6	96	0,747 5	50,0	122	0,572 0	64,4	148	0,462 0
21,7	71	0,990 0	36,1	97	0,740 0	50,6	123	0,567 5	65,0	149	0,457 5
22,2	72	0,973 0	36,7	98	0,732 5	51,1	124	0,561 0	65,6	150	0,454 5
22,8	73	0,960 0	37,2	99	0,725 0	51,7	125	0,557 0	66,1	151	0,451 0
23,3	74	0,950 0	37,8	100	0,718 0	52,2	126	0,552 0	66,7	152	0,447 5
23,9	75	0,930 0	38,3	101	0,712 5	52,8	127	0,547 0	67,2	153	0,444 0
24,4	76	0,915 0	38,9	102	0,706 0	53,3	128	0,542 0	67,8	154	0,440 5
25,0	77	0,905 0	39,4	103	0,699 0	53,9	129	0,537 5	68,3	155	0,437 5
25,6	78	0,900 0	40,0	104	0,691 0	54,4	130	0,532 5	68,9	156	0,434 0
26,1	79	0,890 0	40,6	105	0,685 0	55,0	131	0,528 0	69,4	157	0,430 0
26,7	80	0,877 5	41,1	106	0,677 5	55,6	132	0,524 5	70,0	158	0,427 0
27,2	81	0,872 5	41,7	107	0,670 0	56,1	133	0,520 0	70,6	159	0,423 0
27,8	82	0,862 5	42,2	108	0,665 0	56,7	134	0,516 0	71,1	160	0,419 0
28,3	83	0,855 0	42,8	109	0,665 0	57,2	135	0,512 0	71,7	161	0,417 5
28,9	84	0,845 0	43,3	110	0,648 0	57,8	136	0,508 0	72,2	162	0,414 0
29,4	85	0,840 0	43,9	111	0,640 0	58,3	137	0,503 0	72,8	163	0,412 0
30,0	86	0,830 0	44,4	112	0,634 0	58,9	138	0,499 5	73,3	164	0,407 5
30,6	87	0,823 0	45,0	113	0,627 5	59,4	139	0,495 0	73,9	165	0,405 0
31,1	88	0,815 0	45,6	114	0,622 0	60,0	140	0,491 0	74,4	166	0,402 0
31,7	89	0,807 5	46,1	115	0,615 0	60,6	141	0,487 5	75,0	167	0,398 0
32,2	90	0,795 0	46,7	116	0,608 0	61,1	142	0,484 0	75,6	168	0,396 0
32,8	91	0,790 0	47,2	117	0,602 5	61,7	143	0,480 0	76,1	169	0,392 5
33,3	92	0,780 0	47,8	118	0,596 0	62,2	144	0,477 0	76,7	170	0,390 0
33,9	93	0,775 0	48,3	119	0,588 0	62,8	145	0,472 5	77,2	171	0,387 5
34,4	94	0,763 0	48,9	120	0,582 0	63,3	146	0,468 0	77,8	172	0,385 0
35,0	95	0,755 0	49,4	121	0,577 5	63,9	147	0,465 0	78,3	173	0,382 5

Fig. 70 Water viscosity (DIN EN ISO 13503-5)

Nevertheless, the viscosity of water also depends on the actual fluid pressure, even if it has a slight impact due to the compressibility factor of water. Therefore, to gain a more accurate viscosity value, the correlation introduced by McCain (1991) can be used:

$$\mu_{w1} = AT^{-B} \quad (54)$$

$$A = 109.574 - 8.40564 \times S + 0.313314 \times S^2 + 8.72213 \times 10^{-2} \times S^3 \quad (55)$$

$$B = 1.12166 - 2.63951 \times 10^{-2} \times S + 6.79461 \times 10^{-4} \times S^2 + 5.47119 \times 10^{-5} \times S^3 - 1.55586 \times 10^{-6} \times S^4 \quad (56)$$

$$\frac{\mu_w}{\mu_{w1}} = 0.9994 + 4.0295 \times 10^{-5} \times p_{abs} + 3.1062 \times 10^{-9} \times p_{abs}^2, \quad (57)$$

where μ_{w1} is the viscosity of water at a pressure of 1 bar [cP], T is the temperature [$^{\circ}$ F], p_{abs} is the absolute pressure [psi]; S is the salinity [wt %], and μ_w is the viscosity of water in reservoir conditions [cP].

4.7.2. Laboratory experiment

The measurement was carried out based on the above described API RP 19D in the laboratory of GEOCHEM (Geological and Environmental Research, Consultancy and Service) Ltd. with the incorporation of the Research Institute of Applied Earth Sciences in Kővágószőlős. Both institutes belong to CAPES (Cluster of Applied Earth Sciences). GEOCHEM is a research enterprise, having a high-tech equipped petrophysical laboratory, exceptional knowledge and ideas, significant innovation and development potential. The main scope of GEOCHEM is executing laboratory measurements and developing services in the field of geology, in particular with hydrocarbon and raw material exploration, geothermal energy research, carbon-dioxide sequestration, and radioactive and hazardous waste disposal.

Table 5. Proppant parameters (edited by the Author)

Parameter	MaxPROP ISP G2
Density	2.96 [g/cm ³]
Bulk Density	1.8 [g/cm ³]
Mesh size	16/30 [-]
Roundness	0.9 [-]
Sphericity	0.89 [-]

The proppant sample used for the conductivity measurement was supplied by MOL Plc. with the contribution of the service company Schlumberger Limited which actively accomplishes hydraulic fracturing treatments worldwide. **Table 5** summarizes the proppant characteristics provided by the technical data sheet attached in **Appendix 10.3**, and **Fig. 71** demonstrates the granular media of MaxPROP ISP G2. Based on the standard, the experiment is performed with an areal proppant concentration of 9.76 [kg/m²]; thus, the accurate proppant mass can be calculated accordingly.



Fig. 71 MaxPROP ISP G2 proppant (edited by the Author)

API RP 19D standard declares the usage of Ohio sandstone cores between which the proppant is placed; however, sandstone core samples with similar characteristics can be used as an alternative. Therefore, cores from the Kővágószőlős Formation – the detrital complex of the Upper Permian of the Mecsek mountains, Hungary – were used to substitute Ohio sandstone (Fig. 72).



Fig. 72 Proppant between cores from the Kővágószőlős Formation (edited by the Author)

4.7.2.1. Oxygen removal

Being the test based on the calculation of Darcy's law, the conductivity measurement must be carried out with single-phase, incompressible fluid flow. Therefore, the conductivity test fluid shall reduce the oxygen content to simulate reservoir fluids and minimize test

equipment corrosion. De-oxygenation can be performed with a two-reservoir system for the fluid.

The first reservoir holds fluid for oxygen removal and is connected to nitrogen gas bubbled through the liquid at low pressure below 103 [kPa] and at a low rate of 0.2-1.2 [dm³/min]. The nitrogen supply is first passed through an oxygen/moisture trap capable of removing oxygen to less than 15 [µg/l]. The second reservoir holds the oxygen-free fluid and supplies the oxygen-free water for the fluid drive system. All fluids in each reservoir are held in sealed, inert-gas blanketed containers to prevent oxygen contamination from the air.

4.7.2.2. Procedure and data acquisition

The proppant placement into the cell should be done precisely to ensure even proppant distribution and parallel core and piston setup. The calculated proppant mass, 63.5 [g], should be divided into four portions and filled into the cell, split by markers into four equal volumes along with the cell. The filled measurement cell after markers removal is shown in **Fig. 73** .



Fig. 73 Standard conductivity measurement cell (edited by the Author)

After the core and proppant sample preparation – core cut, sample grinding, and sanding, subsequently application of RVT layer for seal, measuring proppant sample weight with a digital precision scale with the range of 0.01 [gram] in glass flask – the measurement cell was assembled, i.e., the lower piston was placed into the cell, seal ring and metal shim were installed, then the prepared sandstone was carefully placed on the top of them, the proppant sample was filled evenly, and finally, an upper assembly was arranged the same way as down. Placing the flexible assembly of pistons, cores, proppant, etc., into the fixed – to the load frame – measurement cell is complicated because centralization must be kept accurately; however, it is a crucial step that must be precise to gain valuable results.

When all the preconditions are settled, the measurement system can be assembled, and the procedure can be initiated. Initial absolute stress of 5.08 [Mpa] was applied for 1 hour to let the proppant particles be arranged, and the system stabilized at the room temperature of 21.4 [°C]. The back-pressure regulator was maintained at about 2.14 – 3.02 [Mpa]. This value was taken into account when the closure stress was applied. In **Fig. 74**, one can see the conductivity assembly of GEOCHEM Laboratory, where the tests were conducted.

After the initial stress of 5,08 [Mpa] was achieved and held, the applied closure stress was raised to 30.6 [Mpa]. After the initial stress, stresses applied to the proppant pack were held for 50 [h]. Closure stresses increased in 14.4 [Mpa] increments after that. The closure pressure ramp rates were 689 [kPa/min].



Fig. 74 Fracture conductivity measurement system in GEOCHEM's laboratory
(edited by the Author)

Conductivity, i.e., pressure difference, was measured at 5.08, 27.58, 41.37, 55.16, and 68.95 [Mpa] (0.74 kpsi, 2 kpsi, 4 kpsi, 6 kpsi, 8 kpsi, and 10 kpsi), as it is suggested for ceramic and resin-coated proppants.

Test flow rates were determined according to the pressure drop between the pressure ports. Instead of the minimum flow rate of 2 [ml/min] specified in the standard, a flow rate of 2.6 [ml/min] was used, and at the end of the loading cycles, four flow rates were applied to determine the permeability a statistical way. The flow rate and the minimum pressure drop (0.01 [kPa]) are monitored and adjusted if required to fit the pressure drop into the pressure transducers' range.

Pack widths were measured at each stress and calculated to subtract out the compression of the sandstone cores and the expansion of the metal. Before each measurement, the differential pressure transducers have been zeroed.

Acquiring closure stress, pore pressure, temperature, flow rate, and proppant pack width values is a key part of the data processing system. The conductivity test duration – e.g., the measurement we carried out lasted 150 hours – and monitoring the measured parameters

frequently requires a computer-based data processing system. In this case, a data collection and processing system of every 10 seconds was applied, which aided in gaining measurement with ~ 77,000 records.

4.7.2.3. Conductivity results

After all the connections are established, initial stress of 5.08 [Mpa] is applied, as discussed in **chapter 4.7.2.2**. This initial compressive load makes the proppant arranged – despite the even proppant filling, some peaks and volleys could be formed, which can get flat by the initial burden – and also prevents particle displacement during the fluid flow, which could make the pressure transducer or even the fluid flow ports – inlet, outlet pipes – plugged. **Table 7** presents the measured and calculated values recorded in the first 3 minutes of the experiment: elapsed time t [s], closure pressure P_c [bar], pore pressure P_p [bar], closure stress [bar]; i.e., the difference between closure pressure and pore pressure, level transmitter value at both sides of the cell $LT-321/2$ [mm], fracture widths calculated from LT-321/2: w_{f1} , w_{f2} , and w_{avg} [mm], cross-section A [cm²], flow rate Q [ml/min], pressure difference indicated by pressure transducers Δp [mbar], temperature T [°C], and permeability k [D], respectively.

Even if the records are measured in a steady-state condition, the values vary in a certain limited range requiring an automatic data acquisition system that can log data with the given frequency to establish a valuable database.

In the following, Table 6 sums the relevant measured and calculated values averaged for closure pressure steps, while Fig. 75 , Fig. 76 , Fig. 77 , Fig. 78 , Fig. 79 present the average permeability and conductivity, the average fracture width, and the set of permeability and conductivity points measured during the measurement. In Appendix **10.4**, the conductivity values as a function of time are shown in Fig. IX and the temperature logged during the procedure in Fig. X .

Table 6. Result summary (edited by the Author)

Average Measured Values					
Closure stress [psi]	290	4,000	6,000	8,000	10,000
Permeability [D]	564.2	509.0	429.5	328.0	190.9
Fracture width [mm]	4.700	4.589	4.381	4.245	4.055
Conductivity [mD·ft]	8,699	7,662	6,173	4,568	2,539

Table 7. Lab records (edited by the Author)

Elapsed Time [hh:mm:ss]	P _c [bar]	P _p [bar]	Closure Stress [bar]	LT-321 [mm]	LT-322 [mm]	w _{f1} [mm]	w _{f2} [mm]	w _{fAVG} [mm]	A [cm ²]	Q [ml/min]	Δp [mbar]	T [°C]	k [D]
0:00:00	50.8	29.4	21.4	31.8	30.5	4.7	4.7	4.7	1.80245	2.2	0.50	21.4	534.0
0:00:11	50.8	29.2	21.6	31.8	30.5	4.7	4.7	4.7	1.80245	2.2	0.48	21.5	552.4
0:00:21	50.8	29.2	21.6	31.8	30.5	4.7	4.7	4.7	1.80245	2.2	0.47	21.4	572.2
0:00:31	50.8	29.4	21.4	31.8	30.5	4.7	4.7	4.7	1.80245	2.2	0.47	21.4	572.2
0:00:41	50.8	29.2	21.6	31.8	30.5	4.7	4.7	4.7	1.80245	2.2	0.47	21.3	572.2
0:00:51	50.8	29.2	21.6	31.8	30.5	4.7	4.7	4.7	1.80245	2.2	0.48	21.4	552.4
0:01:01	50.8	29.5	21.3	31.8	30.5	4.7	4.7	4.7	1.80245	2.2	0.48	21.4	552.4
0:01:12	50.8	29.5	21.3	31.8	30.5	4.7	4.7	4.7	1.80245	2.2	0.48	21.3	552.4
0:01:22	50.8	29.9	20.9	31.8	30.5	4.7	4.7	4.7	1.80245	2.2	0.48	21.5	552.4
0:01:32	50.8	29.5	21.3	31.8	30.5	4.7	4.7	4.7	1.80245	2.2	0.47	21.4	572.2
0:01:42	50.8	29.5	21.3	31.8	30.5	4.7	4.7	4.7	1.80245	2.2	0.45	21.4	593.4
0:01:52	50.8	29.5	21.3	31.8	30.5	4.7	4.7	4.7	1.80245	2.2	0.47	21.4	572.2
0:02:02	50.8	29.9	20.9	31.8	30.5	4.7	4.7	4.7	1.80245	2.2	0.48	21.5	552.4
0:02:12	51.1	29.5	21.6	31.8	30.5	4.7	4.7	4.7	1.80245	2.2	0.50	21.5	534.0
0:02:22	50.8	29.9	20.9	31.8	30.5	4.7	4.7	4.7	1.80245	2.2	0.45	21.5	593.4
0:02:33	51.1	29.9	21.2	31.8	30.5	4.7	4.7	4.7	1.80245	2.2	0.48	21.4	552.4
0:02:43	50.8	29.9	20.9	31.8	30.5	4.7	4.7	4.7	1.80245	2.2	0.47	21.4	572.2
0:02:53	50.8	29.9	20.9	31.8	30.5	4.7	4.7	4.7	1.80245	2.2	0.50	21.3	534.0
0:03:03	51.1	29.9	21.2	31.8	30.5	4.7	4.7	4.7	1.80245	2.2	0.47	21.5	572.2

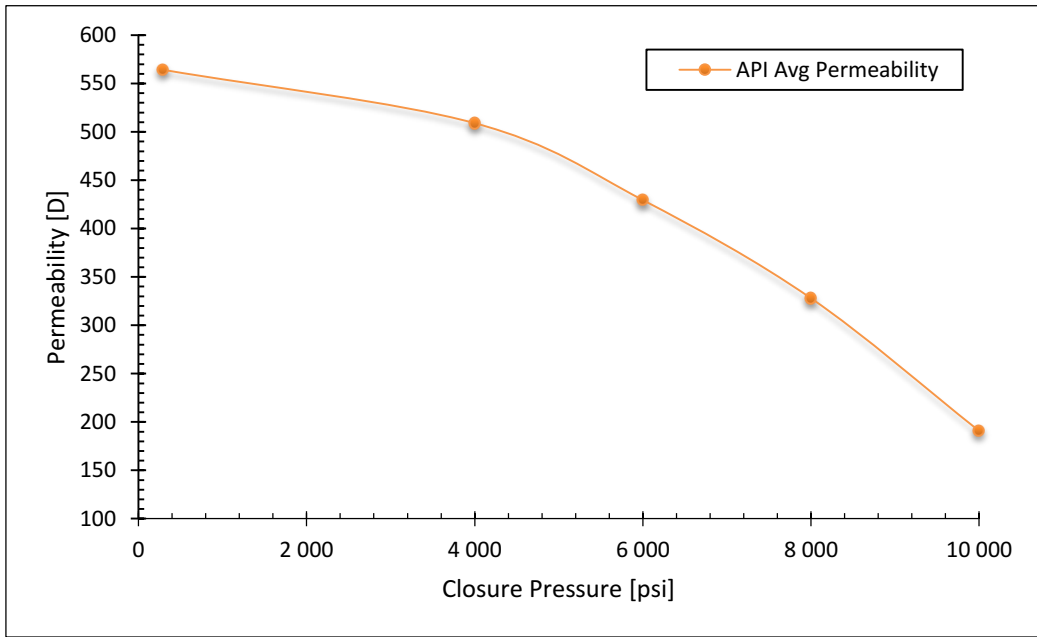


Fig. 75 Average Permeability (edited by the Author)

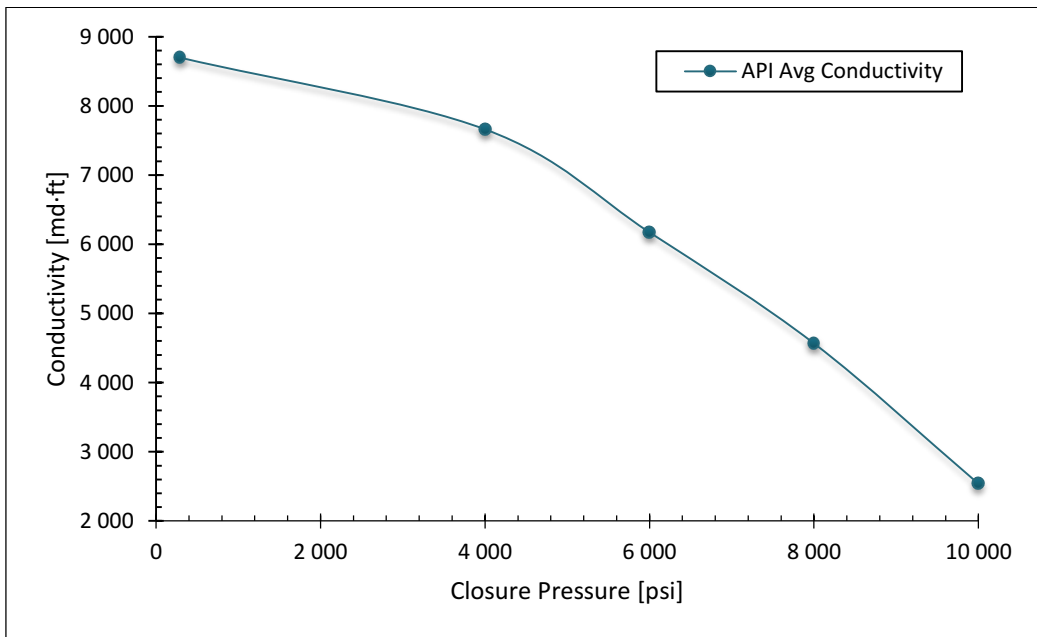


Fig. 76 Average conductivity (edited by the Author)

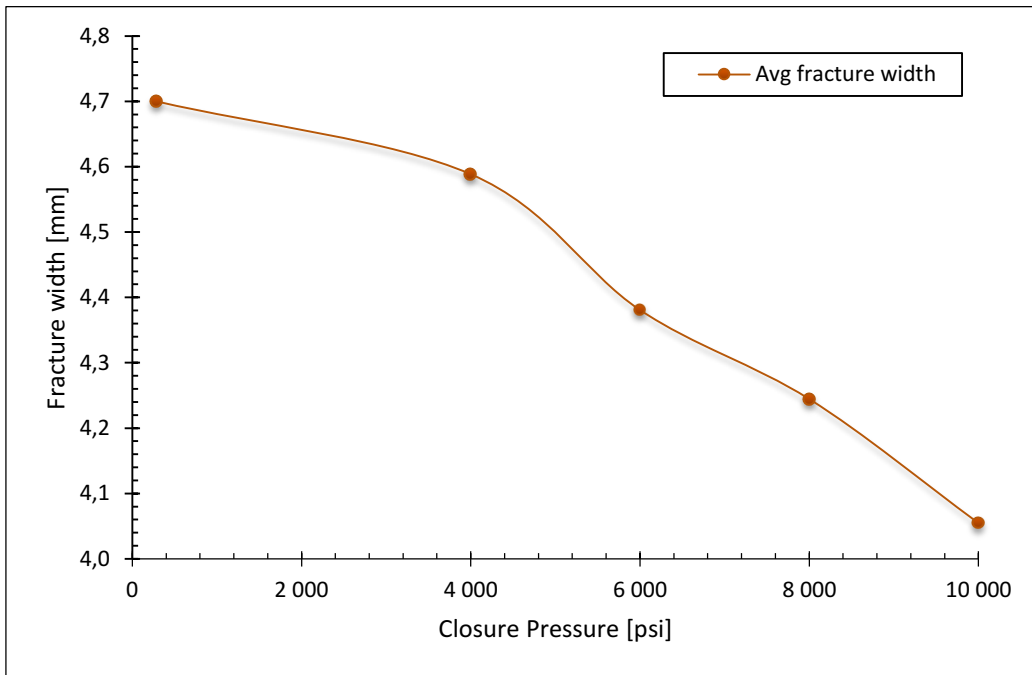


Fig. 77 Average fracture width (edited by the Author)

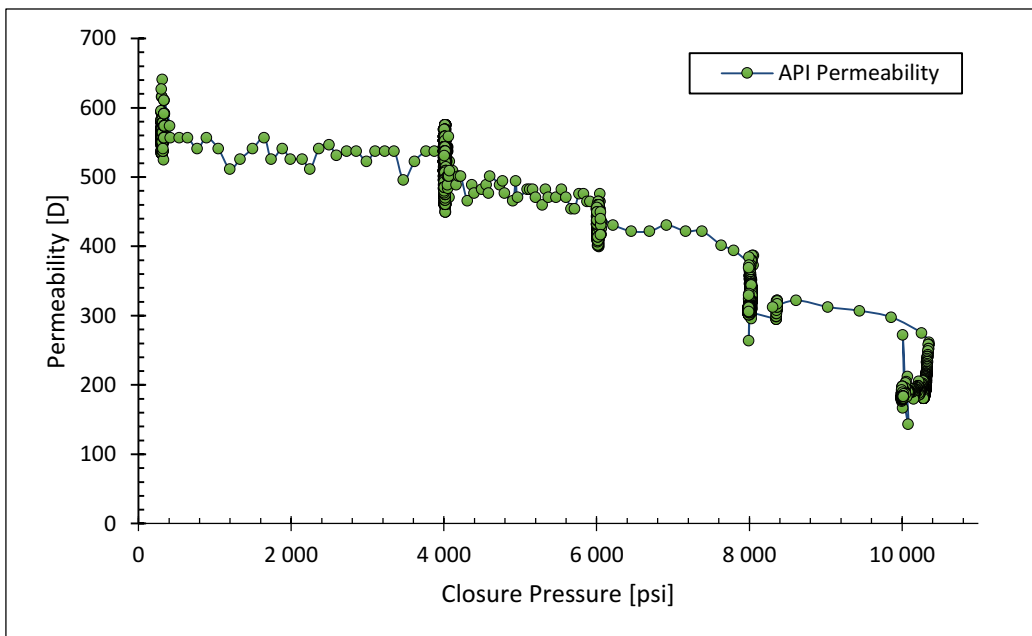


Fig. 78 Set of permeability points (edited by the Author)

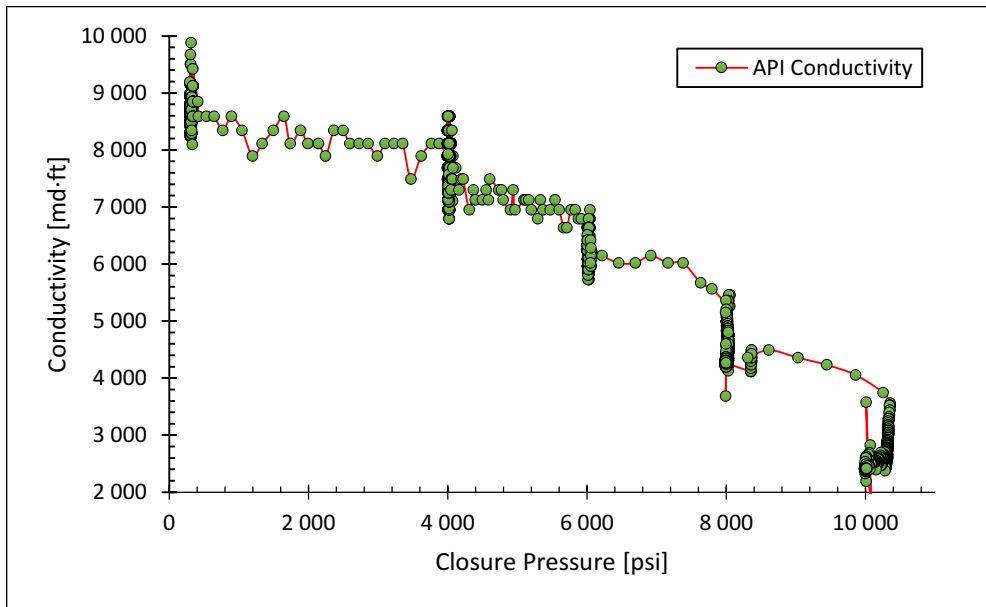


Fig. 79 Set of conductivity points (edited by the Author)

4.7.3. Simulation results

The simulation for model validation was carried out based on the one-way coupling method presented in **chapter 4.4**. The YADE script is attached in **Appendix 10.6**, describing all the steps required to generate, drop, and place the proppant particles in the measurement cell introduced above. First, the particles are randomly generated in a virtual box just above the cell and then dropped into the assembly by gravity, shown in **Fig. 80**.

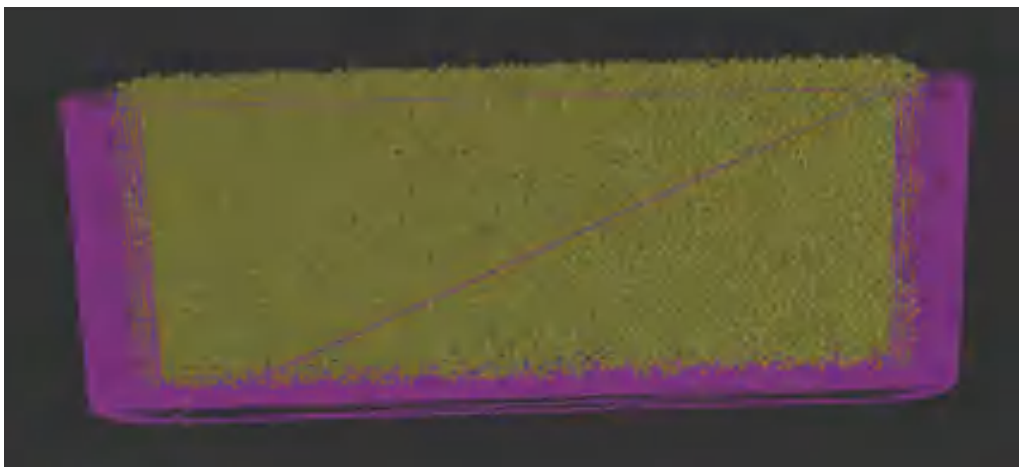


Fig. 80 Generation of proppant particles (edited by the Author)

Due to the numerous collisions of particles, a steady-state condition should be achieved, which is controlled by the measure of unbalanced forces – the ratio of maximum contact force and maximum per-body force; the measure of staticity, and computed with *unbalancedForce* command shown in **Appendix 10.6** – and presented in **Fig. 81** . The iteration is stopped when the unbalanced force drops below 0.5.

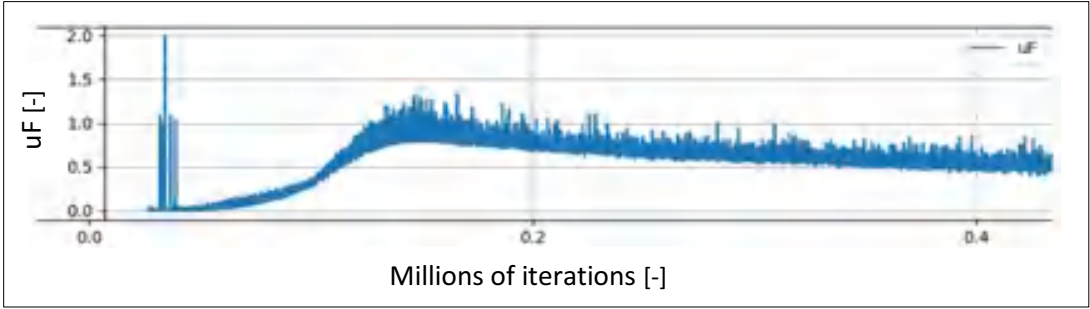


Fig. 81 Unbalanced Force (edited by the Author)

Once the force-balance condition is reached, a plane is pushed to the conglomeration of proppants from the top with a force of 39.93 [kN] acting on the cell area – 79.85 cm² – generates ~ 50 [bar] to represent the initial proppant arrangement. **Fig. 82** shows the proppant arrangement after flattening.

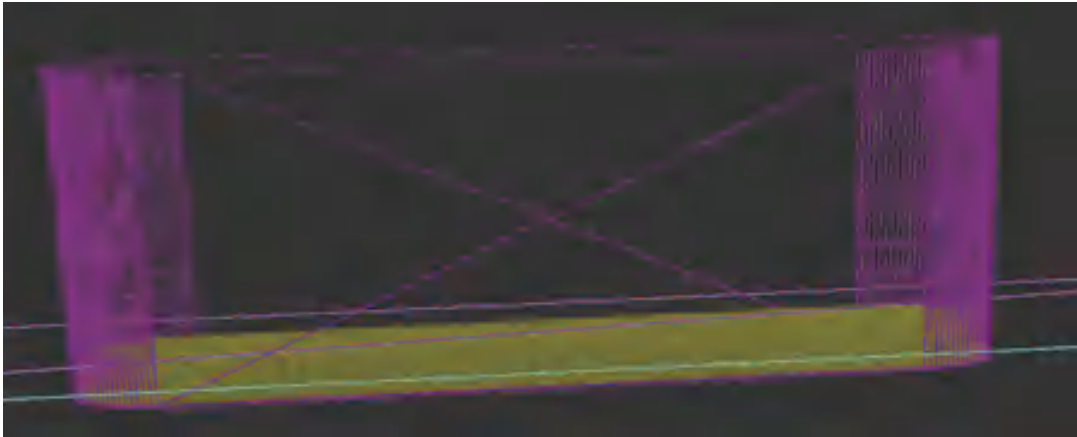


Fig. 82 Proppants placed and arranged (edited by the Author)

Subsequently, as described in the one-way coupling method, the DEM result was exported into ANSYS static structural and then into the ANSYS CFX environment, shown in **Fig. 83** .

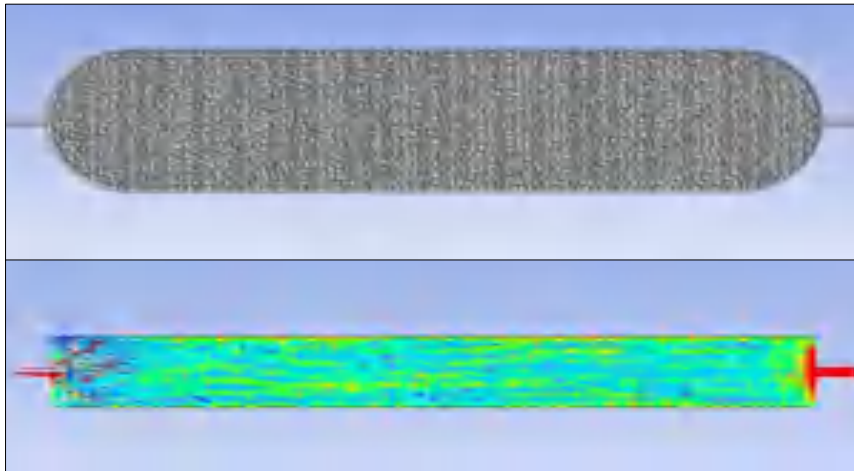


Fig. 83 Filled API cell and fluid flow (edited by the Author)

Different meshing was applied in ANSYS SS and CFX for two kinds of investigation, i.e., mechanical deformation and fluid dynamics analysis. While the proppant particles and the fracture wall were meshed in the static structural module, the pore space between the proppant was meshed for the computational fluid dynamics module.

The one-way coupling method results are summed up and compared to the API data measured in the laboratory in Fig. 84 , Fig. 85 , Fig. 86 , and Table 8, Table 9, Table 10, Table 11. In the figures, the result of the analytical method introduced in **chapter 3** is also shown pointing out its big deviation compared to the outcomes of the experiment and the numerical model.

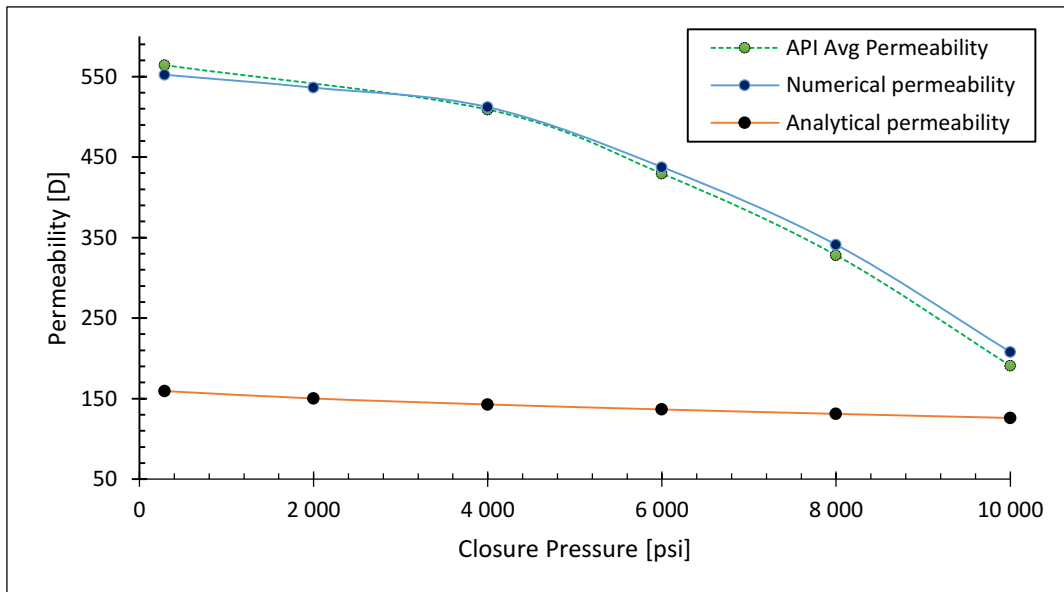


Fig. 84 Measured, numerical and analytical permeability (edited by the Author)

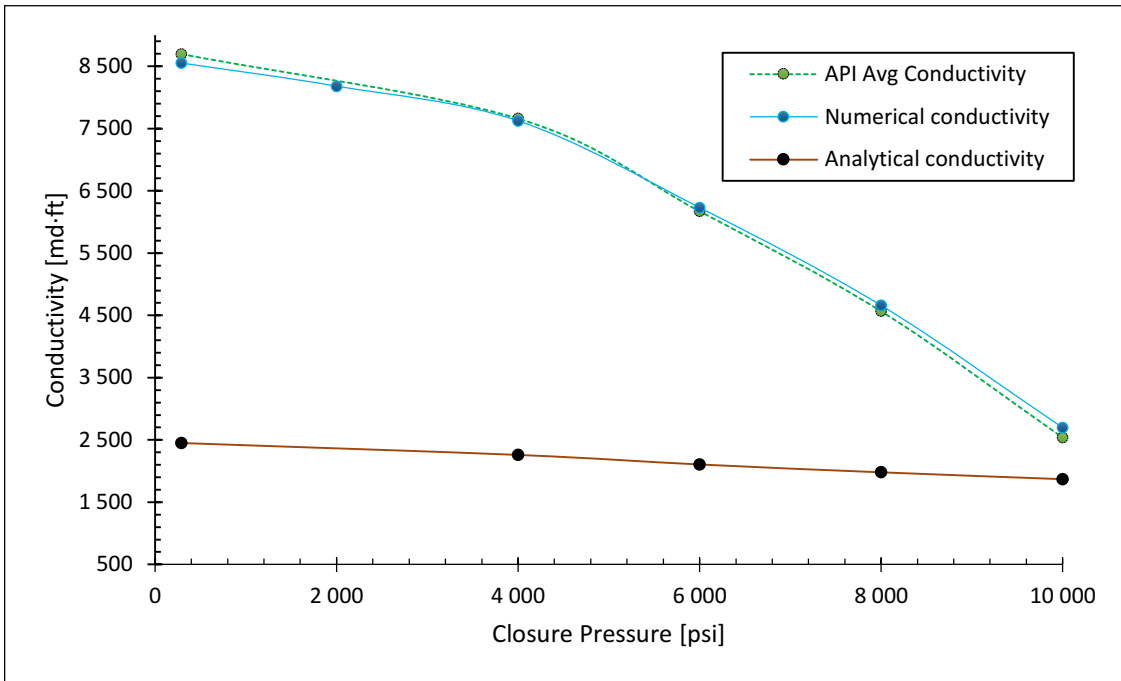


Fig. 85 Measured, numerical and analytical conductivity (edited by the Author)

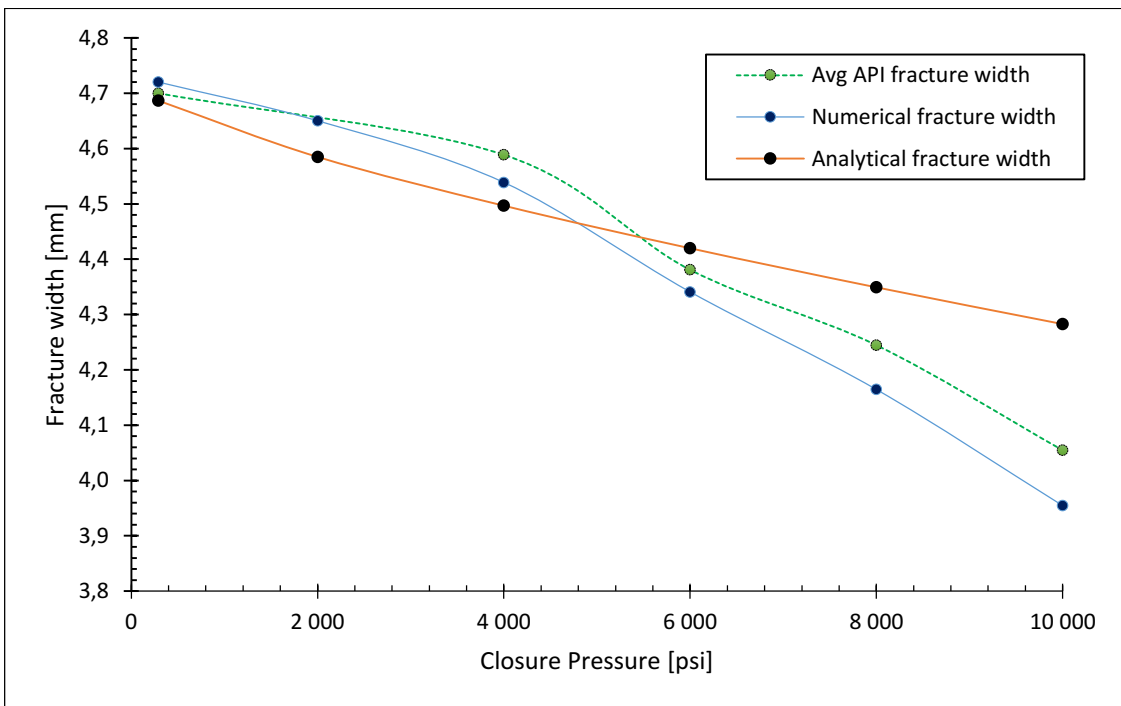


Fig. 86 Measured, numerical and analytical fracture width (edited by the Author)

Table 8. Average Measured Data (edited by the Author)

Average Measured Values					
Closure pressure [psi]	290	4,000	6,000	8,000	10,000
Permeability [D]	564.2	509.0	429.5	328.0	190.9
Fracture width [mm]	4.700	4.589	4.381	4.245	4.055
Conductivity [mD-ft]	8,699	7,662	6,173	4,568	2,539

Table 9. One-way Coupling Results (edited by the Author)

One-way Coupling Method					
Closure pressure [psi]	290	4,000	6,000	8,000	10,000
Permeability [D]	552.2	512.0	437.5	341.0	207.9
Fracture width [mm]	4.720	4.539	4.341	4.165	3.955
Conductivity [mD-ft]	8,550	7623	6231	4659	2697

Table 10. Absolute Difference (edited by the Author)

Difference					
Closure pressure [psi]	290	4,000	6,000	8,000	10,000
Permeability [D]	12.0	-3.0	-8.0	-13.0	-17.0
Fracture width [mm]	-0.02	0.05	0.04	0.08	0.10
Conductivity [mD-ft]	148.8	38.8	-57.6	-91.5	-158.0

Table 11. Relative Difference (edited by the Author)

Difference [%]					
Closure pressure [psi]	290	4,000	6,000	8,000	10,000
Permeability	2.2	-0.6	-1.8	-3.8	-8.2
Fracture width	-0.4	1.1	0.9	1.9	2.5
Conductivity	1.7	0.5	-0.9	-2.0	-5.9

Based on the analysis above, one can observe that the one-way coupling method resulted in outcomes aligned with the lab data. **Table 10** summarizes the absolute differences, and **Table 11** highlights the relative differences as the percentage of the computed data. The one-way coupling method slightly underestimates the permeability and consequently the conductivity for low closure pressure and approximates the measured data from the top in case of higher

closure pressure. The contrary can be drawn for fracture aperture change. The one-way coupled method demonstrates a thicker aperture for low closure pressure and a thinner for higher closing forces.

This phenomenon can be examined from many aspects. On the one hand, the numerical model does not consider proppant crush, which may take place in case of high closure pressure and limit fluid flow but, in the meantime, may diminish aperture reduction due to the support provided by the fragments of small particles. On the other hand, the measurement's uncertainty should also be considered. For example, Richard et al. (2019) showed that standardization is a crucial point in the API RP 19D measurement, and the results might show a variance as high as 20 %. The leading actor impacting the variance is the initial proppant arrangement. Therefore, the placement of the proppant sample was further standardized by introducing partition development within the cell. Four equal volume was separated in the cell body to fill four equal mass of proppant with a precision of decimal gram. Finally, the variance of permeability and conductivity was reduced to 3.9% and 5.4%, respectively (Pusztai & Koroncz, 2021).

If the laboratory data are considered benchmark data (relative differences are shown in **Fig. 87**), and all the possible variations of the physical situation are ignored, the major relative difference is 8.2 % in permeability values for 10,000 [psi]. Nevertheless, the error for the main parameter, i.e., the conductivity, is less than 6 %, implied by the reverse variation in fracture width. Finally, the minor differences between the results of the API RP 19D experiment and the computed model outcomes conclude the integrated numerical model established by the one-way coupling method to be validated.

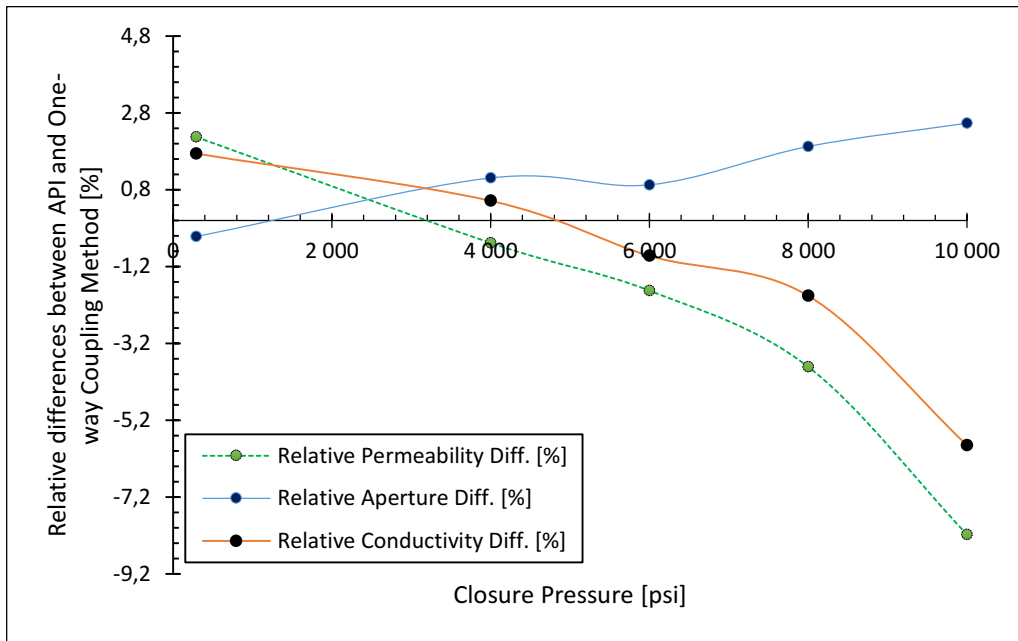


Fig. 87 Relative differences with API reference basis (edited by the Author)

5. SCIENTIFIC ACHIEVEMENTS

Novel scientific results have been found during the research conducted and presented above. This chapter summarizes the scientific findings and forms the theses.

5.1. Thesis #1

I developed a Discrete Element Model, presented in **chapter 4.2**, to describe the random proppant placement within the fracture. The gravitational drop makes the particles roll and slide on each other and contains tangential displacement components, i.e., enables interactions of both collision and friction. In addition, I incorporated inhomogeneity by applying particle geometry other than a sphere and considering proppant size distribution. Finally, I verified the established model by the calibration procedure of a silo outflow experiment.

5.2. Thesis #2

I established a complex Finite Element Model (Structural and Computational Fluid Dynamics), published in **chapter 4.5**, to determine the proppant deformation and embedment into the hydrocarbon-bearing formation, and to simulate and investigate the fluid dynamics within the fracture inside the porous media formed by the compacted proppant pack.

In **chapter 4.7**, I proved the validity of the Structural and Computation Fluid Dynamics model, based on the standard API RP 19D. The results showed an excellent matching enabling me to examine fluid flow and determine the pressure drop across the domain examined. Based on this new method, the primary outcome of the hydraulic fracturing treatment – the fracture permeability and conductivity – can be determined.

5.3. Thesis #3

I evolved the one-way coupling method – presented in **chapter 4.4** – to establish an interface of DEM-FEM-CFD simulation and incorporate the benefits of different numerical approaches. Based on the method, complex mechanical analysis of propped hydraulic fractures can be performed. The established method can be interpreted as my primary research achievement and can be a pioneering technique for practicing field engineers.

5.4. Thesis #4

Based on the one-way coupling method, I found that the initial fracture aperture hurts the proppant pack porosity and, therefore, the permeability. However, the fracture conductivity increases with the initial fracture width; due to the higher degree of freedom, the proppant particles are forced to be arranged more orderly, entailing less interconnected effective porous space between the particles for fluid flow. The result is obtained in **chapter 4.6.3** and demonstrated in **Fig. 58** and **Fig. 59** .

5.5. Thesis #5

I showed the application of clumps in **chapter 4.6.1** to develop non-regular elements – differing from spheres – in DEM. The analysis highlighted the combination of four spheres to substitute spheroidal particles; however, it was excluded from the further investigation because of the slight impact on porosity and permeability with conspicuous time-consuming computational requirements.

5.6. Thesis #6

I proved that the proppant geometry impact on fracture conductivity is less significant than the effect of particle size distribution. This finding confirms the geological and rock mechanics theory, i.e., the less sorted the granular media – it consists of more ranges of particle diameter – the less porosity can be reached based on the phenomenon of smaller fragments might be placed within the pore throat of larger particles. Nevertheless, this analysis, in **chapter 4.6.2.1**, also found that the tiny particles restrict the pore throat concerning fluid flow and provide support against fracture closure resulting thicker fracture aperture.

5.7. Thesis #7

Based on the research, I demonstrated the limits of the analytical model presented in **chapter 3** and I drew the following conclusions:

- The analytical model supposes perfect spheres with the same diameter for all the particles; however, the granular media is sorted by sieves with a given size distribution, and their shape is characterized by sphericity and roundness indices.
- It assumes no friction between the particles, i.e., no tangential displacement component – friction traction – is considered.
- The Hertz model supposes the contact surface developed between the contacting objects is flat; however, the stiffer body domes into the softer object.
- The analytical solution is based on infinitesimal strain assumptions, which may conclude errors due to geometrical nonlinearities of finite deformation.
- Another limiting factor is the assumption of the Kozeny-Carman model, i.e., it is only valid for laminar flow.
- It applies the most compact, even proppant arrangement, i.e., the maximum achievable initial porosity is 0.259, which is not valid for most cases.

6. SUMMARY

Hydraulic fracturing treatment enhances well productivity, usually drilled in tight or less permeable reservoirs, forming high-conductive channels between the formation and the wellbore. After fracturing, the closure pressure indicates a closing action prevented by proppant particles placed between the fracture walls and carrying the load by the complex stress condition. Even if proppants are enormously strong and the strength of the hydrocarbon-bearing layer is relatively high, proppant deformation and embedment take place and may result in a significant reduction of the created fracture conductivity, particularly under high closure pressure circumstances.

The research conducted and presented in the Thesis developed a state-of-the-art method to model in-situ fracture behavior by coupling DEM-FEM-CFD numerical solutions. First, DEM was applied to generate and randomly place proppants into the fracture; meanwhile, FEM Static Structural module was used to let the proppants be deformed and embedded into the formation, and finally, the Computational Fluid Dynamics application was coupled to investigate the permeability and conductivity of the propped fractures.

This research showed that achievable fracture conductivity increases with the increase of proppant size and formation stiffness; however, it decreases with the increment of fracture-aperture-closing stress. Of course, these trends fit the results published by many researchers before, but the absolute value of the simulation results pointed out new perspectives of fracture behavior modeling. As a result, many fundamental factors – such as fracture geometry, proppant geometry, proppant size, uneven proppant and proppant size distribution, deformation, embedment, and fluid dynamics – have been integrated into the one-way coupling model.

The research demonstrated the capability of DEM-FEM-CFD coupling for modeling multidisciplinary processes regarding hydraulic fracturing and provided insight into the factors that drive the complex interactions between proppant particles, formation stiffness, and closure pressure. The outcome of this research may advance the fundamental understanding of proppant embedment and deformation and contribute to a broad scale of applied sciences that aim to optimize hydraulic fracturing.

7. ÖSSZEFOGLALÁS

A hidraulikus rétegrepesztés, az olajipar upstream divíziójában használt, kút produktivitást növelő rétegszerkentő eljárás. Legtöbbször mély, kevésbé áteresztő formációkba fúrt kutak esetén alkalmazzák, hogy intenzifikálják azok hozamát, azáltal, hogy nagy vezetőképességű porózus közeget (proppant pack) hoznak létre a repedésekben. A művelet során, miután a szénhidrogént tároló kőzet megreped a kútba szivattyúzott repesztőfolyadék által gerjesztett feszültségek miatt, a repesztőfolyadékba kitámasztóanyagot, ú.n. proppantot kevernek, hogy az a repedésbe érve kitámassza azt, és megakadályozza a repedés visszazáródását. Még ha a proppant és a kőzet nagy szilárdságú is, proppant deformáció és – beágyazódás jelensége figyelhető meg, amely komoly hatással lehet a kialakított repedés vezetőképességére.

Az értekezés bemutatja a PhD hallgató kutatási tevékenységét, mely során a szerző kifejlesztett egy, a tudomány mai állása szerint új, innovatív, kapcsolt numerikus módszert a kitámasztott repedések viselkedésének mechanikai vizsgálatára. A kapcsolt numerikus DEM-FEM-CFD módszer integrálja a Diszkrét Elem -, valamint Végeelem Módszerek megoldásait. A szerző Diszkrét Elem Módszert alkalmazott a proppant szemcsék véletlenszerű generálására, valamint repedésbe való random elhelyezésére, majd a repedésbe helyezett proppantok deformációját, kőzetbe való ágyazódását, és az így kialakult geometria áramlástani vizsgálatát végezte el Végeelem Módszert használó szoftverek segítségével.

A kutatás eredményeképp megállapítható, hogy a repedés konduktivitás csökken a záródási nyomással, valamint növekszik nagyobb méretű proppantok és nagyobb rugalmassági modulusszal rendelkező rezervoárok esetén. Természetesen ezek az általános érvényű megállapítások már korábban, számos más szerző által evidenciát nyertek, ugyanakkor az abszolútértelemben vett eredmények értékelése új távlatokat jelölhet ki a hidraulikus rétegrepesztés modellezésével foglalkozó mérnökök számára. Végeredményben megállapítható, hogy a szerző sikeresen kapcsolta össze a különböző numerikus módszereket alkalmazó szoftvereket, valamint számos, eddig meg nem oldott, ámde alapvető fontosságú tényezőt -, mint pl. repedés és proppant geometriát, egyenetlen proppant, és ez által feszültség eloszlást, különböző méretű és méreteloszlással rendelkező proppant elhelyezését, valamint nem-lineáris deformációt, beágyazódást és valós áramlástani jellemzőket, – integrált a kapcsolt numerikus modellbe.

8. PUBLICATIONS PRESENTED IN THE THESIS' TOPIC

8.1. Articles and proceedings

- Pusztai, P., Lengyel T. (2015): A Hidraulikus Rétegrepszítés Gazdasági Optimalizációja, Diáktudomány c. kiadvány, VIII. kötet, ISSN 2062-07-21, Miskolc, 2015.
- Jobbik, A., Lengyel, T., Pusztai, P. (2015): Összetett Matematikai Modell Hidraulikus Rétegrepszítés Optimalizálására, Miskolci Egyetem Műszaki Földtudományi Közlemények Kőolaj és Földgáz kötet 85, pp. 97-105., ISSN 2063-5508, Miskolc, 2015.
- Jobbik, A., Lengyel, T., Pusztai, P. (2016): An Innovative Method for Hydraulic Fracturing Optimization, Proceedings of the 4th International Scientific Conference on Advances in Mechanical Engineering (ISCAME 2016), pp. 302-307., ISBN:978-963-473-944-9, Debrecen, 2016.
- Lengyel, T., Jobbik, A. (2017): Kombinált Analízis Rendszer a Proppant Kiválasztás Optimalizálására, Műszaki Tudomány Az Észak-Kelet Magyarországi Régióban, Elektronikus Műszaki füzetek, ISBN 978-963-7064-35-7, Nyíregyháza, 2017.
- Lengyel, T. (2017): Repedés Konduktivitást Befolyásoló Tényezők Vizsgálata, Diáktudomány c. kiadvány, X. kötet, ISSN:2062-07-21, Miskolc, 2017.
- Lengyel, T., Jobbik, A. (2020): Combined Analysis System for Proppant Selection in Aspect of Fracture Conductivity, Geosciences and Engineering, a Publication of the University of Miskolc (Miskolc University Press). HU ISSN 2063-6997, Miskolc, 2020.
- Lengyel T., Jobbik, A. (2017): Integrated Model for Proppant Selection Optimization, Proceedings of 13th International Conference on Heat Engines and Environmental Protection, ISBN: 978-963-420-907-2, Budapest, 2017.
- Lengyel, T., Jobbik, A. (2017): Proppant Optimalizálás a Repedés Konduktivitást Befolyásoló Tényezők Figyelembe Vételével, Miskolci Egyetem Műszaki Földtudományi Közlemények, ISSN 2063-5508, Miskolc, 2017.
- Lengyel, T., Jobbik, A., Tóth, A. (2018): An Analytical Approach for Propped Fracture Conductivity, 18th International Multidisciplinary Scientific Geoconference – SGEM 2018 Conference Proceedings, Volume 18, Science and Technologies in Geology, Exploration and Mining, Issue 1.4, ISBN 978-619-7408-38-6, ISSN 1314-2704, DOI: 10.5593/sgem2018/1.4, Sofia, Bulgaria, 2018.

Lengyel, T. (2018): “Analytical Approach for Propped Fracture Conductivity”, Conference Proceedings of Spring Wind 2018 Conference, ISBN 978-615-5586-31-6, DOI: 10.23715/TSZ.2018.1, Budapest, 2018.

Pasztor, A., Lengyel, T. (2019): Method to calculate apparent permeability of hydraulic fractures. International Multidisciplinary Scientific Geoconference 19, 19(1.2), pp. 985-992., ISBN: 978-619-7408-77-5, ISSN: 1314-2704, Sofia, Bulgaria, 2019.

Varga, A., Lengyel, T., Safranyik, F. (2020): Determination of micromechanical parameters of proppant particles, International Journal of Innovative Research in Advanced Engineering, (2349-2163): 7 2 pp 15-21, 2020

Lengyel, T., Varga, A. (2020): Proppant szemcsék kifolyásvizsgálata, Miskolci Egyetem Műszaki Földtudományi Közlemények, ISSN 2063-5508, Miskolc, 2020.

Lengyel, T., Varga, A. (2021): Proppant szemcsék mikromechanikai paramétereinek meghatározása, Mérnöki és Informatikai Megoldások, <https://doi.org/10.37775/EIS.2021.1.>, 2021

Lengyel, T.; Varga, A.; Safranyik, F.; Jobbik, A. (2021): Coupled Numerical Method for Modeling Propped Fracture Behavior. *Appl. Sciences*. 2021, 11, 9681. <https://doi.org/10.3390/app11209681>

8.2. Conference presentations

Numerical Modeling of Proppant Deformation and Embedment, 5th ICSTR Singapore – International Conference on Science & Technology Research, Singapore, 26-27 March, 2021

Modeling Proppant Deformation and Embedment, 23rd International Conference on Multidisciplinary Studies “Resilience for Survival”, Cambridge, 30-31 July 2020

Apparent Permeability of Fractures, 6th Annual Student Energy Congress – ASEC 2019, SPE Student Chapter, University of Zagreb, Zagreb, 2019

Analytical Approach for Propped Fracture Conductivity, Tavaszi Szél Konferencia, Győr, 2018

An Analytical Approach for Propped Fracture Conductivity, 18th International Multidisciplinary Scientific Geoconference – SGEM 2018 Conference, Sofia, 2018

Combined Analysis System for Proppant Selection in Aspect of Fracture Conductivity, XXXI. Nemzetközi Olaj- és Gázipari Konferencia, Siófok, 2017

An Innovative Method for Hydraulic Fracturing Optimization, 4th International Scientific Conference on Advances in Mechanical Engineering, Debrecen, 2016

Investigation of parameters influencing fracture conductivity including proppant pack properties and rock mechanical characteristics, „Új kutatási irányok a földi energiaforrások hasznosításához kapcsolódóan” című szakmai tudományos konferencia, Miskolc, 2017

Barents Sea – Eastern Finnmark Platform, AAPG – Imperial Barrel Award, Prague, 2017

Integrated Model for Proppant Selection Optimization, 13th International Heat Engines and Environment Protection Conference, Budapest, 2017

Kombinált Analízis Rendszer a Proppant Kiválasztás Optimalizálására, Műszaki Tudomány az Észak-kelet Magyarországi Régióban, Nyíregyháza, 2017

9. REFERENCES

- Alvaro, C., Jimenez, J.R. (2003): Estimation of Moduli and Densities of Rock Constituents through Global Inversion of Wire-line Data. In Proceedings of the 2003 SEG Annual Meeting, Dallas, TX, USA.
- Bagi, K. (2012): Fundamentals of the Discrete Element Method, 1st ed. (Budapest University of Technology and Economics: Hungary, Budapest, 2012) p. 73.
- Balázs, L. (2013): Kőzetfizika. Egyetemi jegyzet geofizikus M.Sc. hallgatók számára (Eötvös Lóránd Tudomány Egyetem, 2013) ISBN 978-963-284-381-0
- Barree, R., Conway, M. (1995): Experimental and Numerical Modeling of Convective Proppant Transport (includes associated papers 31036 and 31068). *J. Pet. Technol.* 1995, 47, p. 216–222, <https://doi.org/10.2118/28564-pa>.
- Barree, R., Cox, S., Barree, V., Conway, M. (2003): Realistic Assessment of Proppant Pack Conductivity for Material Selection. *Soc. Pet. Eng.*, <https://doi.org/10.2118/84306-ms>.
- Bathe, K.J., Saunders, H. (1984): Finite Element Procedures in Engineering Analysis. *J. Press. Vessel. Technol.* 1984, 106, p. 421–422, <https://doi.org/10.1115/1.3264375>.
- Brannon, Harold D., Malone, Mark R., Rickards, Allan R., Wood, William D., Edgeman, J. Randall, and Josh L. B. (2004): Maximizing Fracture Conductivity with Proppant Partial Monolayers: Theoretical Curiosity or Highly Productive Reality? Paper presented at the SPE Annual Technical Conference and Exhibition, Houston, Texas, September 2004. <https://doi.org/10.2118/90698-MS>
- Chen, M., Zhang, S., Liu, M., Ma, X., Zou, Y., Zhou, T., Li, N., Li, S. (2018): Calculation method of proppant embedment depth in hydraulic fracturing. *Pet. Explor. Dev.* 2018, 45, p. 159–166, [https://doi.org/10.1016/s1876-3804\(18\)30016-8](https://doi.org/10.1016/s1876-3804(18)30016-8).
- Cinco, H.L., Samaniego, F.V., Dominguez N.A. (1978): Transient Pressure Behavior for a Well with a Finite-Conductivity Vertical Fracture. *Soc. Pet. Eng. J.* 1978, 18, p. 253–264, <https://doi.org/10.2118/6014-pa>.
- Cooke, C.J. (1973): Conductivity of Fracture Proppants in Multiple Layers. *J. Pet. Technol.* 1973, 25, p. 1101–1107, <https://doi.org/10.2118/4117-pa>.
- Csizmadia, B., Nándori, N. (1999): Mechanika mérnököknek, Szilárdságtan (Tankönyvkiadó, Budapest, 1999)
- Cundall, P.A., Strack, O.D.L. (1979): A discrete numerical model for granular assemblies. *Geotechnique* 1979, 29, p. 47–65, <https://doi.org/10.1680/geot.1979.29.1.47>.
- Darrigol, O. (2002): Between Hydrodynamics and Elasticity Theory: The First Five Births of the Navier-Stokes Equation. *Archive for History of Exact Sciences*, 56(2), p. 95–150. <http://www.jstor.org/stable/41134138>

- Denney, D. (2010): Thirty Years of Gas-Shale Fracturing: What Have We Learned? *J. Pet. Technol.* 2010, 62, p. 88–90, <https://doi.org/10.2118/1110-0088-jpt>.
- Dintwa, E., Tisjkens, E., Ramon, H. (2007): On the accuracy of the Hertz model to describe the normal contact of soft elastic spheres. *Granular Matter* 10, p. 209-221, Springer, DOI 10.1007/s10035-007-0078-7
- Economides, M., Nolte, K. (2000): *Reservoir Stimulation*, 3rd ed. (John Wiley and Sons: Hoboken, NJ, USA, 2000) ISBN 978-047-149-192-7
- Economides, M.J., Tony, M. (2007): *Modern Fracturing: Enhancing Natural Gas Production* (ET Publishing: Houston Gulf Publishing Co, TX, USA, 2007) p. 96. ISBN 978-160-461-688-0
- Égert, J., Keppler, I. (2007): *A végeselemmódszer mechanikai alapjai* (Universitas-Győr Kft., Győr, 2007)
- Ross, E. (2011): Channel Fracturing, *Unconventional Resources*, *New Technology Magazine*
- Fan, M., Han, Y., McClure, J., Chen, C. (2017): Hydraulic Fracture Conductivity as a Function of Proppant Concentration under Various Effective Stresses: From Partial Mono-layer to Multi-layer Proppants. *Soc. Pet. Eng.* 2017, <https://doi.org/10.15530/urtec-2017-2693347>.
- Fan, M., McClure, J., Han, Y., Ripepi, N., Westman, E., Gu, M., Chen, C. (2019): Using an Experiment/Simulation-Integrated Approach to Investigate Fracture-Conductivity Evolution and Non-Darcy Flow in a Proppant-Supported Hydraulic Fracture. *SPE J.* 2019, 24, p. 1912–1928, <https://doi.org/10.2118/195588-pa>.
- Fredd, C., McConnell, S., Boney, C., England, K. (2000): Experimental Study of Hydraulic Fracture Conductivity Demonstrates the Benefits of Using Proppants. *Soc. Pet. Eng.* 2000, <https://doi.org/10.2118/60326-ms>.
- Gonzalez-Montanello, C., Ramírez, Á., Gallego, E., Ayuga, F. (2011): Validation and experimental calibration of 3D discrete element models for the simulation of the discharge flow in silo, *Chemical Engineering Science*, Vol. 66 (21), p. 5116-5126.
- Guo, B., Liu, X., Tan, X. (2017): *Petroleum Production Engineering* 2nd ed. (Gulf Professional Publishing, 2017) p. 389-501, ISBN 9780128093740, <https://doi.org/10.1016/B978-0-12-809374-0.00014-3>.
- Guo, J., Liu, Y. (2012): Modeling of Proppant Embedment: Elastic Deformation and Creep Deformation. *Soc. Pet. Eng.*, <https://doi.org/10.2118/157449-ms>.
- Hertz H. (1895): Über die Berührung fester elastischer Körper (*Gesammelte Werke*, Leipzig, 1895) p. 155-173. Originally published in *Journal f. d. reine u. angewandte Mathematik* 92, p. 156-171, 1881.
- Hubbert, M.K., Willis, D.G. (1957): Mechanics of Hydraulic Fracturing. *Trans. AIME* 1957, 210, p. 153–168, <https://doi.org/10.2118/686-g>.
- Huitt, J.L., McGlothlin, B.B. (1958): The Propping of Fractures in Formations Susceptible to Propping-sand Embedment, Paper presented at the spring meeting of the Pacific Coast

- District, Division of Production, Los Angeles, California, May, 1958. SPE-58-115-MS. <http://dx.doi.org/10.2118/58-115 MS>.
- ISO 13503-5:2006: E. Procedures for measuring the long-term conductivity of proppants. Petroleum and natural gas industries – Completion fluids and materials – Part 5, Geneva, Switzerland, ISO, 2006.
- John, D.A. (1995): Computational Fluid Dynamics, the Basics with Applications International Editions, 1st ed. (McGraw-Hill Inc.: New York, NY, USA, 1995) p. 60–75.
- Keppler, I. (2013): Failure analysis of pebble bed reactors during earthquake by discrete element method. Nucl. Eng. Des. 2013, 258, p. 102–106, <https://doi.org/10.1016/j.nucengdes.2013.01.028>.
- Keppler, I., Safranyik, F., Oldal, I. (2016): Shear test as calibration experiment for DEM simulations: a sensitivity study. Eng. Comput. 2016, 33, <https://doi.org/10.1108/ec-03-2015-0056>.
- Ketterhagen, W.R., Curtis, J.S., Wassgren, C.R., Kong, A., Narayan, P.J., Hancock, B.C. (2007): Granular segregation in discharging cylindrical hoppers: A discrete element and experimental study. Chem. Eng. Sci. 2007, 62, p. 6423–6439, <https://doi.org/10.1016/j.ces.2007.07.052>.
- Kiss, K. (2015): Nem hagyományos szénhidrogének kutatása. Hazai lehetőségek, jelenlegi, valamint várható eredmények, gyakorlati tapasztalatok a MOL Nyrt. érdekeltségű kutatási és termelési területeken. (Unconventional hydrocarbon exploration. Domestic opportunities, actual and expected results, working experiences on the exploration and mining plots of MOL Plc). Magyar Tudomány 176, (11): p. 1304–1313.
- Lacy, L.L., Rickards, A.R., Ali, S.A. (1997): Embedment and Fracture Conductivity in Soft Formations Associated with HEC, Borate and Water-Based Fracture Designs. Soc. Pet. Eng., <https://doi.org/10.2118/38590-ms>.
- Lacy, L.L., Rickards, A.R., Bilden, D. (1998): Fracture Width and Embedment Testing in Soft Reservoir Sandstone. SPE Drill. Complet., 13, p. 25–29, <https://doi.org/10.2118/36421-pa>.
- Lehman, L.V., Parker, M.A., Blauch, M.E., Haynes, R., Blackmon, A. (1999): Proppant Conductivity—What Counts and Why. Soc. Pet. Eng., <https://doi.org/10.2118/52219-ms>.
- Li, K., Gao, Y., Lyu, Y., Wang, M. (2015): New Mathematical Models for Calculating Proppant Embedment and Fracture Conductivity. SPE J., 20, p. 496–507, <https://doi.org/10.2118/155954-pa>.
- Liang, F., Sayed, M., Al-Muntasheri, G., Chang, F.F. (2015): Overview of Existing Proppant Technologies and Challenges. Soc. Pet. Eng., <https://doi.org/10.2118/172763-ms>.
- Liang, F., Sayed, M., Al-Muntasheri, G.A., Chang, F.F., Li, L. (2015): A comprehensive review on proppant technologies. Petroleum 2015, 2, p.v26–39, <https://doi.org/10.1016/j.petlm.2015.11.001>.

- Malkowski, P., Ostrowski, L. (2017): The Methodology for the Young Modulus Derivation for Rocks and Its Value. In Proceedings of the ISRM European Rock Mechanics Symposium-EUROCK 2017, Ostrava, Czech Republic, June 20-22, 2017.
- McCain, W. D. (1991): Reservoir-Fluid Property Correlations-State of the Art (includes associated papers 23583 and 23594). SPE Res. Eng. 6: p. 266–272. doi: <https://doi.org/10.2118/18571-PA>
- McDaniel, G.A., Abbott, J., Mueller, F.A., Mokhtar, A., Pavlova, S., Neuvonen, O., Parias, T., Alary, J.A. (2010): Changing the Shape of Fracturing: New Proppant Improves Fracture Conductivity. Soc. Pet. Eng., <https://doi.org/10.2118/135360-ms>.
- Gillard M., Medvedev O., Peña A., Medvedev A., Peñacorada F., d’Huteau E. (2010): A new approach to generating fracture conductivity, in SPE Annual Technical Conference and Exhibition, Florence, Italy, September 2010.
- Milton-Taylor, D., Stephenson, C., Asgian, M. (1992): Factors Affecting the Stability of Proppant in Propped Fractures: Results of a Laboratory Study. Soc. Pet. Eng., <https://doi.org/10.2118/24821-ms>.
- Mittal, A., Rai, C. S., Sondergeld C. H. (2018): Proppant-Conductivity Testing Under Simulated Reservoir Conditions: Impact of Crushing, Embedment, and Diagenesis on Long-Term Production in Shales. SPE J. 23, 2018, p. 1304–1315. doi: <https://doi.org/10.2118/191124-PA>
- Moharos, I., Oldal, I., Szekrényes, A. (2011): Végeselem-Módszer, Egyetemi tananyag, Typotex, 2011. ISBN 978-963-279-539-3
- Naylor, T. H., Finger, J. M. (1967): Verification of computer simulation models. Management Science 14(2): B92–B101. doi:10.1287/mnsc.14.2.b92
- Nádor, A., Kovács, Zs., Cserkész-Nagy, Á., Bereczki, L., Markos, G., Fancsik, T., Kovács, A., Szocs, T. (2016): Study of Some Potential Environmental Impacts of Hydraulic Fracturing Related to Unconventional Hydrocarbons in Hungary. DOI: 10.1007/698_2016_9.
- Oldal, I., Keppler, I., Csizmadia, B., Fenyvesi, L. (2012): Outflow properties of silos: The effect of arching. Advanced Powder Technology. 23, (3) p. 290-297. <https://doi.org/10.1016/j.appt.2011.03.013>.
- Oldal I., Safranyik F. (2015): Extension of silo discharge model based on discrete element method, Journal of Mechanical Science and Technology, 29 (9) p. 3789-3796.
- Palisch, T.T., Duenckel, R.J., Bazan, L.W., Heidt, J.H., Turk, G.A. (2007): Determining Realistic Fracture Conductivity and Understanding its Impact on Well Performance-Theory and Field Examples. In Proceedings of the SPE Hydraulic Fracturing Technology Conference, College Station, TX, USA, January 29-31, <https://doi.org/10.2118/106301-ms>.

- Park, J., Kang, N. (2009): Applications of fiber models based on discrete element method to string vibration. *J. Mech. Sci. Technol.* 2009, 23, p. 372–380, <https://doi.org/10.1007/s12206-008-0921-8>.
- Peard, N., Macaluso, M., Griffin, M., Address, R., Callanan, M. (1991): Improved Fracturing Techniques Increase Productivity in the AWP (Olmos) Field. *Soc. Pet. Eng.* <https://doi.org/10.2118/21646-ms>.
- Penny, G. S. (1987): An Evaluation of the Effects of Environmental Conditions and Fracturing Fluids Upon the Long-Term Conductivity of Proppants. Paper presented at the SPE Annual Technical Conference and Exhibition, Dallas, Texas. 1987. doi: 10.2118/16900-MS.
- Perkins, T.K., Kern, L.R. (1961): Widths of Hydraulic Fractures. *J. Pet. Technol.*, 13, p. 937–949, <https://doi.org/10.2118/89-pa>.
- Pusztai, P., Koroncz, J. P. (2021): Modified Approach for proppant conductivity measurement, *Geosciences and Engineering*, a Publication of the University of Miskolc, Miskolc University Press. HU ISSN 2063-6997.
- Raji, A.O., Favier, J.F. (2004): Model for deformation in agricultural and food particular materials under bulk compressive loading using discrete element method, Theory, model development and validation, *Journal of Agricultural Engineering Research*, Vol. 60, p. 359-371.
- Renkes, I., Anschutz, D., Sutter, K., Rickards, A. (2017): Long Term Conductivity vs. Point Specific Conductivity. Proceedings of the SPE Hydraulic Fracturing Technology Conference and Exhibition, The Woodlands, TX, USA, January 24-26, 2017, <https://doi.org/10.2118/184814-ms>.
- Richard, S., Schrader, S., Schrader, R., Ereaux, B. (2019): Improved Methods of Measuring Proppant Conductivity. Paper presented at the SPE Western Regional Meeting, San Jose, California, USA, 2019, Society of Petroleum Engineers, SPE-195368-MS, doi: 10.2118/195368-MS
- Robertson, E.P., Christiansen, R. L. (2007): Modeling laboratory permeability in coal using of sorption-induced strain data, *SPE Reservoir Evaluation & Engineering*, SPE 97068, v. 10/3, p. 260-269.
- Roodhart, L., Kulper, T., Davies, D.R.K. (1988): Proppant-Pack and Formation Impairment during Gas-Well Hydraulic Fracturing. *SPE Prod. Eng.*, 3, p. 438–444, <https://doi.org/10.2118/15629-pa>.
- Sargent, R. (2013): Verification and validation of simulation models. *J Simulation* 7, p. 12–24. <https://doi.org/10.1057/jos.2012.20>.
- Schlumberger, (2021). HiWAY flow-channel fracturing technique (slb.com) [Online] Available at: <https://www.slb.com/-/media/files/stimulation/product-sheet/hiway-transition-technologies-ps-1.ashx>, [Accessed 28. 10. 2021.].

- Šmilauer, V., Chareyre, B. (2010): Yade dem formulation. In Yade Documentation, 1st ed. Šmilauer, V., Ed., The Yade Project: 2010. <http://yade-dem.org/doc/formulation.html>.
- Sun, J., Hu, K., Wong, J., Hall, B., Schechter, D. (2014): Investigating the Effect of Improved Fracture Conductivity on Production Performance of Hydraulic Fractured Wells through Field Case Studies and Numerical Simulations. *Soc. Pet. Eng.*, <https://doi.org/10.2118/169866-ms>.
- Terracina, J.M., Harper, A.K. Hexion Inc., (2021). Altering the surface chemistry of resin-coated proppant delivers improved oil flow rates in the Eagle Ford Shale. Improving Well Economics With Advanced Proppants, Hart Energy, [Online] Available at: <https://www.hartenergy.com/exclusives/improving-well-economics-advanced-proppants-176870>, [Accessed 28. 10. 2021.].
- Turner, M.J., Clough, R.W., Martin, H.C., Topp, L.J. (1956): Stiffness and Deflection Analysis of Complex Structures. *J. Aeronaut. Sci.*, 23, p. 805–823, <https://doi.org/10.2514/8.3664>.
- Varga, A., Lengyel, T., Safranyik, F. (2020): Determination of micromechanical parameters of proppant particles. *IJIRAE Int. J. Res. Adv. Eng.*, VII, p. 15–21.
- Varga, A. (2018): Szabad keverőcsigák környezetében létrejövő szemcsemozgások elemzése, PhD Értekezés, Gödöllő.
- Volk, L.J., Raible, C.J., Carroll, H.B., Spears, J.S. (1981): Embedment of High Strength Proppant into Low-Permeability Reservoir Rock. *Soc. Pet. Eng.*, <https://doi.org/10.2118/9867-ms>.
- Weaver, J.D., Rickman, R.D., Luo, H. (2008): Fracture-Conductivity Loss Due to Geochemical Interactions between Manmade Proppants and Formations. *Soc. Pet. Eng.*, <https://doi.org/10.2118/118174-ms>.
- Wu, J.K., Wang, M.Z., Wang, W. (2001): Elastic Mechanics Introduction. Recension of first edition (Peking University Press. Beijing, Chinese, 2001) p. 200-203
- Yuan, C., Zongquan, D., Bing, L. (2011): Numerical simulations of motion behaviors of pan mechanism in a cooking robot with granular cuisine, *Journal of Mechanical Science and Technology*, Vol. 25 (3), p. 803-808.
- Zhang, F., Dontsov, E. (2018): Modeling hydraulic fracture propagation and proppant transport in a two-layer formation with stress drop. *Eng. Fract. Mech.*, 199, p. 705–720, <https://doi.org/10.1016/j.engfracmech.2018.07.008>.
- Zhang, F., Zhu, H., Zhou, H., Guo, J., Huang, B. (2017): Discrete-Element-Method/Computational-Fluid-Dynamics Coupling Simulation of Proppant Embedment and Fracture Conductivity After Hydraulic Fracturing. *SPE J.* 2017, 22, p. 632–644, <https://doi.org/10.2118/185172-pa>.
- Zhel'tov, A.K. (1955): Formation of Vertical Fractures by Means of Highly Viscous Liquid. In *Proceedings of the 4th World Petroleum Congress, Rome, Italy, 3 June 1955*.

Zhu, H., Shen, J., Zhang, F. (2018): A fracture conductivity model for channel fracturing and its implementation with Discrete Element Method. *J. Pet. Sci. Eng.*, 172, p. 149–161, <https://doi.org/10.1016/j.petrol.2018.09.054>.

10.APPENDICES

10.1. HiWay channel fracturing

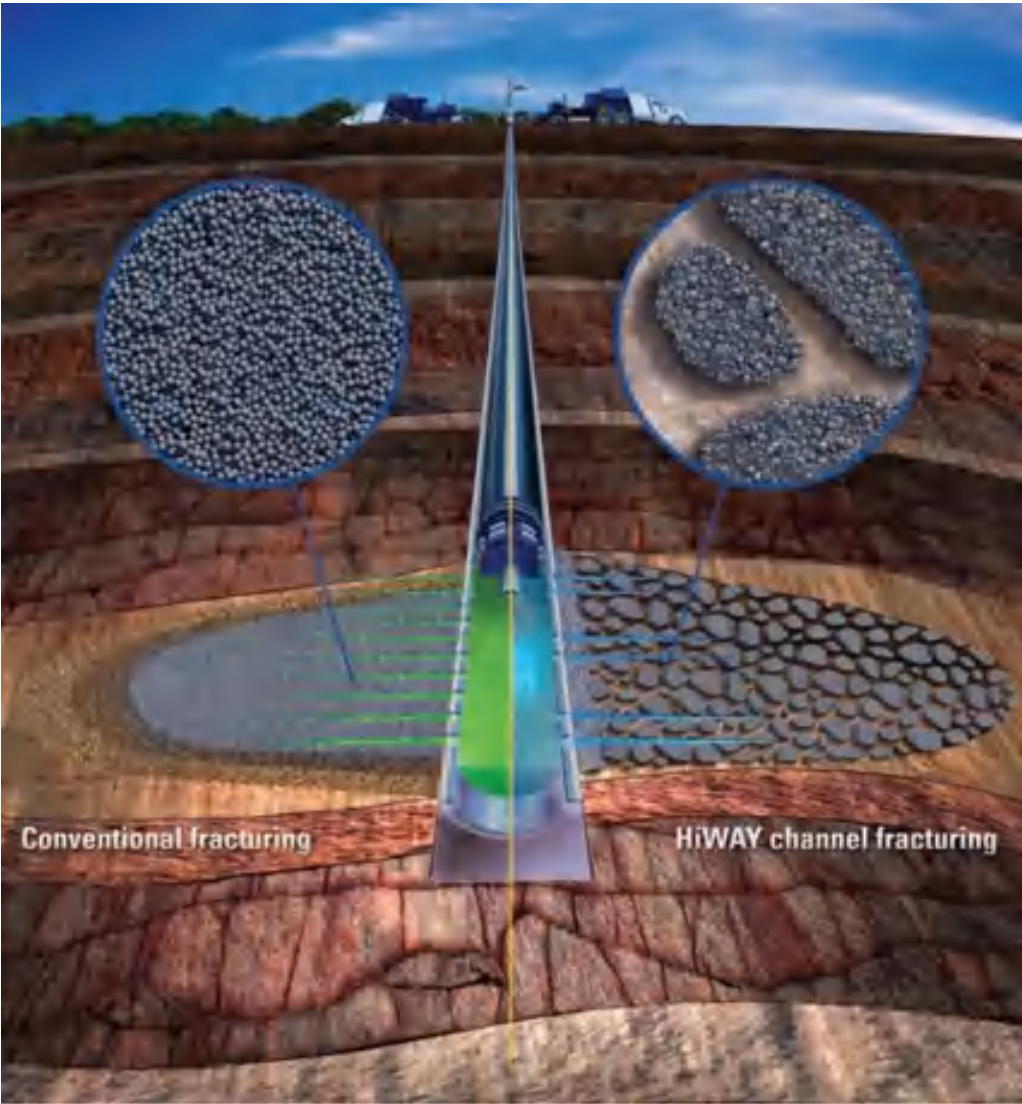


Fig. I Channel Fracturing (Gillard et al., 2010)

10.2. Mesh independence analysis

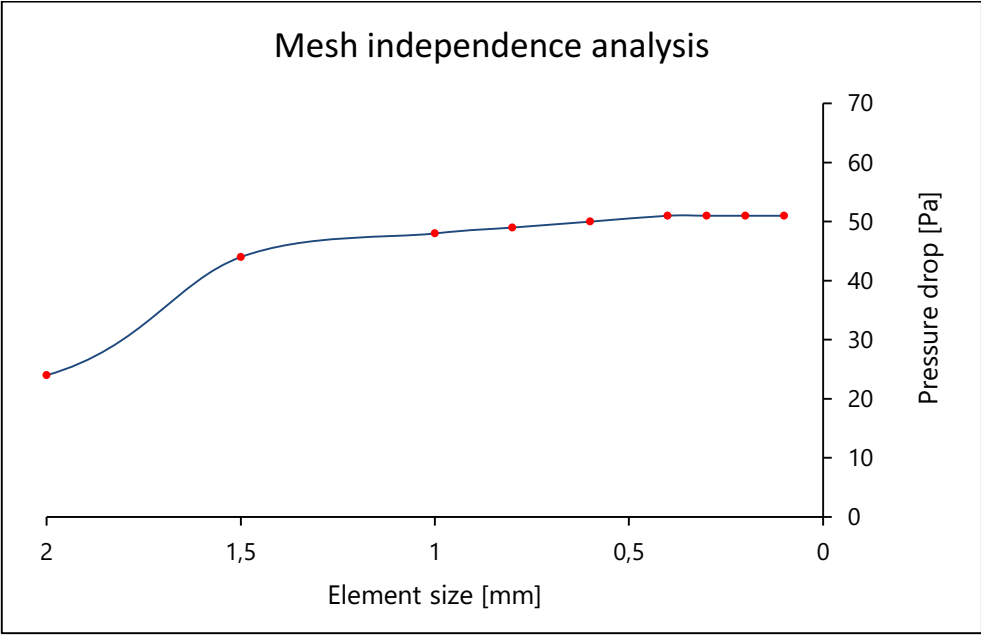


Fig. II Mesh independence study with element size (edited by the Author)

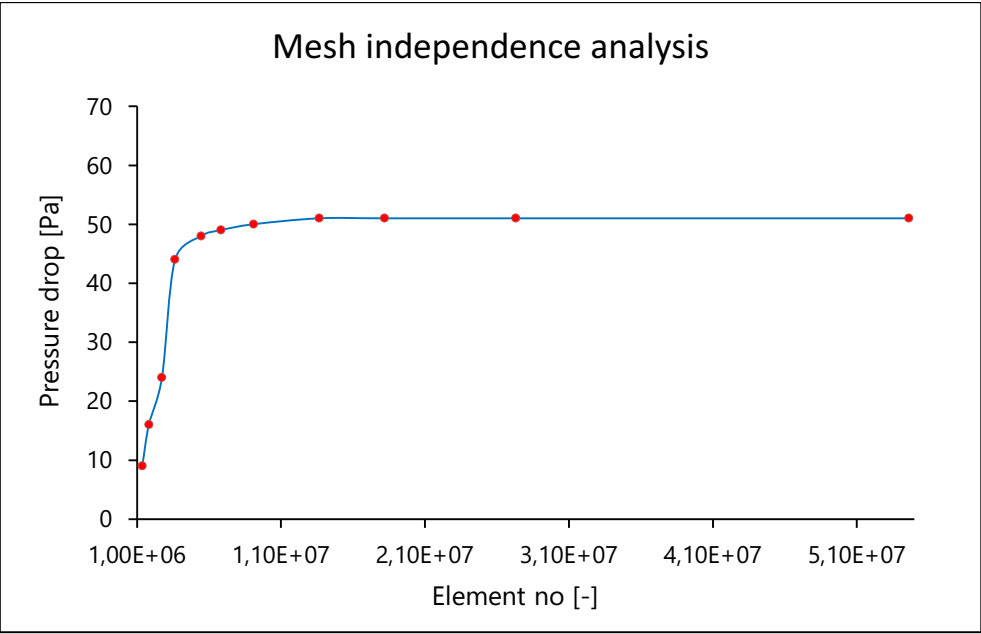


Fig. III Mesh independence study with element number (edited by the Author)

10.3. Technical data sheet

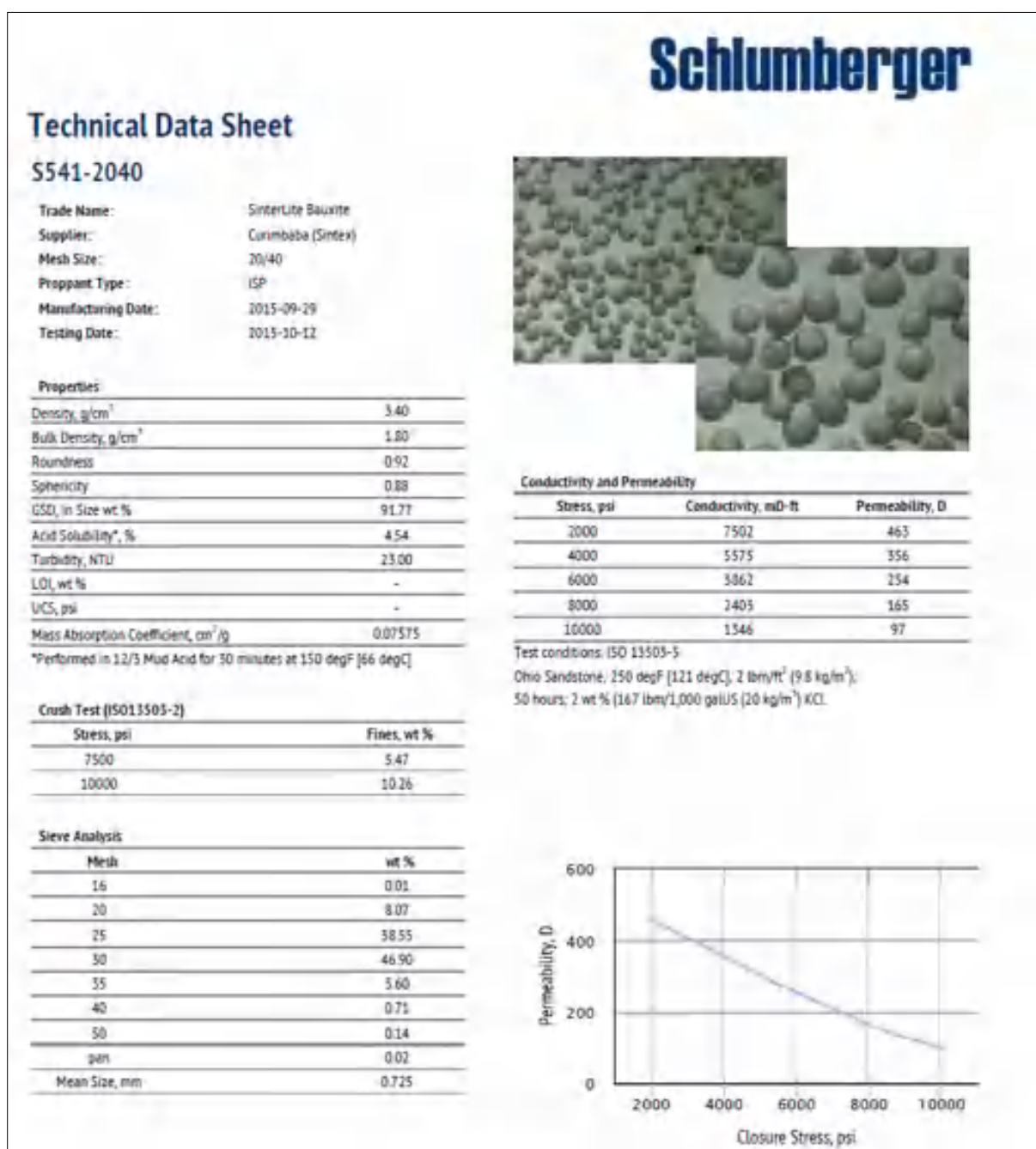


Fig. IV SinterLite Bauxit 20/40 (Schlumberger TDS)

Technical Data Sheet

S360-1630

Trade Name: MaxPROP ISP G2
 Supplier: Santrol
 Mesh Size: 16/30
 Proppant Type: IS-RCP-C
 Manufacturing Date: 2015-10-22
 Testing Date: 2015-11-15

Properties

Density, g/cm ³	2.96
Bulk Density, g/cm ³	1.80
Roundness	0.90
Sphericity	0.89
GSD, In Size wt %	98.99
Acid Solubility*, %	1.36
Turbidity, NTU	6.10
LOI, wt %	3.63
UKS, psi	428.79
Mass Absorption Coefficient, cm ² /g	0.07575

*Performed in 12/5 Mud Acid for 30 minutes at 150 degF (66 degC)

Crush Test (ISO15503-2)

Stress, psi	Fines, wt %
10000	3.13
12500	7.93

Sieve Analysis

Mesh	wt %
12	0.04
16	0.95
18	55.86
20	31.42
25	10.64
30	1.07
40	0.07
pan	0.00
Mean Size, mm	1.004



Conductivity and Permeability

Stress, psi	Conductivity, mD-ft	Permeability, D
2000	9613	580
4000	8681	529
6000	7473	460
8000	5454	343
10000	3634	237

Test conditions: ISO 15503-5

Ohio Sandstone; 250 degF [121 degC]; 2 lbm/ft³ (9.8 kg/m³);

50 hours; 2 wt % (167 lbm/1,000 gallons (20 kg/m³) KCl

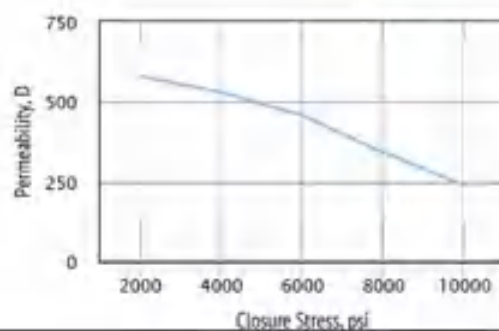


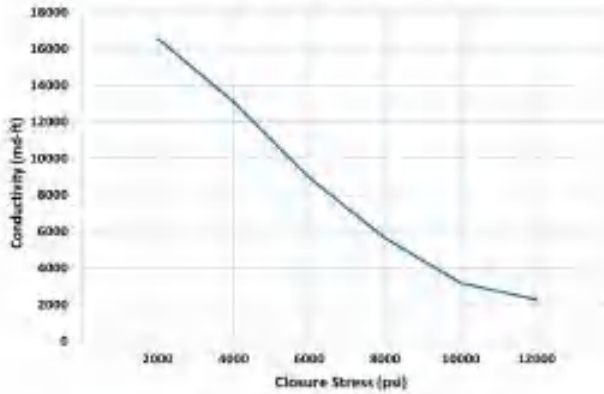
Fig. V MaxPROP 16/30 (Schlumberger TDS)

InterProp 16/30

Intermediate Strength Proppants

Technical Data Sheet

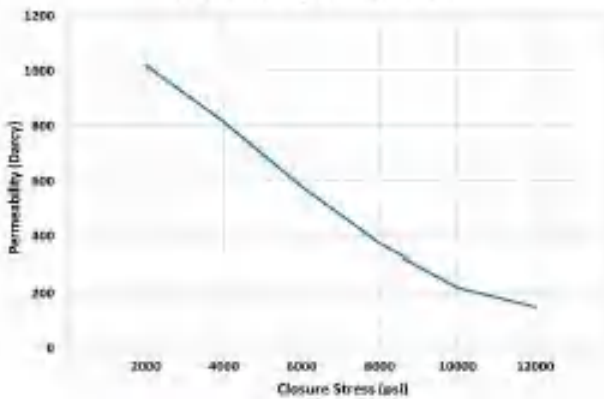
2 lb/ft³, 250°F, 2% KCl & Ohio Sandstone



Reference Conductivity (md-ft), 250°F

Closure Stress (psi)	16/30, 2 lb/ft ³
2,000	16560
4,000	13100
6,000	8950
8,000	5630
10,000	3150
12,000	2260

2 lb/ft³, 250°F, 2% KCl & Ohio Sandstone



Reference Permeability (Darcies), 250°F

Closure Stress (psi)	16/30, 2 lb/ft ³
2,000	1020
4,000	815
6,000	580
8,000	375
10,000	220
12,000	150

Physical Properties:

Specific Gravity	3.2
Bulk Density	1.88 g/cc (117 lb/ft ³)
Absolute Volume	0.0374 gal/lb
Acid Solubility, %	2.3
Roundness/Sphericity (Krumbein & Sloss)	0.9/0.9


Crush Resistance, %	7,500 psi	2.2
	10,000 psi	4.4
	12,500 psi	7.6
Median Particle Dia.	0.93 mm	

SAINT-GOBAIN

Fig. VI InterProp 16/30 (Saint-Gobain TDS)

CARBOECONOPROP

Low-density ceramic proppant

<p>Features</p> <ul style="list-style-type: none"> • Bulk density and specific gravity similar to frac sand • Chemically inert • Available in three standard sizes—20/40, 30/50 and 40/70 	<p>Benefits</p> <ul style="list-style-type: none"> • Developed for largest well concentration • Cost-effective alternative for resin-coated sand • Will not react with fracturing fluid crosslinkers and breakers • High conductivity for increased production 	
---	---	---

Ideally suited for moderate-depth natural gas wells

Both the bulk density and specific gravity of CARBOECONOPROP®, a low-density ceramic proppant, are similar to frac sand, yet its high conductivity makes it more cost-effective than resin-coated sand proppant. CARBOECONOPROP is non-reactive to fracturing fluid crosslinkers and breakers.

Long-term conductivity

Reference conductivity, md-ft @ 250°F

Closure stress [psi]	2 lb/ft ³ 20/40	2 lb/ft ³ 30/50	2 lb/ft ³ 40/70
2,000	6,300	4,150	2,200
4,000	5,500	3,500	1,600
6,000	4,700	2,850	1,200
8,000	4,000	2,400	900
10,000	3,300	1,950	650

Reference permeability, Darcies @ 250°F

Closure stress [psi]	2 lb/ft ³ 20/40	2 lb/ft ³ 30/50	2 lb/ft ³ 40/70
2,000	340	220	115
4,000	300	180	100
6,000	260	160	90
8,000	230	140	80
10,000	200	120	70

Reference conductivity and permeability are measured with a single phase fluid under laminar flow conditions in accordance with API RP 80D. In an actual fracture, the effective conductivity will be much lower due to non-Darcy and multiphase flow effects. For more information, please refer to SPE Paper #106301 – "Determining Realistic Fracture Conductivity and Understanding its Impact on Well Performance—Theory and Field Examples."

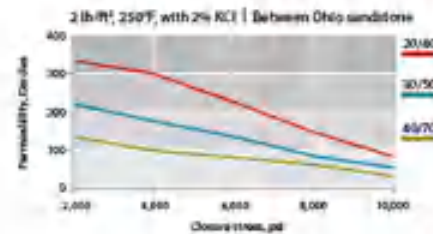
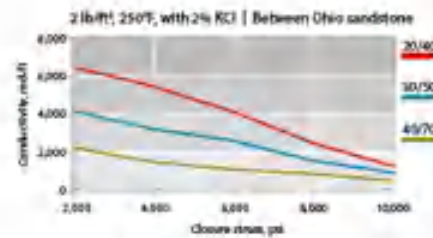


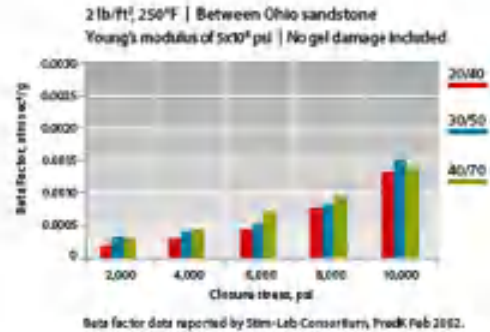
Fig. VII Carboeconoprop 30/50 Page 1 (CARBO TDS)

CARBOECONOPROP

Low-density ceramic proppant

Beta factors

Closure stress [psi]	Beta factor [dm ³ sec ⁻¹ g ⁻¹]		
	20/40	30/50	40/70
2,000	0.00024	0.00035	0.00034
4,000	0.00029	0.00040	0.00046
6,000	0.00045	0.00050	0.00070
8,000	0.00075	0.00080	0.00092
10,000	0.00129	0.00150	0.00151



Physical and chemical properties

Typical sieve analysis [weight % retained]

U.S. Mesh [mesh]	Microns	20/40	30/50	40/70
-16+20 mesh	-1180+850	5		
-20+30 mesh	-850+600	68	3	
-30+40 mesh	-600+425	35	79	5
-40+50 mesh	-425+300		17	72
-50+70 mesh	-300+212		7	22
-70 mesh	-212			1
Median particle diameter [microns]		635	475	332
API/ISO crush test	@ 5,000 psi	1.0	6.8	0.4
% by weight fines generated	@ 7,500 psi	5.2	2.8	2.0

Sizing requirements: A minimum of 90% of the tested sample should fall between the designated sieve sizes. These specifications meet the recommended practices as detailed in API RP 19C.

Typical additional properties

Roundness	0.9	Apparent specific gravity	2.70
Sphericity	0.9	Absolute volume [gal/lb]	0.044
Bulk density [lb/ft ³]	96	Solubility in 12.5 HCl/HF acid	1.7
[g/cm ³]	1.56	[% weight loss]	

All data represents typical values.

Talk to CARBO to find out how we can help you enhance your production.
carboceramics.com

CARBO
Production. Enhanced.

© 2012 CARBO Ceramics, Inc. All rights reserved. 14-CL-001

Fig. VIII Carboeconoprop 30/50 Page 2 (CARBO TDS)

10.4. Conductivity measurement

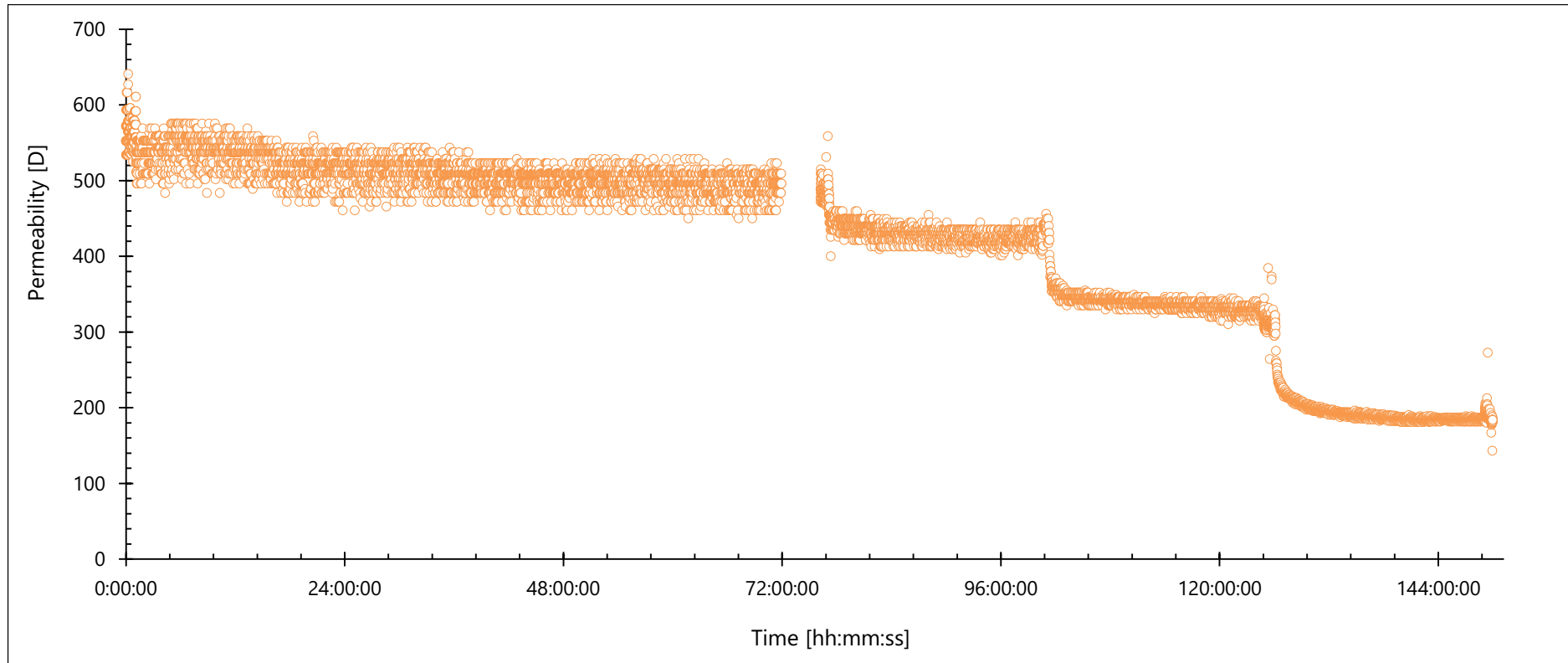


Fig. IX Conductivity measurement (edited by the Author)

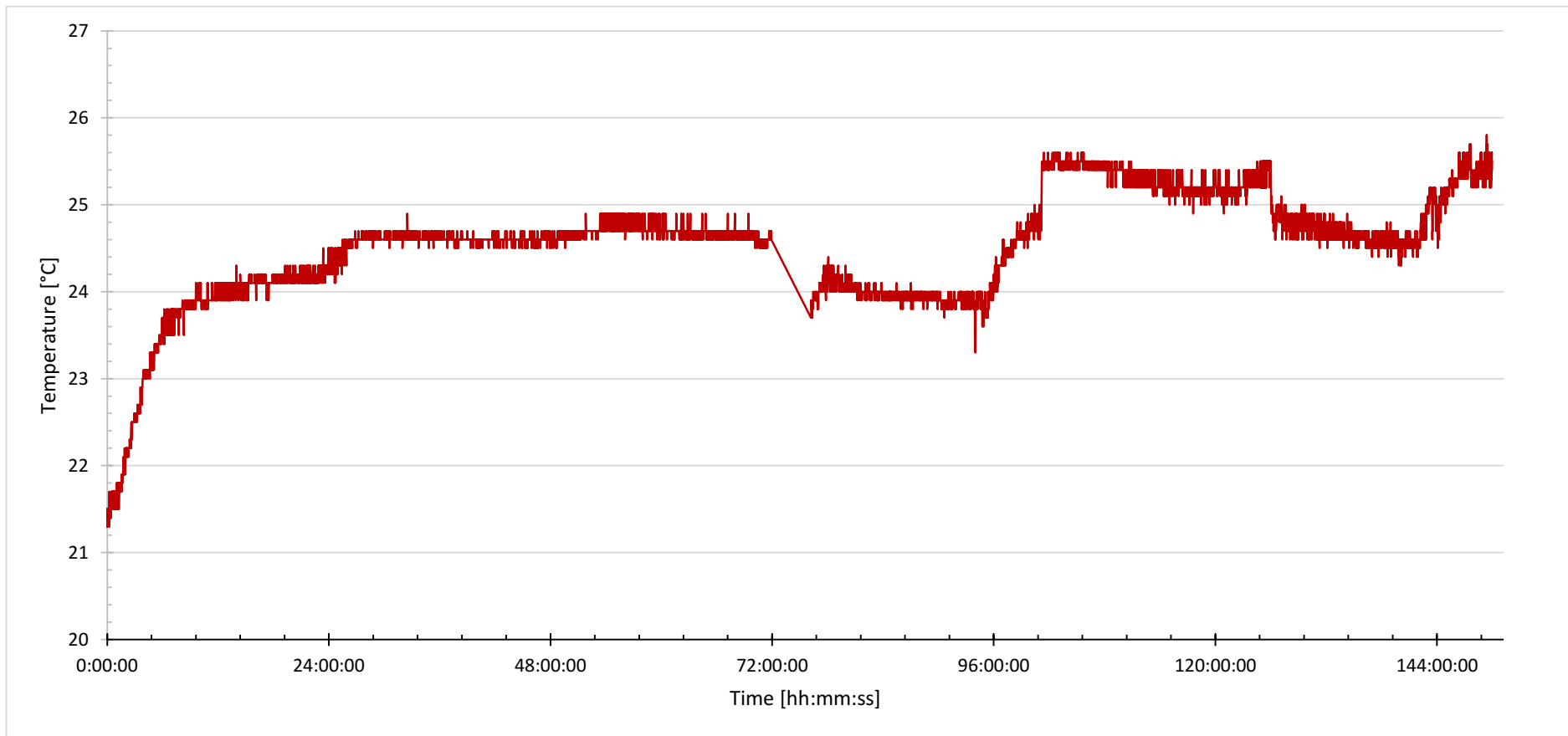


Fig. X Temperature during conductivity measurement (edited by the Author)

10.5. DEM source code with size distribution

```
##### Modules, establishment of functions #####
from yade import plot
from yade import pack
from yade import qt
from yade import ymport
from scipy.integrate import odeint
from datetime import datetime
import math
import numpy as np
import sys
#from os import chdir
#chdir('/home/feri/pythonScript/snowStorm')
qt.View() #3D viewer
#qt._GLViewer.Renderer(ghosts=False)
#import sys
#sys.path.append('/home/szie/PythonScript/Kalibracio') #path
#from par_sugar import par_sugar #parameters from external file
```

```
*****Parameter definition*****
```

```
#utils.readParamsFromTable(sugar=0.005)
```

```
#from yade.params.table import *
```

```
#from yade.params import table
```

```
start_time = datetime.now().strftime("%d-%m-%Y %H:%M:%S")
```

```
*****Material definition*****
```

```
#rock
```

```
dens = 2670
```

```
E = 1.5e10
```

```
nu = .3
```

```
frictAng = .1 #friction coeff approx. .1
```

```
eRoll = .001
```

```
sCoh = 1e10
```

```
nCoh = 1e10
```

```
#proppant
```

```
densP = 2800
```


EP = 4.1306e10

nuP = .25

frictAngP = .05 #friction coeff approx. .1

eRollP = .001

sCohP = 0

nCohP = 0

tensP = 10e6

cohP = 10e6

#wall

EA = 2.1e8

nuA = .3

densA = 7800

frictAngA = .1 #friction coeff approx. .1

#rock

```
#rock = O.materials.append(CohFrictMat(young=E,poisson=nu,density=dens,frictionAngle=frictAng,normalCohesion=nCoh,  
                                     #shearCohesion=sCoh,etaRoll=eRoll,isCohesive=True,momentRotationLaw=True,label='rock'))
```

#wall

```
#wall = O.materials.append(CohFrictMat(young=EA,poisson=nuA,density=densA,frictionAngle=frictAngA,normalCohesion=0,  
                                     #shearCohesion=0,etaRoll=eRoll,isCohesive=False,momentRotationLaw=False,label='wall'))
```

```
wall = O.materials.append(JCFpmMat(type=0,density=dens,young=E,poisson=nu,frictionAngle=frictAng,label='wall'))
```

```
#proppant
```

```
#prop = O.materials.append(CohFrictMat(young=EP,poisson=nuP,density=densP,frictionAngle=frictAngP,normalCohesion=nCohP,  
#shearCohesion=sCohP,etaRoll=eRoll,isCohesive=False,momentRotationLaw=False,label='prop'))
```

```
prop
```

```
O.materials.append(JCFpmMat(type=1,density=densP,young=EP,poisson=nuP,tensileStrength=tensP,cohesion=cohP,frictionAngle=frictAngP,label='prop'))
```

```
*****Wall definition*****
```

```
length = .002
```

```
width = .03
```

```
height = .02
```

```
#frac = O.bodies.append(yimport.gmsh('ZSEB.mesh',fixed=True,material='wall',shift=(0,0,0),scale=1,wire=True,color=(.5,0,.5)))yimport.stl
```

```
frac = O.bodies.append(yimport.stl('frac20_mm.stl',fixed=True,material='wall',wire=True,color=(.0,0,.5)))
```

```
#frac = O.bodies.append(yimport.stl('ZSEB3.stl',fixed=True,material='wall',wire=True,color=(.5,0,.5)))
```

```

propL = length/10
propW = width
propH = height/2
radiusR1 = .0005950 #1190
radiusR2 = .0005000 #1000
radiusR3 = .000840 #841
sp = pack.SpherePack()
coeff = .9 #coefficient for smaller dimensions of the predicate

sp.makeCloud((-length*coeff,-width*coeff,.12-height*coeff),(length*coeff,width*coeff,.12+height*coeff),rMean=radiusR1,rRelFuzz=0,num=3185)
sp.makeCloud((-length*coeff,-width*coeff,.12-height*coeff),(length*coeff,width*coeff,.12+height*coeff),rMean=radiusR2,rRelFuzz=0,num=175)
sp.makeCloud((-length*coeff,-width*coeff,.12-height*coeff),(length*coeff,width*coeff,.12+height*coeff),rMean=radiusR3,rRelFuzz=0,num=140)

m = sp.toSimulation(material='prop')
for i in m:
O.bodies[i].shape.color = (.5,.5,0.)

#*****Definition of simulation cycle*****

damp = .4

```

```

factor = 1.00
O.engines=[
ForceResetter(),
InsertionSortCollider([Bo1_Sphere_Aabb(aabbEnlargeFactor=factor),Bo1_Facet_Aabb()]),
InteractionLoop(
  [Ig2_Sphere_Sphere_ScGeom(interactionDetectionFactor=factor),Ig2_Facet_Sphere_ScGeom()],
  [Ip2_JCFpmMat_JCFpmMat_JCFpmPhys(cohesiveTresholdIteration=1,label='JCFpm')],
  [Law2_ScGeom_JCFpmPhys_JointedCohesiveFrictionalPM(recordCracks=False)]
),
NewtonIntegrator(damping=damp,gravity=(0,0,-9.81),label='newton'),
#VTKRecorder(iterPeriod=1000,recorders=['spheres','facets','materialId','velocity'],fileName='/home/feri/pythonScript/MOL/video/MOL_v1')
#VTKRecorder(iterPeriod=10000,recorders=['spheres','facets','materialId'],fileName='/home/feri/pythonScript/snowStorm/video/snowStorm03e')
#VTKRecorder(REC_ID=budoge,iterPeriod=1000,mask=2,recorders=['facets'],fileName='/home/feri/pythonScript/snowStorm/video/snowStorm03b'),
#VTKRecorder(iterPeriod=1000,mask=3,recorders=['facets'],fileName='/home/feri/pythonScript/snowStorm/video/snowStorm03c'),
#VTKRecorder(iterPeriod=1000,mask=4,recorders=['facets'],fileName='/home/feri/pythonScript/snowStorm/video/snowStorm03d'),
#VTKRecorder(iterPeriod=10,recorders=['facets','materialId'],fileName='/home/feri/pythonScript/snowStorm/video/snowStormFacetUnsymm')
]
O.dt=.7*utils.PWaveTimeStep() #Timestep

```

```
*****Functions*****
```

```
def ment():
```

```
plot.addData(i=O.iter,uF=utils.unbalancedForce())
```

```
if O.iter > 40000 and utils.unbalancedForce() < .05:
```

```
global heightP
```

```
heightP = max([b.state.pos[2] + b.shape.radius for b in O.bodies if isinstance(b.shape,Sphere)]) #height of topmost sphere + R
```

```
print('height = ' + str(heightP))
```

```
#if O.bodies[frac[0]].state.pos[2] > .5:
```

```
global frac
```

```
global packingPlate
```

```
packingPlate = O.bodies.append(geom.facetBox((.0,.0,heightP+.105),(length,width,.1),wallMask=16, material='wall'))
```

```
frac = O.bodies.append(ympart.gmsh('ZSEB.mesh',fixed=True,material='wall',shift=(0,0,-.1+heightP*.7),scale=1,wire=True,color=(0,0,0)))
```

```
vel = .8
```

```
O.engines = O.engines + [TranslationEngine(ids=frac,translationAxis=(0,0,-1),velocity=vel)]
```

```
O.engines = O.engines + [TranslationEngine(ids=packingPlate,translationAxis=(0,0,-1),velocity=vel*1.5)]
```

```
vez.command='ell()'
```

```
#O.pause()#O.engines = O.engines + [TranslationEngine(ids=frac,translationAxis=(0,0,-1),velocity=.2)]
```

```
def ell():
```

```

plot.addData(i=O.iter,uF=utils.unbalancedForce())
if O.bodies[packingPlate[0]].state.pos[2] < heightP * 3:
    O.engines = O.engines + [TranslationEngine(ids=packingPlate,translationAxis=(0,0,-1),velocity=0)]
if O.bodies[frac[0]].state.pos[2] < heightP * 8:
    O.engines = O.engines + [TranslationEngine(ids=frac,translationAxis=(0,0,-1),velocity=.0)]
coh.setCohesionNow=True
for b in frac:
    O.bodies.erase(b)
for b in packingPlate:
    O.bodies.erase(b)
radiusP = 0.0025
sp2 = pack.SpherePack()
#coeff2 = .5 #coefficient for smaller dimensions of the predicate
sp2.makeCloud((-0.0075,-.045,heightP),(0.0075,.045,1.2*heightP),rMean=radiusP,rRelFuzz=0.)
#sp2.makeCloud((-propL*coeff2,-propW*coeff2*1.8,.8-
propH*coeff2),(propL*coeff2,propW*coeff2*1.8,.8+propH*coeff2),rMean=radiusP,rRelFuzz=0.)
n = sp2.toSimulation(material='prop')
for i in n:
    O.bodies[i].shape.color = (0,..5,0.)
#for b in container:

```

```

# O.bodies.erase(b)
#O.pause()
vez.dead=True

def sulypMent(time):
fileName = 'sulyp' + str(time) + '.txt'
sulyp = open(fileName,'w')
sulyp.write('mm\n')
sulyp.write('ID,x,y,z\n')
for b in O.bodies:
if isinstance(b.shape,Sphere):
    Sx = b.state.pos[0]*1000
    Sy = b.state.pos[1]*1000
    Sz = b.state.pos[2]*1000
    ID = b.id
    s = b.shape
    p = b.state.pos
    print("{}: x={}, y={}, z={}, r={}".format(b.id, p[0], p[1], p[2], s.radius))
sulyp.close
def felsoSzem():

```

```

felszin = []
for b in O.bodies:
    if isinstance(b.shape,Sphere):
        print ('#####')
        sulypZ = b.state.pos[2]
        print (sulypZ)
        contPoint = []
        for i in O.bodies[b.id].intrs():
            if isinstance(O.bodies[i.id1].shape,Sphere) and isinstance(O.bodies[i.id2].shape,Sphere):
                contPoint.append(i.geom.contactPoint[2])
        print (contPoint)
        teszt = 0
        for i in contPoint:
            if i > sulypZ:
                teszt += 1
        if teszt == 0:
            felszin.append(b.id)
print (felszin)
plot.plots = {'i':'uF'}
plot.plot()

```


10.6. DEM Source code for validation

```
#####Modules, establishment of functions#####

from yade import plot                #Activate plot module
from yade import pack                #The module generates particles in a virtual reservoir
from yade import qt                  #Import of 3D display module
from yade import ymport
from scipy.integrate import odeint
from datetime import datetime
import math
import numpy as np
import sys

qt.View()                            #3D viewer

start_time = datetime.now().strftime("%d-%m-%Y %H:%M:%S")
```

*****Material definition*****

#rock

dens = 2670

E = 1.5e10

nu = .3

frictAng = .1 #friction coeff approx. .1

eRoll = .001

sCoh = 1e10

nCoh = 1e10

#proppant

densP = 2800

EP = 4.1306e10

nuP = .25

frictAngP = .05 #friction coeff approx. .1

eRollP = .001

sCohP = 0

nCohP = 0

tensP = 10e6

cohP = 10e6

#wall

EA = 2.1e8

nuA = .3

densA = 7800

frictAngA = .1 #friction coeff approx. .1

wall = O.materials.append(JCFpmMat(type=0,density=dens,young=E,poisson=nu,frictionAngle=frictAng,label='wall'))

prop

O.materials.append(JCFpmMat(type=1,density=densP,young=EP,poisson=nuP,tensileStrength=tensP,cohesion=cohP,frictionAngle=frictAngP,label='prop'))

*****Wall definition*****

length = .155

width = .03

height = .06

```

meroCella = O.bodies.append(ymport.stl('meroCellaMultipleSurface_m.stl',fixed=True,material='wall',wire=True,color=(.5,0,.5)))

propL = length/20
propW = width
propH = height/2

radiusR = .00055
sp = pack.SpherePack()
coeff = .5 #coefficient for smaller dimensions of the predicate
sp.makeCloud((-length*coeff,-width*coeff,.07-height*coeff),(length*coeff,width*coeff,.07+height*coeff),rMean=radiusR,rRelFuzz=0.,num=40000)
m = sp.toSimulation(material='prop')

for i in m:
O.bodies[i].shape.color = (.5,.5,0.)

#*****Define simulation cycle*****

damp = .4

```

```

factor = 1.00
O.engines=[
    ForceResetter(),
    InsertionSortCollider([Bo1_Sphere_Aabb(aabbEnlargeFactor=factor),Bo1_Facet_Aabb()]),
    InteractionLoop(
        [Ig2_Sphere_Sphere_ScGeom(interactionDetectionFactor=factor),Ig2_Facet_Sphere_ScGeom()],
        [Ip2_JCFpmMat_JCFpmMat_JCFpmPhys(cohesiveTresholdIteration=1,label='JCFpm')],
        [Law2_ScGeom_JCFpmPhys_JointedCohesiveFrictionalPM(recordCracks=False)]
    ),
    NewtonIntegrator(damping=damp,gravity=(0,0,-9.81),label='newton'),
]

```

```
O.dt=.8*utils.PWaveTimeStep() #Timestep
```

```
*****Recall functions*****
```

```
O.engines=O.engines + [PyRunner(command='Stab()',iterPeriod = 100,label='vez')]
```

```
O.engines=O.engines + [PyRunner(command='Save()',iterPeriod=50, label='save')]
```

```
*****Functions*****
```

```
MaxN = 3000
```

```
MinN = MaxN *.99
```

```
MinuForce = .7
```

```
def Stab():          #Investigate system stability
```

```
if O.iter > 7000000:      #Execute after 3000 iterations
```

```
if utils.unbalancedForce() < MinuForce:      # stability measures drop below the limit
```

```
    # Define the displacement plane with an infinite area above the uppermost particle with a distance of radius
```

```
magassag = max([b.state.pos[2] + b.shape.radius for b in O.bodies if isinstance(b.shape,Sphere)]) # Define the uppermost particle Z coordinate + R
```

```
global kezdo          #Default global variable considered by all functions
```

```
kezdo = O.iter        #Default value equals to the number of iterations when “h” damped
```

```
global Lap1          #Lap1 global variable considered by all functions
```

```
global Lap2          #Lap2 global variable considered by all functions
```

```
global Lap3          #Lap3 global variable considered by all functions
```

```
global Lap4          #Lap4 global variable considered by all functions
```

```
global Lap5          #Lap5 global variable considered by all functions
```

```
global Lap6          #Lap6 global variable considered by all functions
```

```
Lap1=O.bodies.append(utils.facet([(-length*1.5,-width*1.5,magassag),(-length*1.5,width*1.5,magassag),(length*1.5,width*1.5,magassag)], material = 'wall')) #Part 1 of displacement plane
```

```
Lap2=O.bodies.append(utils.facet([(-length*1.5,-width*1.5,magassag),(length*1.5,-width*1.5,magassag),(length*1.5,width*1.5,magassag)], material = 'wall')) #Part 2 of displacement plane
```

```
Lap3=O.bodies.append(utils.facet([(-length*1.5,-width*1.5,magassag*1.01),(-length*1.5,width*1.5,magassag*1.01),(length*1.5,width*1.5,magassag*1.01)], material='wall'))
```

```
Lap4=O.bodies.append(utils.facet([(-length*1.5,-width*1.5,magassag*1.01),(length*1.5,-width*1.5,magassag*1.01),(length*1.5,width*1.5,magassag*1.01)], material = 'wall'))
```

```
Lap5=O.bodies.append(utils.facet([(-length*1.5,-width*1.5,magassag*1.02),(-length*1.5,width*1.5,magassag*1.02),(length*1.5,width*1.5,magassag*1.02)], material = 'wall'))
```

```
Lap6=O.bodies.append(utils.facet([(-length*1.5,-width*1.5,magassag*1.02),(length*1.5,-width*1.5,magassag*1.02),(length*1.5,width*1.5,magassag*1.02)], material = 'wall'))
```

```
velZ = -.005
```

```
nyomolapok = [Lap1,Lap2]
```

```
O.bodies[Lap1].state.vel[2]=velZ #Displacement down of Part 1 of displacement plane
```

```
O.bodies[Lap2].state.vel[2]=velZ #Displacement down of Part 2 of displacement plane
```

```
O.bodies[Lap3].state.vel[2]=velZ #Displacement down of Part 1 of auxiliary displacement plane 1
```

```
O.bodies[Lap4].state.vel[2]=velZ # Displacement down of Part 2 of auxiliary displacement plane 1
```

```
O.bodies[Lap5].state.vel[2]=velZ # Displacement down of Part 1 of auxiliary displacement plane 2
```

```
O.bodies[Lap6].state.vel[2]=velZ # Displacement down of Part 2 of auxiliary displacement plane 2
```

```
print('m= ' + str(massCalc(-1.)) + ' kg')
```

```
save.command = 'Save2()'      #Iterative command of save, recalls the function 'Save2()'
```

```
vez.command = 'stop()'       # Iterative command of save, recalls the function 'stop()'
```

```
def Save():      #Data saving
```

```
    plot.addData(i=O.iter,uF=utils.unbalancedForce())
```

```
def Save2():
```

```
    global N      #Data saving
```

```
    N = O.forces.f(Lap1)[2] + O.forces.f(Lap2)[2]    #Tangential force acting on the displacement plane
```

```
    #plot.addData(i=O.iter,N=Normalero,T=T)          #Saving iteration numbers and tangential force, N and T
```

```
    plot.addData(i=O.iter,N=N,uF=utils.unbalancedForce(),i2=O.iter) # Saving iteration numbers and tangential force, N and T
```

```
def stop():
```

```
if N > MaxN:
```

```
O.bodies[Lap1].state.vel[2]=0    # Displacement down of Part 1 of displacement plane
```

```
O.bodies[Lap2].state.vel[2]=0
```

```
O.bodies[Lap3].state.vel[2]=0
```

```
O.bodies[Lap4].state.vel[2]=0
```



```
O.bodies[Lap5].state.vel[2]=0
```

```
O.bodies[Lap6].state.vel[2]=0
```

```
sulypMent2('sulypontkord')
```

```
def ment():
```

```
plot.addData(i=O.iter,uF=utils.unbalancedForce())
```

```
if O.iter > 40000 and utils.unbalancedForce() < .05:
```

```
global heightP
```

```
heightP = max([b.state.pos[2] + b.shape.radius for b in O.bodies if isinstance(b.shape,Sphere)]) #height of topmost sphere + R
```

```
print('height = ' + str(heightP))
```

```
#if O.bodies[frac[0]].state.pos[2] > .5:
```

```
global frac
```

```
global packingPlate
```

```
packingPlate = O.bodies.append(geom.facetBox((.0,.0,heightP+.105),(length,width,.1),wallMask=16, material='wall'))
```

```
frac = O.bodies.append(ymport.gmsh('ZSEB.mesh',fixed=True,material='wall',shift=(0,0,-.1+heightP*.7),scale=1,wire=True,color=(0,0,0)))
```

```
vel = .8
```

```
O.engines = O.engines + [TranslationEngine(ids=frac,translationAxis=(0,0,-1),velocity=vel)]
```

```
O.engines = O.engines + [TranslationEngine(ids=packingPlate,translationAxis=(0,0,-1),velocity=vel*1.5)]
```

```
vez.command='ell()'
```

```

def ell():
    plot.addData(i=O.iter,uF=utils.unbalancedForce())
    if O.bodies[packingPlate[0]].state.pos[2] < heightP * 3:
        O.engines = O.engines + [TranslationEngine(ids=packingPlate,translationAxis=(0,0,-1),velocity=0)]
    if O.bodies[frac[0]].state.pos[2] < heightP * 8:
        O.engines = O.engines + [TranslationEngine(ids=frac,translationAxis=(0,0,-1),velocity=.0)]
    coh.setCohesionNow=True
    for b in frac:
        O.bodies.erase(b)
    for b in packingPlate:
        O.bodies.erase(b)
    radiusP = 0.0025
    sp2 = pack.SpherePack()
    #coeff2 = .5 #coefficient for smaller dimensions of the predicate
    sp2.makeCloud((-0.0075,-.045,heightP),(0.0075,.045,1.2*heightP),rMean=radiusP,rRelFuzz=0.)

    n = sp2.toSimulation(material='prop')
    for i in n:

```

```
O.bodies[i].shape.color = (0.,.5,0.)
```

```
#for b in container:
```

```
# O.bodies.erase(b)
```

```
#O.pause()
```

```
vez.dead=True
```

```
def sulypMent(time):
```

```
fileName = 'sulyp' + time + '.txt'
```

```
sulyp = open(fileName,'w')
```

```
sulyp.write('mm\n')
```

```
sulyp.write('ID,x,y,z\n')
```

```
for b in O.bodies:
```

```
if isinstance(b.shape,Sphere):
```

```
    Sx = b.state.pos[0]*1000
```

```
    Sy = b.state.pos[1]*1000
```

```
    Sz = b.state.pos[2]*1000
```

```
    ID = b.id
```

```
    sulyp.write(str(ID)+' '+str(Sx)+' '+str(Sy)+' '+str(Sz)+'\n')
```

```
sulyp.close
```

```

def sulypMent2(fileName): #Saving the centers of gravity # excel – import 3D cloud of points into inventor
fileName2 = fileName + '.txt'
sulyp = open(fileName2,'w')
sulyp.write('mm\n')
sulyp.write('ID,x,y,z\n')
for b in O.bodies:
if isinstance(b.shape,Sphere): #Exclude coordinates if the particle is a sphere
    Sx = b.state.pos[0]*1000
    Sy = b.state.pos[1]*1000
    Sz = b.state.pos[2]*1000
    ID = b.id
    sulyp.write(str(ID)+' '+str(Sx)+' '+str(Sy)+' '+str(Sz)+'\n')
sulyp.close

def felsoSzem():
felszin = []
for b in O.bodies:
if isinstance(b.shape,Sphere):
    print ('#####')

```

```

sulypZ = b.state.pos[2]
print (sulypZ)
contPoint = []
for i in O.bodies[b.id].intrs():
    if isinstance(O.bodies[i.id1].shape,Sphere) and isinstance(O.bodies[i.id2].shape,Sphere):
        contPoint.append(i.geom.contactPoint[2])
print (contPoint)
teszt = 0
for i in contPoint:
    if i > sulypZ:
        teszt += 1
if teszt == 0:
    felszin.append(b.id)
print (felszin)
def massCalc(zPos):
    #mass calculation of spheres above zPos
    m = 0
    for b in O.bodies:
        if isinstance(b.shape,Sphere):
            #cummulate mass of spherical elements above zPos

```

```

if b.state.pos[2] + b.shape.radius > zPos:
    m += b.state.mass
return m
#*****Draw the diagram*****

plot.plots = {'i':'uF',i2: (('N','r-'),None,('uF','b-'))} #Diagram drawing
plot.plot() #Diagram display

#*****RUN*****
#O.run() #RUN the simulation
#utils.waitForBatch()
#OpenGLRenderer.ghosts=False

```